ABSTRACT

Title of dissertation: OPTICAL AND CASIMIR EFFECTS IN TOPOLOGICAL MATERIALS

Justin H. Wilson, Doctor of Philosophy, 2015

Dissertation directed by: Professor Victor M. Galitski
Department of Physics

Two major electromagnetic phenomena, magneto-optical effects and the Casimir effect, have seen much theoretical and experimental use for many years. On the other hand, recently there has been an explosion of theoretical and experimental work on so-called topological materials, and a natural question to ask is how such electromagnetic phenomena change with these novel materials. Specifically, we will consider are topological insulators and Weyl semimetals.

When Dirac electrons on the surface of a topological insulator are gapped or Weyl fermions in the bulk of a Weyl semimetal appear due to time-reversal symmetry breaking, there is a resulting quantum anomalous Hall effect (2D in one case and bulk 3D in the other, respectively). For topological insulators, we investigate the role of localized in-gap states which can leave their own fingerprints on the magneto-optics and can therefore be probed. We have shown that these states resonantly contribute to the Hall conductivity and are magneto-optically active. For Weyl semimetals we investigate the Casimir force and show that with thickness, chemical potential, and magnetic field, a *repulsive and tunable* Casimir force can be obtained.

Additionally, various values of the parameters can give various combinations of traps and antitraps.

We additionally probe the topological transition called a Lifshitz transition in the band structure of a material and show that in a Casimir experiment, one can observe a non-analytic "kink" in the Casimir force across such a transition. The material we propose is a spin-orbit coupled semiconductor with large g-factor that can be magnetically tuned through such a transition. Additionally, we propose an experiment with a two-dimensional metal where weak localization is tuned with an applied field in order to definitively test the effect of diffusive electrons on the Casimir force—an issue that is surprisingly unresolved to this day.

Lastly, we show how the time-continuous coherent state path integral breaks down for both the single-site Bose-Hubbard model and the spin path integral. Specifically, when the Hamiltonian is quadratic in a generator of the algebra used to construct coherent states, the path integral fails to produce correct results following from an operator approach. We note that the problems do not arise in the time-discretized version of the path integral, as expected.

OPTICAL AND CASIMIR EFFECTS IN TOPOLOGICAL MATERIALS

by

Justin H. Wilson

Dissertation submitted to the Faculty of the Graduate School of the
University of Maryland, College Park in partial fulfillment
of the requirements for the degree of
Doctor of Philosophy
2015

Advisory Committee:
Professor Victor M. Galitski, Advisor & Chair
Professor Sankar Das Sarma
Professor Christopher Jarzynski
Professor Jeremy N. Munday
Professor Jay Deep Sau

Dedication

I dedicate this dissertation to my sister, Megan Walker, for her unwavering love and support.

Acknowledgments

There are many people to thank that have helped me on my journey: Friends and family, colleagues and mentors.

First, I thank my advisor Victor Galitski for a great many things. As my advisor he has patiently been there while I have sometimes struggled or been stuck on a research problem. Additionally, he provided many opportunities to do what many starting in science have a hard time grasping: collaborating, getting out there and making yourself known. Naturally, this entire dissertation would not exist without him, and I am very thankful he has been my advisor.

I also need to thank my fellow graduate student Andrew Allocca. When he joined Victor's group, we immediately began collaborating on a project idea that Victor and I had formulated, and we've since seen the fruits of this labor in three publications, all of which are presented in this dissertation. Andrew did the bulk of the technical work for two of these publications, and he deserves credit for that. He has also become a fast friend.

My other collaborators have also been amazing and helpful, not just scientifically, but with advise and oftentimes friendships outside of the work environment: Benjamin Fregoso, Dmitry Efimkin, and Joe Mitchell. Dmitry was the genesis of the idea in Chapter 2 and has been a pleasure to work with. We have a large group and everyone in that group has been amazing and also has my thanks.

Outside of collaboration, I thank Sankar Das Sarma for helping me make the transition from quantum gravity to condensed matter theory, and providing a bit

of the philosophical underpinnings of condensed matter which is presented herein. I have also been helped by conversations with Michael Levin on the project regarding path integrals presented in Chapter 5, and Liang Wu for the initial conversation that led to Chapter 4.

Oh, and I have to thank Jed Pixley. But mostly for not tearing my head off for my procrastinating on our research collaboration by working on my dissertation.

Table of Contents

List of Figures

List of Abbreviations

APS	American Physical Society
AQHE	Anomalous quantum Hall effect
RPA	Random phase approxmation
TE	Transverse electric
TI	Topological insulator
TM	Transverse magnetic
UCF	Universal conductance fluctuations
WL	Weak localization

Chapter 1: Introduction

In the low-energy physics regime commonly studied by condensed matter theory and cold atom physics, electromagnetism is the dominant force at play. Electrons are bound to atoms by the Coulomb attraction, the electrostatic attraction between charges, and in semiconducting solids described by a band structure, a Fermi sea of electrons (usually described with the outermost shell of electrons hopping amongst atoms) has observable properties mainly through its electromagnetic coupling. Additionally, electrons interact with one another, again through electromagnetism, producing interesting phenomena.

Many interesting things are still being studied within the context of non-interacting band theory. Due to material properties, sometimes the band structure of a material has a topological character—usually a topological number such as a Chern number [8]. Two examples of this considered in this dissertation are topological insulators and Weyl semimetals [9] (see Sec. 1.3.1 and Sec. 1.3.2 respectively for more details).

The basic reductionist theory for a material is fully described by many-particles (usually electrons in a solid) interacting with electromagnetism. However, there are

This introduction borrows from the introductions of the papers covered herein: [3–7], copyright APS.

still very interesting and unsolved problems that emerge when one puts a lot of charges together in something as commonplace as a solid. And in these cases, the problem as expressed by the full "wave-function" of all electrons and photons is both intractable and useless.

In this dissertation, the electromagnetic force is dealt with directly. In simple terms, a lot of what is considered here is related to the linear response of a material to an electromagnetic field captured by the conductivity σ defined as $\mathbf{j} = \sigma\mathbf{E}$ where $\mathbf{j}$ is the current density and $\mathbf{E}$ is the applied electric field. While the conductivity is easily calculated with the Kubo formula [10], interactions and disorder can complicate the picture.

This linear response is important not only for transport, but also when one has an incident electromagnetic wave incident on the material. In fact, due to Maxwell's equations, the current and charge induced by an incident wave has an effect on the reflected and transmitted waves. These waves can be measured directly (optically) or indirectly (e.g. with a Casimir experiment) to observe properties of the conductivity that transport misses at higher frequencies.

These phenomena can be used to probe the higher frequency response of the material to electromagnetism which in turn can tell us useful information about the band structure or other material properties. This is the backdrop under which we begin. First, in Chapter 2 we investigate the optics with a thin film 3D topological insulator when we include the effects of states localized to charged impurities. In Chapter 3 we shift gears to the Casimir effect and see first how the Casimir effect can investigate phenomenon like topological Lifshitz transitions in the band structure;

we also investigate how weak localization could be used to discern the effects of diffusion on the Casimir effect. In Chapter 4 we look at the Casimir response between two identical Weyl semimetals to find that they can be repulsive. Finally, we move to the more theoretical in Chapter 5 to discuss a breakdown of the path integral and how it is unrelated to previously identified problems. Before we move into the technical details, we provide an introduction and overview of the material presented here.

1.1 Probing a material with magneto-optics

As one can observe from just looking around, different materials have different optical properties. Mirrors are good reflectors of visible light, pure water is a good at transmitting visible light, and more obscure objects absorb some visible light and diffusively reflect others. But we can even see that the way light interacts is already telling us more than just if it reflects: In water the refractive index is greater than one, causing light rays to "bend".

Light has another property that can change upon interaction with a material: polarization. When the polarization changes in a time-reversal symmetry broken way (due to internal magnetization or an applied magnetic field), these phenomena are known as magneto-optical phenomena.

The first observation of this kind of phenomenon was discovered by Faraday in 1845 [11]. In the first experiment, Faraday sent light through glass with traces of lead in the direction of an applied magnetic field. The angle through which the

polarization rotates through, as verified in a number of materials, takes the form

$$\vartheta_{\mathrm{F}} = \mathcal{V}\ell B, \tag{1.1}$$

where ℓ is the length traveled by the light, B is the magnetic field, and $\mathcal{V}$ is the Verdet constant of the material [12]. We already see that this is probing material properties: The Verdet constant is a property of the material, subject to how electrons in the material are behaving.

The Faraday effect has found use in many areas of physics from astronomy in the characterization of interstellar media [13] and planetary science [14] to semiconductor physics (such as [15] in the case of GaAs). In as early as 1898 [16], the resonant behavior that occurs when the frequency of light incident on the object (in this case, a metallic vapor) is commensurate with transitions in the object was seen. It was not until the advent of atomic physics and the quantum mechanical description of the interaction of light and matter that these observations were put on a firm theoretical base. Now, these experimental observations are powerful tools to probe material properties.

Similar to the Faraday effect is the Kerr magneto-optical effect (referred here as the *Kerr effect*, not to be confused with the nonlinear electro-optical effect of the same name) discovered by Kerr in 1877 [17]. While the Faraday effect refers to the transmitted light's polarization, the Kerr effect concerns rotation of the reflected light.

For a material in the modern context, the optical conductivity $\sigma(\omega)$ is calculated with Kubo formula which crucially depends on the band structure (or generally,

the ground state and excitations of the material's Hamiltonian). Then when an incident light hits a material it causes a current $\mathbf{j}(\omega) = \sigma(\omega)\mathbf{E}(\omega)$. This current in turn creates its own field, and causes a reflected and transmitted wave. The resonant behavior of this reflection and transmission is all in the optical conductivity $\sigma(\omega)$ since if there are resonant transitions at ω, we will observe a large current response as a result (see Chapter 2 for more details on a particular case).

These effects have been around for over a hundred years, but we still see active use to identify resonances and time-reversal symmetry breaking nature of materials such as for topological insulators (e.g. [18] and [19]) and chiral superconductors (e.g. [20]). As we describe in detail in Chapter 2, we will show how a localized in-gap state will give a resonant Faraday and Kerr effect.

1.2 The Casimir effect

Another, more subtle, electromagnetic phenomenon resulting from quantization of the electromagnetic field was found in 1948, when Casimir predicted attraction between two neutral, perfectly conducting materials [2], The origin of this phenomenon is the differences in vacuum energies from infinite free space. Schematically, when one quantizes a field operator such as the electromagnetic field given by the vector field A_μ, every classically permitted solution can be occupied by an integer number of "photons". Mathematically, this usually means for bosonic fields that quantum harmonic oscillators describe the excitations of the field (photons for

QED). The Hamiltonian for such a system is just

$$H = \sum_{\mathbf{k},\sigma} \hbar\omega(\mathbf{k}) \left(a^\dagger_{\mathbf{k}\sigma} a_{\mathbf{k}\sigma} + \tfrac{1}{2} \right). \tag{1.2}$$

where $[a_{\mathbf{k}\sigma}, a^\dagger_{\mathbf{k}'\sigma'}] = \delta_{\mathbf{k}\mathbf{k}'}\delta_{\sigma\sigma'}$, $\omega(\mathbf{k})$ is the dispersion, σ labels the internal degrees of freedom (e.g. polarization), and $\mathbf{k}$ labels the eigenvectors (e.g. $\mathbf{k}$ is the wave vector in free space).

Usually the constant term in the Hamiltonian that remains when $\langle a^\dagger_{\mathbf{k}\sigma} a_{\mathbf{k}\sigma} \rangle = 0$ (zero photons) is thrown out as a "arbitrary constant" energy. This discarded term is known as the vacuum energy

$$E_0 = \frac{\hbar}{2} \sum_{\mathbf{k}\sigma} \omega(\mathbf{k}) \tag{1.3}$$

It is convenient to throw it out because such a term is formally divergent, but in some cases, it can change in well-defined finite ways (when the eigenenergies given by $\omega(\mathbf{k})$ change). This is the origin of the Casimir energy: defined as the energy difference between the vacuum energy of one configuration and what is defined as "free-space" (in the two-plate geometry this corresponds to letting the plate separation $a \to \infty$).

$$E_c(a) = E_0(a) - E_0(a \to \infty). \tag{1.4}$$

The Casimir force is then defined by the derivative of this object $F_c = -\partial E_c / \partial a$.

The divergent term can be understood quite simply two ways. One way involves vacuum fluctuations in free space that do not involve the plates and the self-energies of each plate individually; both quantities do not depend on distance. The next, more mathematical way, is to understand that E_0 is the first moment of the density of states $E_0 = \frac{1}{2} \int dE\, E\, \rho(E)$. This diverges for unbounded spectra,

but as Weyl showed [21], the asymptotics (for the Laplacian operating on a scalar potential, which with some caveats can be extended to the Maxwell operator) go as $\rho(E) \propto V\sqrt{E}$ where V is the volume of the system (the next order term is a constant surface term and has also been derived [22], accounting for surface self-energies). Since we keep the volume of the system constant (and the surfaces do not deform), these divergent terms are the same in every configuration and can safely be discarded. The remaining terms of $\rho(E)$ after these are discarded give a convergent integral for the first moment, otherwise known as the Casimir energy.

Bringing this back to electromagnetic fields, we can generally get a finite Casimir Free energy for two distinct objects A and B by considering

$$E_c = E_0^{\mathrm{AB}} - E_0^{\mathrm{A}} - E_0^{\mathrm{B}} + E_0^{\text{Free space}}, \tag{1.5}$$

(we have over-counted free space by subtracting off each object individually). This amounts to summing up the vacuum diagrams that only connect objects A and B,

$\mathcal{E}_c =$ 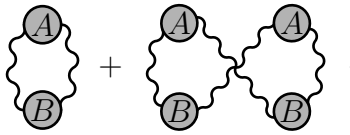 (1.6)

where  $\equiv \tilde{\Pi}_X$ accounts for all interactions taking place on plate X. Or mathematically,

$$\mathcal{E}_c = \frac{\hbar}{\beta} \sum_{i\omega_n}{}' \operatorname{Tr} \log[\mathbb{I} - \tilde{\Pi}_A D_{AB} \tilde{\Pi}_B D_{BA}]. \tag{1.7}$$

where the trace is a full operator trace (over position and polarization), ω_n are the Matsubara frequencies with the $\sum'$ representing a sum over positive frequencies with the zero mode taken at half-weight, and D_{XY} is photon propagator connecting

X and Y. This quantity has been derived many times [23] with a particular instance for compact dielectric objects appearing in [24] derived via path integration and for two-dimensional sheets in the Appendix of [4]. One can see that reflections off of the two objects are important. In fact, if we specialize to two parallel plates (labeled now 1 and 2), we can obtain the Casimir energy density [25, 26] formula known as the Lifshitz formula with just reflection matrices (R_1 and R_2 respectively)

$$E_c(a) = \frac{\hbar}{\beta} \sum_{i\omega_n}{}' \int \frac{d^2k}{(2\pi)^2} \operatorname{tr} \log[\mathbb{I} - R_1 R_2 e^{-2q_z a}], \tag{1.8}$$

where the trace is now just a matrix trace, and $q_z \equiv \sqrt{\omega_n^2 + q^2}$. This discussion highlights the strange place Casimir energy and force occupies: It is calculated with purely classical objects (either the classical eigenenergies or reflection matrices discussed here), but all of the photons experiencing these are *virtual* and hence making it a purely quantum effect.

It will be useful to relate Eq. (1.8) to the linear response of the material. In the two-dimensional limit [4], we have that the reflection matrix description is equivalent to the random phase approximation (RPA) applied to the linear response Π_X defined by $j^\mu = \Pi_{X,\mu\nu} A^\nu$ for vector potential field A^ν,

$$\tilde{\Pi}_X = (\mathbb{I} - \Pi_X D)^{-1} \Pi_X, \tag{1.9}$$

or diagrammatically the RPA is given by

(1.10)

is the dressed current-current correlation function for plate X while $\Pi_X \equiv$

$\tilde{\Pi}_X$ is the usual current-current correlator derived in linear response theory – a

clearly material-dependent quantity related to conductivity at real frequencies by $\sigma(\omega) = \frac{\Pi(\omega)}{i\omega}$.

It is a general theorem that mirror symmetric objects without time-reversal symmetry breaking can only attract one another with the Casimir effect [27]. Nonetheless, Casimir repulsion between two materials in vacuum is a long sought after phenomenon [26, 28]. There are principally four categories in which repulsion can be achieved: (i) Modifying the dielectric of the intervening medium [26, 29, 30]; (ii) Pairing a dielectric object and a permeable object [28] (such as with metamaterials [31–33]); (iii) Using different geometries [34–36]; and (iv) Breaking time-reversal symmetry [37–39]. As one can see from Eq. (1.8), the integral generally yields an attractive force (eigenvalues of the square of the reflection matrix R^2 are usually positive); however, if we break time reversal symmetry, obtaining antisymmetric off-diagonal terms in the reflection matrix $R_{xy} = -R_{yx}$ there is the possibility of Casimir repulsion [40]. One candidate is a two-dimensional Hall material [38], and similarly, another is a topological insulator where the surface states have been gapped by a magnetic field [37, 39]. A Hall conductance does not guarantee repulsion; longitudinal conductance can overwhelm any repulsion from the Hall effect (though the magnetic field can lead to interesting transitions [4]), and a Hall effect that is too strong can suppress Kerr rotation and hence lead to attraction. The latter case is an interesting phenomenon where "more" of a repulsive material can lead to attraction.

In the realm of Casimir experiments, after nearly 50 years of theory [41], experimental evidence was presented by Lamoreaux [42]. Following this discovery there was a flurry of theory [23, 43] and experiment [30, 44–48] which led to an

astounding amount of theoretical and experimental machinery. With this machinery, others have observed that the Casimir force can have a nontrivial dependence on material parameters [49–55], some of which may be tunable. Being able to tune the Casimir force by modifying the frequency-dependent conductivity [56–58] could have important applications for precision gravity experiments [59–63] and applications to nanotechnology [64].

From the other direction, any change of the Casimir force would be an indication of a change in the material's properties. Just as a repulsive effect would be a signature of some time-reversal symmetry breaking , other changes in the Casimir force can be attributed to other material properties. For instance, Bimonte and coauthors showed that one can in principle measure the change in Casimir energy between a normal and a superconducting state [51, 52]. Additionally, it has been demonstrated that both the Casimir effect and the thermal Casimir effect [53] are capable of probing phase transitions [54, 55].

Unfortunately, some details of the theory describing experiments are still unresolved. When applying the Casimir effect to a real experiment, it is theoretically calculated by modeling metallic plates with one of two models: the Drude or plasma model. These simplified models describe the linear response of electrons in the plates to an electromagnetic field at low frequencies. While the Drude model describes diffusive electrons subject to a random disorder potential, the plasma model describes ballistic electrons unhindered by disorder. These two models typically provide similar predictions of the Casimir force as a function of plate separation, with the plasma model predicting a slightly stronger attraction than the Drude model in

non-magnetic metals.

Quantitative results from many experiments [65–68] seem to favor the plasma model over a naive Drude model—in some ways, arguably, the more physical of the two. Many experiments attempt to account for the effect of electrostatic patch potentials in the plates, expecting the effect to be relevant for agreement with one model or the other. Several of these [67, 68] find that the correction due to patches would make agreement with Drude worse while others [53, 69] see agreement with the Drude model once the effect of patches is minimized. There is recent theoretical and experimental work specifically to account for the contribution of patch potentials [70, 71]. While the initial theoretical results seemed to weaken the case for the plasma model, the comparison of calculation and experiment shows the contribution to the force from patch potentials to be approximately an order of magnitude smaller than the difference between the Drude and plasma models. However, the authors caution that the analysis is preliminary and acknowledge future work may be needed. In the same vein as the work done on patch potentials, there has also been investigation into the effect of charge disorder[72], finding that quenched and annealed disorder contribute to the Casimir force in markedly different ways, with quenched disorder completely overwhelming the Casimir force at large distances. Additionally, another method that may be able to distinguish between the Drude and plasma models based on the thermal Casimir force has also been proposed [73, 74], and recent preliminary experimental observations based on this proposal seem to, again, favor a plasma model [75].

In this dissertation we will show a material phenomenon that the Casimir effect

actually can capture with (Lifshitz transition, see Sec. 1.8), propose an experiment to see what role diffusion has (or does not have) in the Casimir effect, and demonstrate a material that could see repulsion (Weyl semimetals, see Sec. 1.3.2).

1.3 Topological materials

Ever since Thouless, Kohmoto, Nightingale, and Den Nijs demonstrated topology in the quantum Hall effect [76], topology has found its way into many parts of condensed matter theory. Topological order has been identified by authors, connecting various gapped ground states [77] distinguishing long-range entangled (LRE) states and short-range entangled (SRE) states. Once a symmetry is added into this scheme, the SRE states can be further distinguished in to symmetry protected topological (SPT) phases and non-topological phases. These SPT phases include topological insulators (Sec. 1.3.1). For gapless Fermionic states, topology can still be assigned in terms of the Fermi points (or the undergoing of a Lifshitz transition as described later) [78]. These features will be important in Weyl semimetals [79].

1.3.1 Topological Insulators

Topological insulators (TIs) represent a new class of solids whose band structure can be characterized by a $\mathbb{Z}_2$ topological invariant [80–83]. As with normal "non-topological" insulators, their bulk has a filled valence band with an empty conduction band separated by a gap. But unlike usual insulators, TIs have very unconventional, symmetry-protected surface states. Interest in TIs has grown con-

siderably since the discovery of two-dimensional (HgTe [84, 85]) and subsequently three-dimensional TIs (Bi_2Se_3, Bi_2Te_3 and other Bismuth based materials [86–89]). The surface states of three-dimensional TIs are described by a Dirac equation for massless particles, but unlike two-dimensional systems like graphene, there is only one Dirac "cone" (in general, an odd number)—something that can only be realized at the surface of a bulk three-dimensional system [90, 91]. Thus, the surface of a TI is a veritable experimental and theoretical playground for many interesting phenomena including but not limited to both topological superconductivity, which gives rise to exotic Majorana fermions [92] (these could potentially be used as building blocks for quantum computation [93]) and the anomalous half-integer quantum Hall effect (AQHE) [94] (See also Refs. [8, 95] for a review).

The AQHE occurs when time-reversal symmetry is broken, opening up a gap in the Dirac surface states. Without an external magnetic field, this effect can be realized by an exchange field that couples to the spins of the electrons on the surface. The exchange field can be induced either by the proximity effect with an insulating ferromagnet [96] or by the ordering of magnetic impurities introduced to the bulk or surface of a TI [94, 97, 98]. Recently, both methods of inducing an exchange field have been realized experimentally [99–102] and the AQHE has been experimentally confirmed by transport measurements [103]. The AQHE is the origin of the "image monopole effect" for an electron in the vicinity of a TI surface [104] as well as reflectionless chiral electronic states localized on domain walls that separate regions with the opposite exchange field [105].

Another way to probe the AQHE is with the magneto-optical Faraday and

Kerr effects discussed in Sec. 1.1 where the polarization of the transmitted and reflected electromagnetic waves rotates relative to the wave incident on the TI's surface. At low frequencies—when dispersion effects can be neglected—the optics of the TI nanostructures can be described macroscopically with an additional axionic θ-term in the action ΔS_{AE}, which is insensitive to microscopical details [96, 106] and is given by

$$\Delta S_{\mathrm{AE}} = \theta \frac{e^2}{2\pi h} \int dt\, d^3r\, \mathbf{E} \cdot \mathbf{B}. \tag{1.11}$$

Here $\theta = 0$ for ordinary insulators and $\theta = \pi$ for topological ones. Moreover for thin film TIs, the Faraday angle $\tan \vartheta_{\mathrm{F}} = \alpha_0$ and the Kerr angle $\tan \vartheta_{\mathrm{K}} = 1/\alpha_0$ are predicted to be universal [107–109] and depend *only* on the fine-structure constant $\alpha_0 = e^2/\hbar c \approx 1/137$.

The theoretical investigation of the Faraday and Kerr effect beyond the low frequency regime is important not only because real optical experiments occur at finite frequency but also because single-particle and collective excitations on the surface of TI start to leave their own fingerprint on optical quantities. In particular, chiral excitons, which are collective in-gap excitations in the gapped Dirac electron liquid, reveal their chiral nature [110] via prominent resonances seen in the frequency dependence of the Faraday and Kerr angles [1]. In Chapter 2 we consider other in-gap excitations, localized electronic states, which are present due to inevitable impurities occurring in the TI bulk or on its surface. In usual semiconductors, in-gap states dominate absorption and magneto-optical effects do not appear without a magnetic field; the exceptions are magnetic semiconductors where there are similar

effects [111].

1.3.2 Weyl semimetals

The topological nature of the Weyl semimetals lie at the Weyl nodes where for low energies and chemical potential at the Weyl node [9, 78]

$$H_W = \pm \hbar v_{\mathrm{F}} \mathbf{k} \cdot \boldsymbol{\sigma}, \tag{1.12}$$

where $\mathbf{k}$ and $\boldsymbol{\sigma}$ are the 3D wave vector and vector of Pauli matrices respectively. Each node has a *chirality* (+ or - in the above Hamiltonian) and has a chiral anomaly [112]. Furthermore, they come in pairs requiring either time-reversal or inversion symmetry to be broken [79] and they can annihilate each other when brought to the same place in $\mathbf{k}$ space. One theoretically easy way to study these semimetals is at the phase transition between a topological insulator and a normal insulator. The topology here lies around the nodes themselves [9]. If you consider the Bloch states $|u(\mathbf{k})\rangle$, and compute the effective vector potential $\mathbf{A}(\mathbf{k}) = i \langle u(\mathbf{k}) | \partial_{\mathbf{k}} | u(\mathbf{k}) \rangle$ and Berry curvature $\mathbf{F}(\mathbf{k}) = \partial_{\mathbf{k}} \times \mathbf{A}(\mathbf{k})$, then the chirality χ (a quantized number $\chi = \pm 1$) can be calculated

$$\chi = \frac{1}{2\pi} \oint \mathbf{F}(\mathbf{k}) \cdot d\mathbf{n}(\mathbf{k}), \tag{1.13}$$

where the integral is over a Fermi surface that encloses the Weyl node. This is directly analogous to calculating the flux through a surface enclosing a magnetic monopole.

Weyl semimetals have a weak longitudinal conductance and a bulk Hall effect [9, 113]. Clean Weyl semimetals at zero temperature have a zero DC longitudinal

conductivity and optical conductivity $\mathrm{Re}[\sigma_{xx}] \propto \omega$ [114]. Additionally, they exhibit a bulk Hall effect exemplified in the DC limit by an axionic field theory [115] where in addition to the Maxwell action, we have, much akin to Eq. (1.11),

$$S_A = \frac{e^2}{32\pi^2\hbar c} \int d^3r\, dt\, \theta(\mathbf{r}, t) \epsilon^{\mu\nu\alpha\beta} F_{\mu\nu} F_{\alpha\beta}, \tag{1.14}$$

where $\theta(\mathbf{r}, t) = 2\mathbf{b} \cdot \mathbf{r} - 2b_0 t$, and $2\mathbf{b}$ is the distance between Weyl nodes in $\mathbf{k}$-space while $2b_0$ is their energy offset (resulting from the Chiral anomaly); e is the charge of an electron; $\hbar$ is Planck's constant; c is the speed of light; $F_{\mu\nu}$ is the electromagnetic field strength tensor; and $\epsilon^{\mu\nu\alpha\beta}$ is the fully antisymmetric 4-tensor. Inversion symmetry breaking Weyl semimetals, on the other hand, do not exhibit a DC Hall effect [116] and therefore will not see the effects described in this letter. The electrodynamics of this were investigated in [117] where the authors even comment on the possibility for a repulsive Casimir effect.

The marginal nature of Weyl semimetals makes them prime candidates for tuning the Casimir force between attractive and repulsive regimes. In constructed Weyl semimetals made of heterostructures of normal and topological insulators [118] an external magnetic field can control the Hall effect [119] and hence the repulsive effects. Additionally, some of the first materials that have been predicted were pyrochlore iridates [120–122]; these could also see a repulsion tunable with carrier doping or an additional magnetic field.

In a real material and experiment at finite temperature, disorder and interactions should be taken into account and in Weyl semimetals they lead to a finite DC conductivity [113, 114, 118].

1.4 Material properties

We investigate in Chapter 3 how some material properties could change the Casimir effect. Here, we provide a brief overview of these phenomena (Lifshitz transitions and weak localization).

1.4.1 Lifshitz Transitions

A Lifshitz transition, or second-and-half order transition, occurs when a material's Fermi surface undergoes a topological change [78] – such as the emergence or collapse of an electron or hole pocket [123, 124]. This is a sharp transition only at zero temperature, and any finite temperature smooths out what is seen, but as long as T/μ is small (in a good metal, for instance), relatively sharp effects should still be seen. One typical way of seeing this effect is through thermopower [124] where maxima correspond to where the Lifshitz transition occurs.

Mathematically, the effect manifests itself as nonanalytic kinks in the conductivity and the carrier density as the system is tuned through a transition, so anything that uses the conductivity should also see a kink, and anything that depends on the derivative of the conductivity (or density of carriers).

Various models are suspected to undergo some type of Lifshitz transition [125–127] including the cuprates [128], and experimental evidence of a Lifshitz transition has been recently observed in iron arsenic superconductors [129].

1.4.2 Weak localization

Weak localization (WL) is a well known and greatly studied effect [130–134], most easily observed in low-dimensional disordered systems at low temperatures where quantum interference logarithmically decreases the conductivity of a sample with decreasing temperature. This is most easily understood via the simple Einstein relation, $\sigma = 2e^2\nu D$, where ν is the electronic density of states per spin in the material and D is the diffusion constant. Weak localization provides a quantum correction to the diffusion constant, $D \to D + \delta D$, that is strongly dependent on both temperature and an applied magnetic field at very low temperatures.

In a semiclassical picture, every electron's path has some amplitude A_p associated with it, and the propagation probability for an electron is represented by a sum over these trajectories $\sum_{p,q} A_p^* A_q = \sum_p |A_p|^2 + \sum_{p \neq q} A_p^* A_q$. When considering self-intersecting paths, the interference term $\sum_{p \neq q} A_p^* A_q$ has a constructively interfering term as long as electrons maintain their phase coherence. Thus, one direction of propagation around a loop and its time-reversed counterpart interfere constructively, leading to a higher probability of finding the electron in the loop, and a lower total probability for the electron to be transmitted through the sample, resulting in a decrease in conductivity.

This effect occurs at temperatures low enough that electrons will not lose phase information in the time taken to propagate around a loop. As the temperature decreases, larger loops can be traversed before phase information is lost, and the suppression of conductivity becomes more pronounced. The effect can be re-

moved by either increasing temperature, so that electron dephasing will occur due to interactions, or by applying a magnetic field, causing an additional phase for each loop path proportional to the area it encloses. Even for weak fields, this phase is enough to ensure the paths will not interfere perfectly constructively anymore, and the WL effect will be suppressed. In the semiclassical picture illustrated above, the magnetic field effect can be introduced with a phase $A_p \to A_p e^{i\phi_p}$ due to flux enclosed by a closed path. Since paths vary in flux they enclose, the interference term will be suppressed – suppressing the effect of WL on conductivity.

The response function of a non-interacting disordered electron gas can be represented diagrammatically as in Fig. 1.1. The simplest approximation considers only the diagrams shown in the first line of the figure—those without impurity lines and all diagrams with impurity interaction ladders. In the long wavelength (i.e. local) limit, $\mathbf{q} \to 0$, these terms combine to give the response function $\Pi^{\text{Drude}} = -\frac{ne^2}{m}\frac{\omega_n}{\omega_n+1/\tau}$, from which the well known Drude result for DC conductivity can be found, $\sigma^{\text{Drude}} = -\lim_{\omega_n\to 0}\Pi^{\text{Drude}}/\omega_n = \frac{ne^2\tau}{m}$. This approximation is valid for the one thick disordered plate we consider.

The leading correction to the Drude result comes from diagrams with maximally crossed impurity lines, shown on the second line of Fig. 1.1, which cannot be ignored in an accurate treatment of the two dimensional plate at low temperatures. These diagrams can be represented as a single diagram containing a cooperon. This approximation to the response function can be written as

$$\Pi = \Pi^{\text{Drude}} + \delta\Pi, \tag{1.15}$$

where $\delta\Pi$ gives the WL correction. An explicit calculation of $\delta\Pi$ in two dimensions, at low but finite temperature T, and with an external magnetic field H, gives the Hikami-Larkin-Nagaoka formula [130, 131],

$$\delta\Pi(i\omega_n; T, H) = -\frac{e^2|\omega_n|}{2\pi^2\hbar}\left[\psi\left(\frac{1}{2}+\frac{\hbar}{4eHD\tau_\phi(T)}\right)-\ln\left(\frac{\hbar}{4eHD\tau}\right)\right], \tag{1.16}$$

where ψ is the digamma function, $D = \frac{v_F^2\tau}{2}$ is the diffusion constant, and τ_ϕ is the electron dephasing time. This expression diverges logarithmically as $T \to 0$ with a sign opposite that of the Drude result, leading to a suppression of conductivity. It also has a very sensitive dependence on an applied magnetic field, becoming very small at moderate values of H ($\sim 100\,\text{gauss}$) even at very low temperatures when the effect would be large in the absence of such a field.

In two dimensions the primary dephasing mechanism at very low temperatures is Nyquist electron-electron scattering, and the dephasing time is given by [135]

$$\frac{1}{\tau_\phi} = \frac{k_B T}{2\pi D\nu\hbar^2}\ln\left(\pi D\nu\hbar\right), \tag{1.17}$$

where $\nu = m/2\pi\hbar^2$ is the density of states per spin at the Fermi level for a two dimensional system.

1.5 Coherent State Path Integrals

Finally, we end our introduction and review with a brief account of the theoretical object: Path integrals. This subject bares no direct relation with the previous topics of magneto-optics and Casimir effect.

Path integrals are widely known for being an alternate formulation of quantum mechanics, and appear in many textbooks as a useful calculational tool for

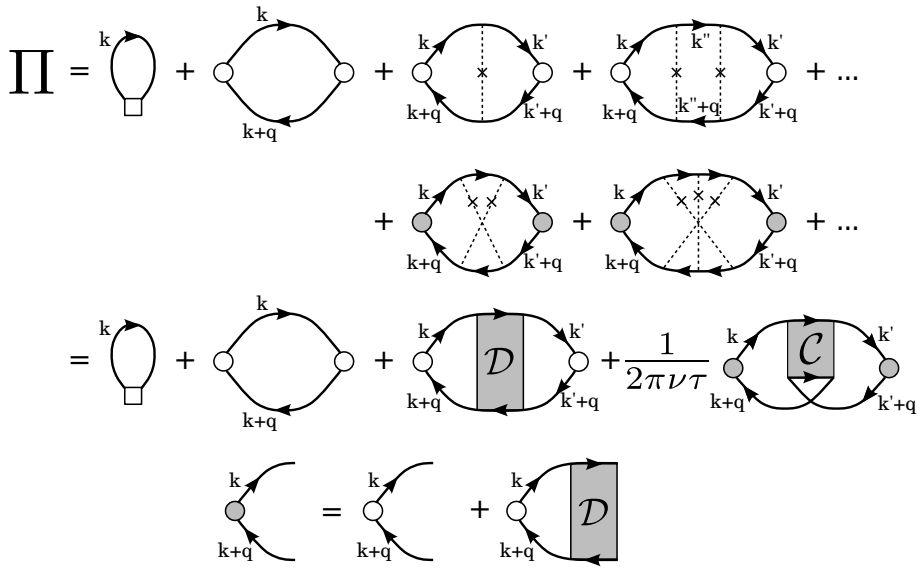

Figure 1.1: The diagrammatic expansion of Π up to the leading correction to the Drude result. Solid lines represent disorder averaged electron Green's functions, dashed lines represent interactions with the disorder potential, the shaded regions represent diffusons (labeled with $\mathcal{D}$) or cooperons (labeled with $\mathcal{C}$) and the circles represent current vertices. The first three diagrams of the third line together give the Drude result, while the last term gives the leading correction. The last line defines the renormalized vertex.

various quantum and statistical mechanical problems (e.g., perturbative expansions, non-perturbative techniques including the instanton method, and effective theories [136–138]). From their inception, there has been the problem of writing down a path integral for any system that can be described by a Hilbert space equipped with a Hamiltonian. One way to approach this problem is with what is known now as the generalized coherent state path integral [139, 140] which generalizes the coherent state path integral for a harmonic oscillator. The key observation with path integration [137] is that, given a Hamiltonian H, the propagator e^{-itH} at some time t can be broken up into N slices $(e^{-itH/N})^N$ and in between each multiplicative term one inserts an (over-)complete set of states parametrized by a continuous parameter. If we take $N \to \infty$ we get the time-continuous formulation. This formulation of path integrals, applied to coherent states, has become widely and routinely used in many areas of physics (see the many papers collected in [141]), yet despite the many successes of path integrals, they have been on very shaky mathematical grounds (for a small "slice" of this history, see [142]).

Glauber coherent states [143] are usually understood as the most classical states associated with the harmonic oscillator. They obey the classical equations of motion for a harmonic oscillator and are minimal uncertainty states. Perelomov and Gilmore [144, 145] extended the definition of coherent states to Lie algebras other than the Heisenberg algebra (i.e., the harmonic oscillator algebra). Since then, these "generalized" coherent states have been used in a number of applications (see [146, 147]). In particular, the coherent states form an overcomplete basis (with a continuous label) which is a necessary ingredient for the construction of a path

integral. For the harmonic oscillator, coherent states are represented by a complex number, but for coherent states constructed with $\mathfrak{su}(2)$ (spin), they are points on the Bloch sphere, S^2.

For the case of the harmonic oscillator, it is commonly known that one can easily go between the normal-ordered Hamiltonian (all annihilation operators commuted to the right) and the coherent state path integral [136]; this is due to the fact that coherent states are eigenvectors of the annihilation operator. For the general coherent state path integral, the "classical" Hamiltonian in the path integral is just the expectation value of the quantum Hamiltonian with a coherent state. This prescription results in some notable exactly solvable cases, but all such cases involve *non-interacting* terms which are essentially linear in the algebra generators used to construct the coherent-states. When the Hamiltonian involves terms that are non-linear in generators (interactions), this prescription fails, as we demonstrate in Chapter 5.

In previous literature, the spin coherent state path integral has sometimes produced (quantitatively) incorrect results [148–152] unless the time-discretized version is employed [151, 153]. These problems with the time-continuous path integral were mostly solved by authors including Stone *et al.* [154] by identifying an anomaly in the fluctuation determinant which added an extra phase to the semi-classical propagator. Kochetov had also found this phase earlier than Stone in a general context [155]. Furthermore, Pletyukhov [156] related the extra phase in the spin path integral back to Weyl ordering the Hamiltonian in the case of the harmonic oscillator (in the simplest case, Weyl ordering corresponds to symmetrically ordering annihi-

lation and creation operators). Additionally, Weyl ordering has been considered in the Bose-Hubbard case in [157]. Unfortunately, this solution does not explain the present breakdown under consideration in Chapter 5 as we will demonstrate.

Chapter 2: Resonant Faraday and Kerr effects due to in-gap states on the surface of a topological insulator

2.1 Overview

Beginning our study into electromagnetic effects of topological materials, we look at the optical effects of topological insulators. This is a well-studied effect beginning with calculation of the so-call "giant Kerr effect" [108]. A non-zero Kerr effect requires time-reversal symmetry breaking: such as an applied magnetic field or ordered magnetic impurities in such a material as described in the Sec. 1.3.1. Such impurities can have excess charge, contributing to localized states on the surface of the topological insulator. These states are magneto-optically active, as we show in this chapter. This chapter is largely taken with slight modification from the author's article [3], copyright APS.

We have shown that localized in-gap states on the magnetically gapped surface of TI are magneto-optically active and lead to peculiar resonant features in frequency dependence of the Faraday and Kerr angles. In this case, the time reversal symmetry is broken *internally* by the exchange field – leading to a nonzero Hall conductivity. The shapes of the resonant features differ considerably from the case

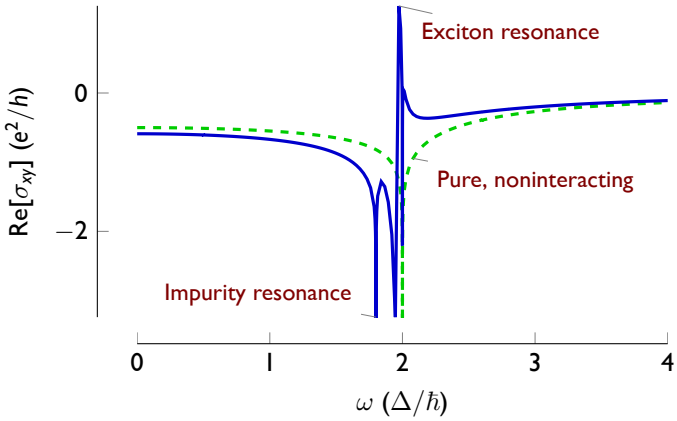

Figure 2.1: Here we plot the optical Hall conductivity in units of half the gap (2Δ is the magnetically induced gap) taking into account both the effect of localized impurity states (the subject of this paper) and chiral excitons – which can be clearly distinguished – and compare it to the pure, noninteracting optical conductivities (dashed line). The chemical potential is at $\mu = -\Delta$ and there is a density $N/S = 0.035 a_0^{-2}$ (see Eq. (2.8)) of Coulomb impurity states with dimensionless coupling to electrons of $\alpha = 0.3$. The exciton contribution is calculated with dimensionless Coulomb coupling between electron and holes of $\alpha_c = 0.18$ and is calculated in Ref. [1]. (See Section 2.2 for discussion of α and $\alpha_c = e^2/\epsilon\hbar v_F$.)

of chiral excitons, so they can be easily distinguished, as can be seen in Fig. 2.1 by the total Hall conductivity taking into account both effects. The magneto-optical effects are controlled by the appearance of a nonzero Hall conductivity and similarly, they inherit frequency dependence from the optical Hall conductivity – in this manner, Fig 2.1 represents the crucial finding of this chapter. These localized in-gap states also lead to prominent resonances in frequency dependence of the ellipticities of transmitted and reflected waves; thus, they can be effectively probed in ellipsometry measurements.

2.2 Localized in-gap states

The single-particle Hamiltonian for Dirac electrons interacting with charged impurities scattered over the surface of a TI is given by

$$H_0 = v_{\mathrm{F}}[\mathbf{p} \times \boldsymbol{\sigma}]_z + \Delta\sigma_z - \sum_i \frac{Ze^2}{\bar{\epsilon}|\mathbf{r} - \mathbf{r}_i|}. \tag{2.1}$$

Here $\mathbf{p}$ is the momentum operator; $\boldsymbol{\sigma}$ is the vector of Pauli matrices with components σ_i; v_{F} is Fermi velocity of Dirac electrons; $\mathbf{r}_i$ is position of of ith impurity and Ze is their charge; $\bar{\epsilon}$ is the effective dielectric permitivity on the surface of the TI[1]; And Δ

[1] In the thin film geometry, the screened potential between two charges on the top of the film has the following form

$$\phi_{\mathrm{exact}}(r) = \frac{2}{\epsilon+1}\frac{Ze}{r} + \frac{4\epsilon}{\epsilon^2-1}\sum_{n=1}^{\infty}\left(\frac{\epsilon-1}{\epsilon+1}\right)^{2n}\frac{Ze}{\sqrt{r^2+(2dn)^2}}. \tag{2.2}$$

In the text, we introduce the effective dielectric constant $\bar{\epsilon}$ so that the resulting Coulomb potential matches the exact potential in the vicinity of the effective radius a_0 of the lowest energy state. The bulk dielectric constant [158] for Bi_2Se_3 is $\epsilon \sim 100$.

parametrizes the out-of-plane component of exchange field which gaps the surface spectrum. The in-plane component can be gauged away and is unimportant for the phenomena with which this paper is concerned.

In the absence of impurities, the surface spectrum is $\epsilon_{\mathbf{p}} = \pm\sqrt{(v_{\mathrm{F}}p)^2 + \Delta^2}$ (+ for the conduction band; − for the valence band, separated by a gap $2|\Delta|$). The wave functions of Dirac states can be presented as $|\mathbf{p}\pm\rangle = e^{i\mathbf{p}\cdot r/\hbar}\,|\varphi_{\mathbf{p}\pm}\rangle$, where the spinor part is given by

$$|\varphi_{\mathbf{p}\pm}\rangle = \frac{1}{\sqrt{2\epsilon_{\mathbf{p}}(\epsilon_{\mathbf{p}} \pm \Delta)}} \begin{pmatrix} \Delta \pm \epsilon_{\mathbf{p}} \\ iv_{\mathrm{F}}pe^{i\theta_{\mathbf{p}}} \end{pmatrix}, \tag{2.3}$$

where $\theta_{\mathbf{p}}$ is the polar angle of the wave vector $\mathbf{p}$.

If impurities are dilute enough—the case we consider below—they can be considered independently. The dimensionless effective structure constant $\alpha = Ze^2/\hbar v_{\mathrm{F}}\bar{\epsilon}$ measures their coupling to Dirac states. Further, we assume positively charged impurities ($Z > 0$), and the generalization to $Z < 0$ is straightforward. Each Coulomb impurity creates numerous localized states with energies labeled by the quantum numbers n and total angular momentum j

$$\epsilon_{nj} = \frac{\Delta|n + \gamma|}{\sqrt{(n + \gamma)^2 + \alpha^2}}, \tag{2.4}$$

where $\gamma = \sqrt{j^2 - \alpha^2}$, $n = 0, 1, 2, \ldots$ for $j = 1/2, 3/2, \ldots$ and $n = 1, 2, \ldots$ for $j = -1/2, -3/2, \ldots$ (note that for $n = 0$, the states are not doubly degenerate). The wave functions of the localized states take the form

$$|\Psi_{\mathbf{x};nj}\rangle = \frac{1}{\sqrt{2\pi}} \begin{pmatrix} F^{+}_{nj}(r)e^{i(j-1/2)\theta_r} \\ -F^{-}_{nj}(r)e^{i(j+1/2)\theta_r} \end{pmatrix}, \tag{2.5}$$

where θ_r is the polar angle in real space, and the functions $F^{\pm}_{nj}(r)$ are given by [159]

$$F^{\pm}_{nj}(r) = \frac{(-1)^n \lambda^{3/2}}{\Delta\Gamma(1+2\gamma)} \sqrt{\frac{\Gamma(1+2\gamma+n)(\Delta \pm \epsilon_{nj})}{(\hbar v_{\mathrm{F}} j + \Delta\alpha/\lambda)\alpha n!}} \times (2\lambda r)^{\gamma-1/2} e^{-\lambda r} [(\hbar v_{\mathrm{F}} j + \Delta\alpha/\lambda)\mathcal{F}(-n, 1+2\gamma; 2\lambda r) \mp \hbar v_{\mathrm{F}} n \mathcal{F}(1-n, 1+2\gamma; 2\lambda r)]. \quad (2.6)$$

where $\lambda = \sqrt{\Delta^2 - \epsilon^2_{nj}}/\hbar v_{\mathrm{F}}$ and $\mathcal{F}(a, b; z) = 1 + \frac{a}{b} z + \frac{a(a+1)}{b(b+1)} \frac{z^2}{2!} + \cdots$ is the confluent hypergeometric function. It should be noted that the state with the lowest energy (which we refer to as the "lowest state" to differentiate it from the many-body ground state) is well separated from excited states that lay in the vicinity of continuum of delocalized electronic states, as seen in Fig. (2.2). Thus, we focus on the lowest state with energy $\epsilon_0 \equiv \epsilon_{0,1/2} = \Delta\sqrt{1-4\alpha^2}$ and wave functions given by Eq. (2.5) with $j = 1/2$ and

$$F^{\pm}_{0,1/2}(r) = \frac{2\alpha}{\hbar v_{\mathrm{F}}} \sqrt{\frac{2\Delta(\Delta \pm \epsilon_0)}{\Gamma(1+2\gamma)}} \left(4\alpha \frac{\Delta r}{\hbar v_{\mathrm{F}}}\right)^{\gamma-1/2} e^{-2\alpha \frac{\Delta r}{\hbar v_{\mathrm{F}}}}, \quad (2.7)$$

with an effective radius

$$a_0 = \sqrt{\langle r^2 \rangle} = \frac{\hbar v_{\mathrm{F}}}{\Delta} \frac{\sqrt{3 - 4\alpha^2 + 3\sqrt{1-4\alpha^2}}}{4\alpha} \sim \sqrt{\frac{3}{8}} \frac{\hbar v_{\mathrm{F}}}{\Delta} \frac{1}{\alpha} + O(\alpha). \quad (2.8)$$

For $\alpha \geq 0.5$, the $j = 1/2$ bound states become unstable and classically these bound electrons collapse into the "nucleus"; this has been extensively discussed in the case of Dirac fermions in graphene [160–162].

We are interested in the resonant contribution of the localized states to the optical conductivity, so we approximate the delocalized scattering states by the

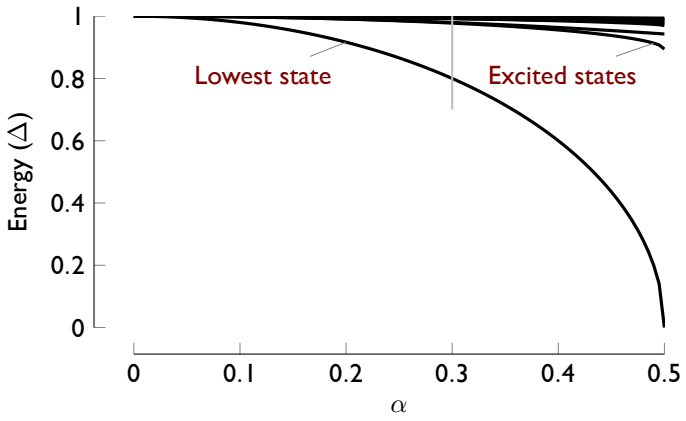

Figure 2.2: Energies of the first six states localized on a charged impurity. The vertical line represents the α we consider for our numerical results.

unperturbed delocalized ones as written in Eq. (2.3). While this approximation is not exact – the delocalized states will be modified due to the potential – it does not affect the resonant feature, which is due to the difference in energies.

2.3 Optical conductivities

The electromagnetic response on the surface of a TI is described by the optical conductivity tensor. For noninteracting electrons, this tensor can be written in the Kubo-Greenwood formulation as

$$\sigma_{\mu\nu}(\omega) = \frac{\hbar e^2}{iS} \sum_{\alpha\beta} \frac{f_\alpha - f_\beta}{\epsilon_\alpha - \epsilon_\beta} \frac{\langle\alpha|j_\mu|\beta\rangle \langle\beta|j_\nu|\alpha\rangle}{\hbar\omega + \epsilon_\alpha - \epsilon_\beta + i\delta}. \tag{2.9}$$

Here ω is the frequency of the incident electromagnetic wave, S is the surface area, and $\mathbf{j} = -\partial H/\partial \mathbf{k} = v_{\mathrm{F}}[\boldsymbol{\sigma} \times \hat{\mathbf{z}}]$ is the single-particle current operator. The sum is over all single-particle states α, including the valence band, the conduction band, and localized states with their corresponding energies ϵ_α and occupation numbers

f_α. The conductivity can be broken up into transitions between (i) surface bands, denoted by $\sigma^{\rm cv}$; (ii) a surface band and the localized states, denoted by $\sigma^{\rm imp}$; and (iii) localized states, denoted by $\sigma^{\text{imp-imp}}$. One can separate each of these contributions to the conductivity tensor as $\sigma = \sigma^{\rm cv} + \sigma^{\rm imp} + \sigma^{\text{imp-imp}}$. In this paper, the impurities contribute independently; this works well when the sample is dilute enough, i.e., given N impurities, $(N/S)a_0^2 \ll 1$.

The contribution between bands can be presented as

$$\sigma^{\rm cv}_{\mu\nu}(\omega) = -i\hbar e^2 \sum_{\mathbf{p},\gamma,\gamma'} \frac{f_{\mathbf{p},\gamma} - f_{\mathbf{p},\gamma'}}{\epsilon_{\mathbf{p},\gamma} - \epsilon_{\mathbf{p},\gamma'}} \frac{\langle \varphi_{\mathbf{p},\gamma}|j_\mu|\varphi_{\mathbf{p},\gamma'}\rangle \langle \varphi_{\mathbf{p},\gamma'}|j_\nu|\varphi_{\mathbf{p},\gamma}\rangle}{\hbar\omega + \epsilon_{\mathbf{p},\gamma} - \epsilon_{\mathbf{p},\gamma'} + i\delta}. \tag{2.10}$$

This quantity was evaluated previously and is given by [108, 109]. We also give a similar derivation at imaginary frequencies in Eqs. (4.50) and (4.51) later and these can be found from those by a rotation onto the real axis,

$$\begin{aligned}
\mathrm{Re}[\sigma^{\rm cv}_{xx}] &= \frac{e^2}{h}\frac{\pi}{8}\left[1 + \left(\frac{2\Delta}{\hbar\omega}\right)^2\right]\Theta(\hbar|\omega| - 2|\mu|), \\
\mathrm{Im}[\sigma^{\rm cv}_{xx}] &= \frac{e^2}{8h}\left\{\frac{4\Delta^2}{\hbar\omega|\mu|} + \left[1 + \left(\frac{2\Delta}{\hbar\omega}\right)^2\right]\log\left|\frac{\hbar\omega - 2|\mu|}{\hbar\omega + 2|\mu|}\right|\right\}, \\
\mathrm{Re}[\sigma^{\rm cv}_{xy}] &= \frac{e^2}{4h}\frac{2\Delta}{\hbar\omega}\log\left|\frac{\hbar\omega - 2|\mu|}{\hbar\omega + 2|\mu|}\right|, \\
\mathrm{Im}[\sigma^{\rm cv}_{xy}] &= -\frac{e^2}{h}\frac{\pi}{4}\frac{2\Delta}{\hbar\omega}\Theta(\hbar|\omega| - 2|\mu|),
\end{aligned} \tag{2.11}$$

assuming $|\mu| \geq \Delta$ (if $|\mu| < \Delta$, let $\mu \to \Delta$ in these expressions).

The localized states on the Coulomb impurities are labeled by $\lambda = (\mathbf{r}_i, n, j)$, and their matrix elements can be presented in the following form:

$$\begin{aligned}
\langle \mathbf{p} \pm |j_\mu|\lambda\rangle &= \int d^2x \, \langle \varphi_{\mathbf{p},\pm}|j_\mu|\Psi_{\mathbf{x}-\mathbf{r}_i;nj}\rangle \, e^{i\mathbf{p}\cdot\mathbf{x}/\hbar} \\
&= e^{i\mathbf{p}\cdot\mathbf{r}_i} \langle \varphi_{\mathbf{p}\pm}|j_\mu|\Psi_{\mathbf{p};nj}\rangle \,,
\end{aligned} \tag{2.12}$$

where $|\Psi_{\mathbf{p};nj}\rangle$ is the Fourier transform of $|\Psi_{\mathbf{x};nj}\rangle$. The expression for $\sigma_{\mu\nu}^{\rm imp}$ can be further split,

$$\sigma_{\mu\nu}^{\rm imp} = \sigma_{\mu\nu}^{\rm imp+} + \sigma_{\mu\nu}^{\rm imp-}. \tag{2.13}$$

Here $\sigma_{\mu\nu}^{\rm imp+}$ ($\sigma_{\mu\nu}^{\rm imp-}$) denotes the contribution due to excitations from localized states to the conduction band (from the valence band to localized states), which is nonzero if the localized state is filled (empty). They can both be presented in the form

$$\sigma_{\mu\nu}^{\rm imp\pm} = \frac{N\hbar e^2}{iS}\sum_{\epsilon_\lambda \lessgtr \mu}\sum_{\mathbf{p}} \frac{f_\lambda^{\pm} - f_{\mathbf{p}\pm}}{\epsilon_\lambda \mp \epsilon_{\mathbf{p}}} \times \left[\frac{\langle\lambda|j_\mu|\mathbf{p}\pm\rangle\,\langle\mathbf{p}\pm|j_\nu|\lambda\rangle}{\hbar\omega \pm \epsilon_{\mathbf{p}} - \epsilon_\lambda + i\delta} + \frac{\langle\mathbf{p}\pm|j_\mu|\lambda\rangle\,\langle\lambda|j_\nu|\mathbf{p}\pm\rangle}{\hbar\omega + \epsilon_\lambda \mp \epsilon_{\mathbf{p}} + i\delta}\right]. \tag{2.14}$$

Here we have summed over all Coulomb impurities. The phase factor in Eq. (2.12) depends on the position of the impurity and is canceled in the product of matrix elements in Eq. (2.14). Integrating the matrix elements over the angle of $\mathbf{p}$ and changing variables from p to $\epsilon_p \equiv \epsilon$ while taking into account the occupation of the bands, we obtain

$$\sigma_{xx}^{\rm imp\pm} = \frac{iN\hbar e^2}{S}\sum_{\epsilon_\lambda \lessgtr \mu}\int_{\max\{|\mu|,\Delta\}}^{\infty} \frac{\epsilon\, d\epsilon}{(2\pi\hbar v_{\rm F})^2}\frac{M_{xx}^{\lambda\pm}(\epsilon)}{\epsilon \mp \epsilon_\lambda} \times \left[\frac{1}{\hbar\omega \pm \epsilon - \epsilon_\lambda + i\delta} + \frac{1}{\hbar\omega + \epsilon_\lambda \mp \epsilon + i\delta}\right], \tag{2.15}$$

$$\sigma_{xy}^{\rm imp\pm} = \frac{N\hbar e^2}{S}\sum_{\epsilon_\lambda \lessgtr \mu}\int_{\max\{|\mu|,\Delta\}}^{\infty} \frac{\epsilon\, d\epsilon}{(2\pi\hbar v_{\rm F})^2}\frac{M_{xy}^{\lambda\pm}(\epsilon)}{\epsilon \mp \epsilon_\lambda} \times \left[\frac{1}{\hbar\omega \pm \epsilon - \epsilon_\lambda + i\delta} - \frac{1}{\hbar\omega + \epsilon_\lambda \mp \epsilon + i\delta}\right], \tag{2.16}$$

where we defined

$$M_{xx}^{\lambda\pm}(\epsilon) \equiv \int_0^{2\pi} d\vartheta_p \, |\, \langle \mathbf{p} \pm |j_x| \lambda \rangle \, |^2, \tag{2.17}$$

$$M_{xy}^{\lambda\pm}(\epsilon) \equiv i \int_0^{2\pi} d\vartheta_p \, \langle \mathbf{p} \pm |j_x| \lambda \rangle \, \langle \lambda | j_y | \mathbf{p} \pm \rangle \, , \tag{2.18}$$

and we used the fact that these are real functions.

To evaluate these, we use Eq. (2.12). In position space, the bound state $|\lambda\rangle$ is of the form shown in Eq. (2.5) (centered around $\mathbf{r}_i$), so the Fourier transform takes the corresponding form

$$|\Psi_{\mathbf{p};nj}\rangle = \sqrt{2\pi} \begin{pmatrix} \tilde{F}_{nj}^{+}(p) e^{i\theta_p (j-1/2)} \\ i \tilde{F}_{nj}^{-}(p) e^{i\theta_p (j+1/2)} \end{pmatrix} \tag{2.19}$$

where $\tilde{F}_{nj}^{\pm}(p) = \int_0^\infty dr \, r F_{nj}^{\pm}(r) J_{j\mp 1/2}(pr/\hbar)$ are Hankel transforms of their real-space counterparts (which can be analytically evaluated given Eq. (2.7)).

In terms of these objects, we can evaluate the integrated matrix elements

$$M_{xx}^{\lambda\pm}(\epsilon) = \frac{(2\pi v_{\mathrm{F}})^2}{2\epsilon} [(\epsilon \mp \Delta) |\tilde{F}_{nj}^{+}(p)|^2 + (\epsilon \pm \Delta) |\tilde{F}_{nj}^{-}(p)|^2]$$

$$M_{xy}^{\lambda\pm}(\epsilon) = \frac{(2\pi v_{\mathrm{F}})^2}{2\epsilon} [(\epsilon \mp \Delta) |\tilde{F}_{nj}^{+}(p)|^2 - (\epsilon \pm \Delta) |\tilde{F}_{nj}^{-}(p)|^2]$$

with $p = \sqrt{\epsilon^2 - \Delta^2}/v_{\mathrm{F}}$.

Considering just the lowest state with $n = 0$ and $j = 1/2$ (labeled with $\lambda = 0$), we obtain

$$M_{xx}^{0\pm}(\epsilon) + M_{xy}^{0\pm}(\epsilon) = \frac{2^\gamma (2\pi v_{\mathrm{F}})^2}{4\alpha^2} \left(\frac{\hbar v_{\mathrm{F}}}{\Delta} \right)^2 \frac{\Gamma\left(\gamma + \frac{3}{2}\right)^2}{\Gamma(2\gamma + 1)} \frac{(\epsilon \mp \Delta)(\Delta + \epsilon_0)}{\epsilon \Delta} \times {}_2F_1 \left(a_\gamma, a_\gamma + \tfrac{1}{2}; 1; \frac{\Delta^2 - \epsilon^2}{4\alpha^2 \Delta^2} \right)^2 \tag{2.20}$$

$$M_{xx}^{0\pm}(\epsilon) - M_{xy}^{0\pm}(\epsilon) = \frac{2^\gamma (2\pi v_{\rm F})^2}{64\alpha^4} \left(\frac{\hbar v_{\rm F}}{\Delta}\right)^2 \frac{\Gamma\left(\gamma+\frac{5}{2}\right)^2}{\Gamma(2\gamma+1)} \frac{(\epsilon\pm\Delta)(\epsilon^2-\Delta^2)(\Delta-\epsilon_0)}{\epsilon\Delta^3} \times {}_2F_1\left(a_\gamma+\tfrac{1}{2}, a_\gamma+1; 2; \frac{\Delta^2-\epsilon^2}{4\alpha^2\Delta^2}\right)^2 \quad (2.21)$$

where $a_\gamma = (2\gamma+3)/4$ and ${}_2F_1$ is the (analytic continuation of the) hypergeometric function ${}_2F_1(a,b;c;x) = 1 + \frac{ab}{c}\frac{x}{1!} + \frac{a(a+1)b(b+1)}{c(c+1)}\frac{x^2}{2!} + \cdots$.

If two bound states are at different positions, then by our diluteness assumption (insignificant wave-function overlap) transitions between them will *not* contribute to the conductivity significantly. However, if the chemical potential is in between two bound states that live at the *same* position (e.g. the ground and excited states of a single impurity), then transitions between those states can contribute to the conductivity; this contribution is given by

$$\sigma_{xx}^{\text{imp-imp}} = N\frac{\hbar e^2}{iS} \sum_{\substack{\epsilon_{nj}<\mu \\ \epsilon_{mj'}>\mu}} \frac{(\Phi_{mj'}^{nj})^2\delta_{j+1,j'} + (\Phi_{nj}^{mj'})^2\delta_{j,j'+1}}{\epsilon_{nj}-\epsilon_{mj'}} \times \left[\frac{1}{\hbar\omega+\epsilon_{nj}-\epsilon_{mj'}+i\delta} + \frac{1}{\hbar\omega+\epsilon_{mj'}-\epsilon_{nj}+i\delta}\right], \quad (2.22)$$

and

$$\sigma_{xy}^{\text{imp-imp}} = N\frac{\hbar e^2}{S} \sum_{\substack{\epsilon_{nj}<\mu \\ \epsilon_{mj'}>\mu}} \frac{(\Phi_{mj'}^{nj})^2\delta_{j+1,j'} - (\Phi_{nj}^{mj'})^2\delta_{j,j'+1}}{\epsilon_{nj}-\epsilon_{mj'}} \times \left[\frac{1}{\hbar\omega+\epsilon_{nj}-\epsilon_{mj'}+i\delta} - \frac{1}{\hbar\omega+\epsilon_{mj'}-\epsilon_{nj}+i\delta}\right], \quad (2.23)$$

where we have defined

$$\Phi_{mj'}^{nj} \equiv v_{\rm F}^2 \int_0^\infty r dr\, F_{mj'}^+(r) F_{nj}^-(r). \quad (2.24)$$

The integral in Eq. (2.24) can be calculated analytically for the functions given in Eq. (2.6); the result is in terms of Appell hypergeometric functions and can

be calculated with the use of an integral identity[2]. Notice that transitions can only occur between states that only differ by a quantum of angular momentum as expected from the form of the single-particle current operator. For our calculations, we do not consider these transitions since the higher excited states merge with the continuum – leading to at most a decreasing and smoothing of the threshold.

For the calculation of the frequency-dependent conductivities shown in Fig. 2.4, we use the dimensionless parameters $\alpha = 0.3$, $(N/S)a_0^2 = 0.035$. For a charge on the surface of a bulk TI, $\alpha \sim 0.09Z$; however, in a thin film geometry where the localized state has a radius $a_0 \gtrsim d$, where d is the thickness of the thin film, the situation is more complicated. If $a_0 \gg d$, then we expect $\alpha \sim 3.5Z$, but we are in an intermediate region where the energy level due to the more complicated potential (see Eq. (2.2)) is more accurately captured by $\alpha \sim 0.3Z$. Also, we use four values of the chemical potential corresponding to four different occupation situations, illustrated in Fig. 2.3. In-gap states correspond to resonance features in Figs. 2.4a and 2.4b which are well below the threshold of $2\max(\Delta, |\mu|)$. If the in-gap states are empty, an additional peak appears at $\epsilon_0 + \max\{\Delta, |\mu|\}$. If they are occupied, it appears at frequency $\max\{\Delta, |\mu|\} - \epsilon_0$. The shape of the resonance depends weakly

[2] The relevant integral is

$$\int_0^\infty dr\, e^{-br} r^{\gamma-1} \mathcal{F}(\alpha_1; \beta_1; a_1 r) \mathcal{F}(\alpha_2; \beta_2; a_2 r) = \frac{\Gamma(\gamma)}{b^\gamma} F_2(\gamma; \alpha_1, \alpha_2; \beta_1, \beta_2; \tfrac{a_1}{b}, \tfrac{a_2}{b}), \tag{2.25}$$

where F_2 is the Appell hypergeometric function defined by the series

$$F_2(\gamma; \alpha_1, \alpha_2; \beta_1, \beta_2; x_1, x_2) = \sum_{n,m=0}^{\infty} \frac{(\gamma)_{n+m} (\alpha_1)_n (\alpha_2)_m}{(\beta_1)_n (\beta_2)_m} \frac{x_1^n}{n!} \frac{x_2^m}{m!}, \tag{2.26}$$

with $(a)_n = a(a+1)\cdots(a+n-1)$ being the Pochhammer symbol.

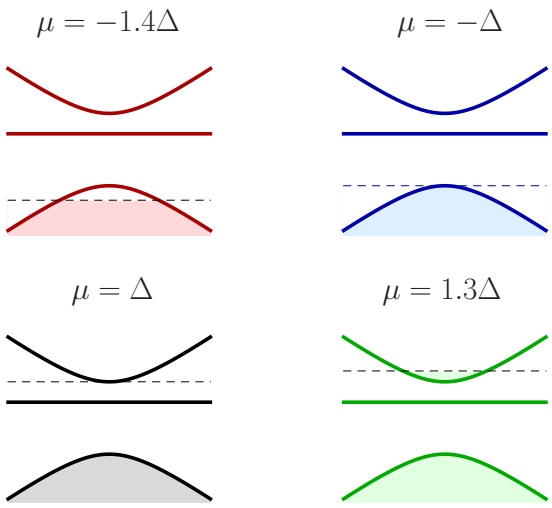

Figure 2.3: The four cases for the chemical potential. The solid line in the middle of the gap is the bound state.

on the value of the chemical potential, and its height disappears at $\mu/|\Delta| \gg 1$. Thus, the main role of the chemical potential, if it is outside the gap, is the shifting of resonant frequencies, and in the next section, which discusses the magneto-optical effects of a topological insulator film, we exclusively consider the chemical potential to be situated inside the gap.

It should be noted that in the above calculation, we neglected the Drude contribution, which appears if the chemical potential lies outside the gap. The Drude contribution dominates transport, but it is not as important for the optical conductivity at frequencies $\omega \gg 1/\tau$. We further assume that we have only one localized state, namely the lowest bound state in Eq. (2.7). The excited in-gap states violate the diluteness criterion: electrons can hop between these states due to significant wave-function overlap, hence these states will merge with continuum of delocalized states.

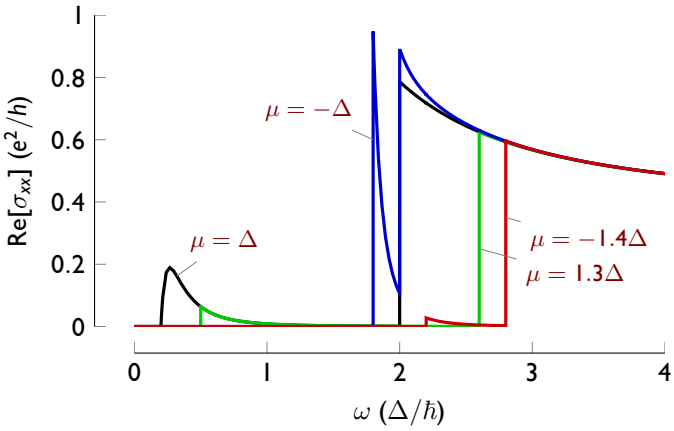

(a) Longitudinal conductivities.

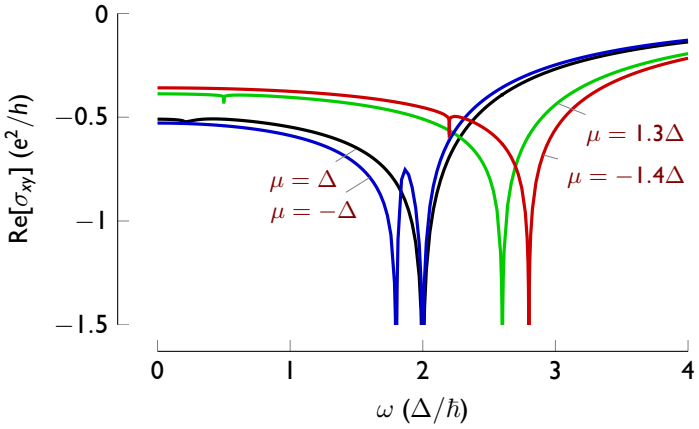

(b) Hall conductivities.

Figure 2.4: Given the four positions of the chemical potential illustrated in Fig. 2.3, Coulomb coupling $\alpha = 0.3$, and a density of $N/S = 0.035a_0^2$; (a) and (b) show the longitudinal and Hall conductivities, respectively. Note that the largest features are at $2|\mu|$, when the electromagnetic waves excite electrons from the valence to the conduction band. The lower-frequency features occur when electromagnetic waves excite electrons from the valence to the bound states ($\mu \leq -\Delta$) or when electromagnetic waves excite electrons from the bound state to the conduction band ($\mu \geq \Delta$).

2.4 Faraday and Kerr effects

We consider the Faraday and Kerr effects at normal incidence and in a thin film geometry. These conditions are the most favorable for observing the effects of surface states on the optics. While the Faraday and Kerr effects are quite insensitive to oblique incidence [163], they decrease considerably (especially the Kerr effect) in the presence of a mismatch of dielectric constants on the TI film surfaces and due to longitudinal conductivity [109, 164]. This mismatch—of bulk dielectric constant to surface effects—can be neglected only if the film thickness is considerably smaller than the optical wavelength in it, $d \ll \lambda/\epsilon_{\mathrm{TI}}$. In real samples, the bulk contributes considerably to the longitudinal conductivity, which could be reduced in TI films. Further, we assume that the direction of the exchange field (sign of Δ) is the same on each surface of the TI; in the opposite case, the effects of both plates on the optics cancel one another.

In experiments, the incident wave is usually linearly polarized, $\mathbf{E} = E_0\hat{\mathbf{x}}$. Looking in the Appendix A, for the calculation of the reflection matrix, we see that for $\omega = ck_z$, $\sigma_{xx}^{\mathrm{tot}} = \sigma_{yy}^{\mathrm{tot}}$, and $\sigma_{xy}^{\mathrm{tot}} = -\sigma_{yx}^{\mathrm{tot}}$ that

$$\begin{aligned}
\mathbf{E}_r &= E_0 \frac{\left[\frac{\sigma_{xx}^{\mathrm{tot}}}{2c} + \left(\frac{\sigma_{xx}^{\mathrm{tot}}}{2c}\right)^2 + \left(\frac{\sigma_{xy}^{\mathrm{tot}}}{2c}\right)^2\right]\hat{\mathbf{x}} + \frac{\sigma_{xy}^{\mathrm{tot}}}{2c}\hat{\mathbf{y}}}{1 + 2\frac{\sigma_{xx}^{\mathrm{tot}}}{2c} + \left(\frac{\sigma_{xx}^{\mathrm{tot}}}{2c}\right)^2 + \left(\frac{\sigma_{xy}^{\mathrm{tot}}}{2c}\right)^2}, \\
\mathbf{E}_t &= E_0 \frac{\left[1 + \frac{\sigma_{xx}^{\mathrm{tot}}}{2c}\right]\hat{\mathbf{x}} + \frac{\sigma_{xy}^{\mathrm{tot}}}{2c}\hat{\mathbf{y}}}{1 + 2\frac{\sigma_{xx}^{\mathrm{tot}}}{2c} + \left(\frac{\sigma_{xx}^{\mathrm{tot}}}{2c}\right)^2 + \left(\frac{\sigma_{xy}^{\mathrm{tot}}}{2c}\right)^2}.
\end{aligned} \tag{2.27}$$

For calculational purposes, it is convenient to present the incident wave as a combination of two circularly polarized waves and calculate their reflection $r_\pm = |r_\pm| e^{i\Phi_\pm^r}$

and transmission $t_\pm = |t_\pm| e^{i\Phi^t_\pm}$ amplitudes. In this basis, the reflected and transmitted waves are, respectively, $\mathbf{E}_r = E_0(r_+\mathbf{e}_+ + r_-\mathbf{e}_-)$ and $\mathbf{E}_t = E_0(t_+\mathbf{e}_+ + t_-\mathbf{e}_-)$, where $\mathbf{e}_\pm = \hat{\mathbf{x}} \pm i\hat{\mathbf{y}}$ represent the two directions of circular polarization. The transmittance through the film is given by $T = (|t_+|^2 + |t_-|^2)/2$; the transmitted wave's polarization rotates through an angle $\vartheta_\mathrm{F} = (\Phi^t_+ - \Phi^t_-)/2$ (the Faraday angle) and has ellipticity $\delta_\mathrm{F} = (|t_+| - |t_-|)/(|t_+| + |t_-|)$; and the reflected wave's polarization rotates through an angle $\vartheta_\mathrm{K} = (\Phi^r_+ - \Phi^r_-)/2$ (the Kerr angle) and has ellipticity $\delta_\mathrm{K} = (|r_+| - |r_-|)/(|r_+| + |r_-|)$.

Using the form of $\mathbf{E}_r$ and $\mathbf{E}_t$ calculated in Eq. (2.27), we can find the values for the reflected and transmitted circular polarizations as described above. They are given by

$$t_\pm = \frac{e^2/h}{e^2/h + \alpha_0 \sigma^\mathrm{tot}_\pm}, \qquad r_\pm = -\frac{\alpha_0 \sigma^\mathrm{tot}_\pm}{e^2/h + \alpha_0 \sigma^\mathrm{tot}_\pm}, \tag{2.28}$$

where $\sigma^\mathrm{tot}_\pm = \sigma^\mathrm{tot}_{xx} \mp i\sigma^\mathrm{tot}_{xy}$, e^2/h is the quantum of conductance, and $\alpha_0 \approx 1/137$ is the fine-structure constant. Additionally, both sides of the thin film contribute to the optical conductivity, so $\sigma^\mathrm{tot}_{\mu\nu} = 2\sigma_{\mu\nu}$. If we expand in the fine-structure constant, we have $\vartheta_\mathrm{F} \sim 2\alpha_0 \operatorname{Re}\sigma_{xy}/(e^2/h)$, $\delta_\mathrm{F} \sim 2\alpha_0 \operatorname{Im}\sigma_{xy}/(e^2/h)$, and $T \sim 1 - 4\alpha_0 \operatorname{Re}\sigma_{xx}/(e^2/h)$. Thus, these quantities track the respective optical conductivities quite well.

For the numerical calculations, we have used the following parameters, in addition to the dimensionless parameters taken previously [$\alpha = 0.3$ and $(N/S)a_0^2 = 0.035$]. We take the parameters for Bi_2Se_3 for the gap to be the maximum achievable by magnetic doping [100], $\Delta = 25\,\mathrm{meV}$, and Fermi velocity, $v_\mathrm{F} = 6.2 \times 10^5\,\mathrm{m/s}$.

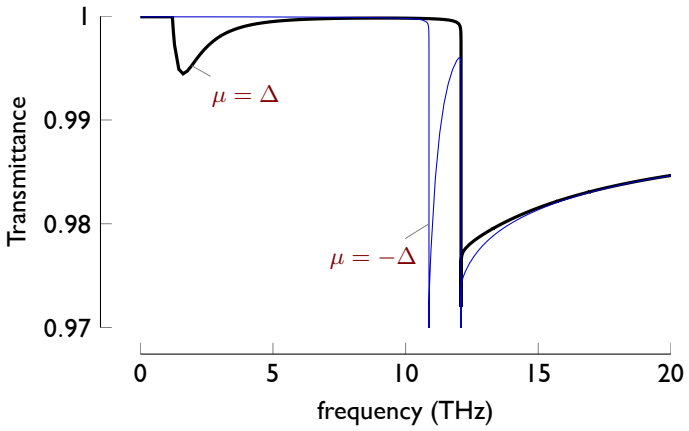

Figure 2.5: The transmittance of the electromagnetic wave for a thin film of Bi_2Se_3 in the case of a filled valence band and an unoccupied bound state ($\mu = -\Delta$) and an occupied bound state ($\mu = \Delta$).

With these numbers, our density is $N/S = 38\,\mu\text{m}^{-2}$ and $a_0 = 30\,\text{nm}$. It should be noted that N/S is *not* the total concentration of impurities, but the concentration of impurity states with a definite energy ϵ_0 inside the gap. The generalization to the realistic case is discussed in the Conclusions.

The dependence of transmittance on frequency is presented in Fig. 2.5. As one can easily see, the in-gap states lead to absorption below the threshold (i.e. when $\hbar\omega \sim 2|\mu|$), but it is small, not impeding the observation of transmission. The decrease can be understood from the relation of the longitudinal conducitivity to transmission, and hence why even magneto-optically inactive states affect transmission.

The Faraday and Kerr angles' dependence on frequency is presented in Figs. 2.6a and 2.7a respectively. As with transmittance, the largest feature is at the threshold. Since the Faraday angle strongly depends on the real part of the Hall conductivity,

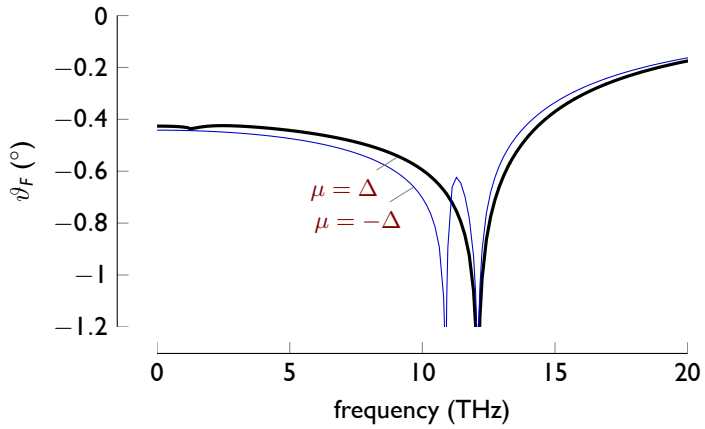

(a)

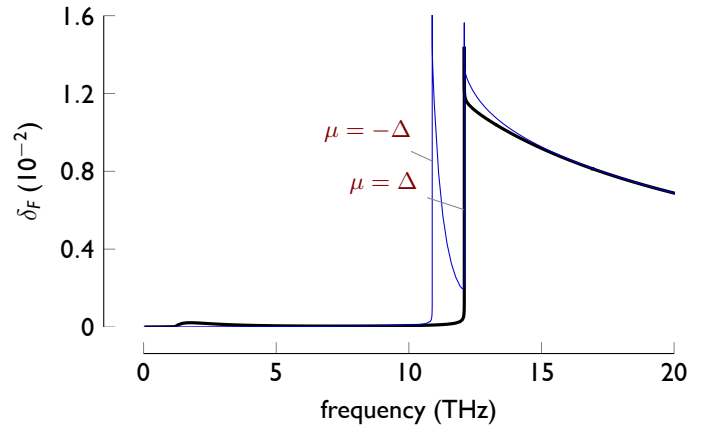

(b)

Figure 2.6: The measurable optical quantities of (a) the Faraday angle and (b) the ellipticity of the transmitted wave for Bi_2Se_3 in the case of a filled valence band with an unoccupied bound state ($\mu = -\Delta$) and an occupied bound state ($\mu = \Delta$). The features correspond to the features in the optical conductivities.

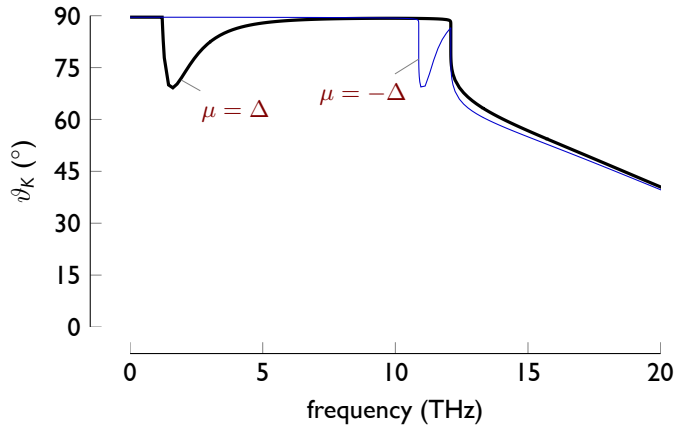

(a)

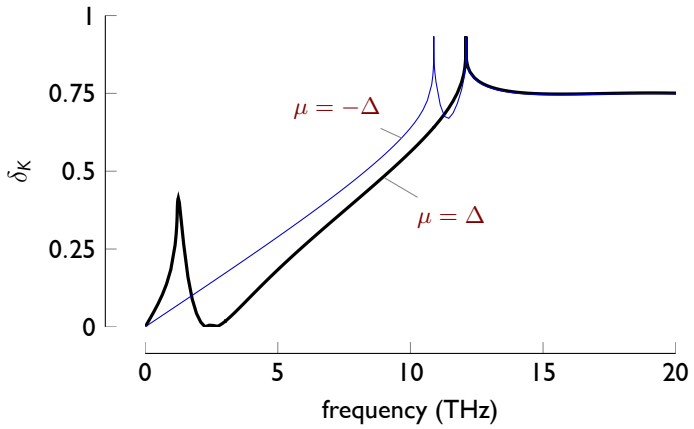

(b)

Figure 2.7: The measurable optical quantities of (a) the Kerr angle and (b) the ellipticity of the reflected wave for Bi_2Se_3 in the case of a filled valence band with an unoccupied bound state ($\mu = -\Delta$) and an occupied bound state ($\mu = \Delta$). The features correspond to the features in the optical conductivities.

we see that it matches it and has a similar resonant structure. The Kerr angle is more sensitive to the real part of the longitudinal conductivity though and we see corresponding features at these points – decreasing the Kerr angle from its large 90° rotation at zero frequency when the frequency is on resonance with the localized state. In both cases, the effect due to impurities is similar in nature to the resonant feature at threshold $\omega = 2\Delta$.

Lastly, we show the frequency dependence of ellipticities of transmitted and reflected waves in Figs. 2.6b and 2.7b respectively. Again, we see features when the incident electromagnetic wave is on resonance with the impurity state. The ellipticity of the transmitted wave follows the imaginary part of the Hall conductivity, and the reflected wave again is quite sensitive to resonant effects. Thus, in-gap states can be probed effectively with ellipsometry.

2.5 Conclusions

We have shown that in-gap localized states dominate both the absorption and magneto-optics for TI films with magnetically gapped surfaces. In particular, they lead to peculiar resonances in the frequency dependencies of the Faraday and Kerr effects. This is similar to magnetic semiconductors [111], though in non-magnetic semiconductors in-gap states usually require a magnetic field to become magneto-optically active. In the system considered in this paper, the surface spectrum does not respect time-reversal symmetry due to the gap induced by exchange field. Hence, we can conclude that the effect we observe is insensitive to details such as electron-

hole asymmetry [165], hexagonal corrections [166] to the Dirac spectrum, or to the profile of impurity potential which we assumed to be the Coulomb potential. We also assumed that all Coulomb impurities have the same charge and are located on the surface of TI; they can also be in the bulk of the TI, and their coupling to the electronic Dirac states will depend on their distance to the surface. If they are dilute enough, they will also contribute to the optical conductivity, which can be represented as

$$\sigma_{\mu\nu}^{\mathrm{imp}}(\omega) = \int_{-|\Delta|}^{|\Delta|} d\epsilon_0 P(\epsilon_0) \sigma_{\mu\nu}^{\mathrm{imp}}(\omega, \epsilon_0), \tag{2.29}$$

where $\sigma_{\mu\nu}^{\mathrm{imp}}(\omega, \epsilon_0)$ is the contribution of a single impurity bound sates with energy ϵ_0 and $P(\epsilon_0)$ is the concentration of the corresponding states. The finite distribution of levels, originating from different coupling of impurities with Dirac states, can make the calculated resonance features shallower and considerably wider. Additionally, there are variations of the chemical potential $\delta\mu$ which correspond to electron and hole puddles for $\delta\mu > 2\Delta$ [167, 168]. For $\delta\mu < 2\Delta$, the variations can bring about variation of the occupation numbers of impurity states in different regions which does not qualitatively modify our results. For our results to qualitatively still make sense, we require the variations in the chemical potential $\delta\mu < 2\Delta$.

There have been multiple optical experiments probing topological insulators that measure the Kerr and Faraday effects. Jenkins *et al.* studied the Kerr effect and reflectivity for a fixed frequency and varying the magnetic field [19]. Time-domain spectroscopy has been utilized on strained HgTe [169, 170]. The large Kerr effect and thickness independent Drude peaks have also been observed [171]. Additionally,

the quantized Faraday angle has been seen with passivated Bi_2Se_3 in a terahertz experiment as well as observation of a shifted Dirac cone [172, 173]. Time-domain spectroscopy was also used in BSTS to see both the surface state and a bulk impurity band [174]. Recently, the same technique was used on $(Bi_{1-x}In_x)_2Se_3$ to observe a topological phase transition as x is varied [175]. At present, all observed features originate from the bulk physics, but recently new ultrathin magnetically gapped TI films have been grown [176, 177], and for these samples all conditions necessary for the observation of magneto-optical effects are satisfied.

In these ultrathin films, the tunneling between opposite surfaces can become important. The tunneling splits the bands and "splits" the threshold, leading to features [178] similar to impurity states.

Resonant features from localized in-gap states and from chiral excitons appear below the threshold $2|\Delta|$, but their shapes have completely different characters. The localized impurity states are single-particle excitations while excitons are two-particle excitations. *Continuous* transitions from a valence band to a localized state (or from the localized state to a conduction band) contribute to optical conductivity, hence the additional peak can be interpreted as a splitting of the threshold $2|\Delta| \rightarrow |\Delta| + \epsilon_0$ (or to $|\Delta| - \epsilon_0$ if the state is occupied). On the other hand, excitons lead to a *sharp* feature in the two-particle spectrum, corresponding to their dispersion law $E_{\mathrm{ex}}(q)$. Since only excitons with zero momentum are optically active, they lead to features of a single, resonant shape in the magneto-optics [1].

To conclude, we have investigated the role of localized in-gap states on the surface of a topological insulators in the magneto-optical Faraday and Kerr effects.

These in-gap states resonantly contribute to both the longitudinal and Hall conductivities which in turn leads to peculiar resonances in the frequency dependence of the Faraday and Kerr angles as well as to the ellipticities of transmitted and reflected waves. These resonant features that we have predicted can be directly measured by optical experiments. In fact, their specific shape of these resonant features allows them to be easily separated from other in-gap excitations.

Chapter 3: Observation of material phenomena with the Casimir effect

3.1 Overview

In this chapter we mainly concern ourselves with materials tangentially related to the topological materials present in Chapter 2 and Chapter 4. We show how specific material phenomena, specifically topological Lifshitz transitions and weak localization in two-dimensions, can appear as a distinct signature in a Casimir force experiment. This chapter is largely taken from the papers[1] [4] and [5], copyright APS.

3.2 Nonanalytic behavior of the Casimir force across a Lifshitz transition in a spin-orbit-coupled material

Within the paradigm of observing material phenomena with the Casimir effect (see discussion in Sec. 1.2), we consider how the Casimir force changes as a parameter tunes a system across a Lifshitz transition—an extreme case of Fermi

[1] In this chapter, the technical results were obtained in large part by my coauthor on these papers and fellow graduate student Andrew Allocca.

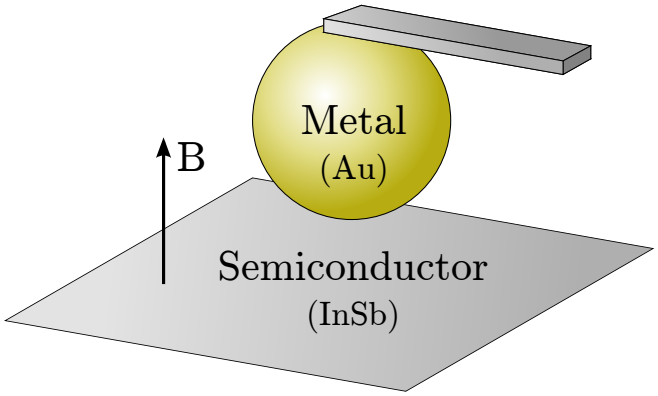

Figure 3.1: The geometry typically used in experimental measurements of the Casimir force is a gold-coated sphere suspended above a planar plate from a cantilever. We consider a lower plate of indium antimonide with an applied magnetic field.

surface reconstruction in an electronic material (see Sec. 1.4.1). We find that as the system goes through this transition by tuning a magnetic field, the Casimir force is both nonanalytic and nonmonotonic as a function of the field. Our model involves a thin layer of indium antimonide (or another semiconductor with a large g factor, as discussed below) and could be experimentally realized in the common experimental setup for Casimir measurements as shown in Fig. 3.1. In this section, we consider how the Casimir force changes as we tune a two-dimensional spin-orbit-coupled material through a Lifshitz transition.

Others have considered the consequences on the Casimir effect of considering two-dimensional plates instead of thick slabs [179–181], but similar to the particular case of graphene [182–184], our model requires a more microscopic approach. We consider the Casimir force at zero temperature between two parallel plates where at

least one is modeled as a two-band spin-orbit-coupled material (sufficiently thin to be considered quasi-two-dimensional) with a fixed chemical potential and tunable Zeeman splitting due to an external magnetic field. (When considering only one spin-orbit-coupled plate, the other is a metallic plate, modeled as a clean free electron gas.) The Zeeman field tunes a gap in this two-band material and causes one of the Fermi surfaces to form or collapse. This is the simplest realistic model exhibiting a Lifshitz transition. At these transition points, the Casimir force between the two plates experiences a kink, as seen in Fig. 3.2.

This could be experimentally measured with the usual plate and sphere geometry as seen in Fig. 3.1. The plate would be a thin layer of InSb while the sphere would be the usual Au-coated sphere. While we consider the parallel plate scenario, our calculations can be generalized to the sphere-plate geometry by using the proximity force approximation [23] without damage to the nonanalyticity we observe in the Casimir force.

3.2.1 Clean spin-orbit coupled materials response function

We consider the single-particle effective Hamiltonian for the conduction bands of the semiconductor,

$$H = \frac{k^2}{2m^*} - \mu + \beta(\sigma_x k_x - \sigma_y k_y) + V_z \sigma_z, \tag{3.1}$$

which has eigenvalues

$$\xi^{\pm}(k) = \frac{k^2}{2m^*} - \mu \pm \sqrt{V_z^2 + \beta^2 k^2}, \tag{3.2}$$

where m^* and μ are the conduction band effective mass of the electron and chemical potential. The coefficient β is the strength of the Dresselhaus spin-orbit coupling, and σ_i are the Pauli matrices. The factor V_z is the induced Zeeman splitting, given by $V_z = \mu_B g^* B$, where μ_B is the Bohr magneton, g^* is the material's g factor, and B is an applied magnetic field. For all calculations we assume that this Hamiltonian is a simple model of the relevant bands of the material indium antimonide, for which $m^* = 0.014 m_0$, where m_0 is the free electron mass, and $\beta = \gamma \langle k_z^2 \rangle \simeq \gamma \left(\frac{\pi}{d}\right)^2$ [185], where d is the thickness of the plate and $\gamma = 760.1\,\mathrm{eV\AA}^3$ is the intrinsic Dresselhaus parameter for the material. We consider InSb plates that are six lattice constants thick, $d = 6 \times 0.6479\,\mathrm{nm} = 3.89\,\mathrm{nm}$. The plates may still be considered effectively two-dimensional (2D) as long as the energy needed to excite higher electron modes in the confined direction is much larger than the energy required to excite the two lowest bands modeled here. Additionally, since the g factor of InSb is $g^* = -51.6$ we can also neglect the orbital coupling of the electrons directly to the external magnetic field as well as the effect of the magnetic field on the metallic plate when it is considered [186].

For $\mu > |V_z|$ there are two bands crossing the Fermi energy. With fixed μ, as $|V_z|$ is increased the occupation of the upper band decreases until the Fermi surface disappears entirely when $|\mu| = |V_z|$ – the electron pocket defined by that Fermi surface disappears. Increasing the Zeeman splitting further, the Fermi energy lies within the gap and only the lower band crosses the Fermi level, giving a single Fermi surface. This represents the Lifshitz transition for $\mu > 0$, and is shown with the red dashed line in the insets of Fig. 3.2.

If $m^*\beta^2 > |V_z|$ the lower band has a local maximum at $k = 0$ and a similar scenario can be considered for $\epsilon_{\min} < \mu < -|V_z|$, where $\epsilon_{\min}$ is the lowest energy of the lower band. In this case, the lower band crosses the Fermi energy for two distinct values of k, producing two Fermi surfaces – the inner one enclosing a hole pocket. Again, increasing $|V_z|$ for fixed μ leads to a shrinking of the inner Fermi surface until it disappears completely at the point when $|\mu| = |V_z|$. For larger Zeeman splitting, the Fermi energy again lies within the gap and there is a single Fermi surface. This senario for $\mu < 0$ is shown with the blue dashed line in the insets of Fig. 3.2. The disappearance of a Fermi surface by changing V_z in these two scenarios are simple examples of a Zeeman-driven Lifshitz transition.

Since these transitions occur at a specific value of $|V_z|$, regardless of the sign of V_z, the direction of the applied magnetic field is unimportant. For this reason, we always assume $V_z > 0$ for simplicity. We also denote the magnetic field strength needed to reach the Lifshitz transition point as $B_L = \frac{|\mu|}{g\mu_B}$.

We determine the bare correlation function using the current operator, $j_i(x) = \psi^\dagger(x)\frac{\partial \hat{H}[A]}{\partial A_i(x)}\psi(x)$, where $\hat{H}[A]$ is the Hamiltonian given in Eq. (3.1) after minimal coupling. The correlation function is then expressed in terms of the current as

$$\Pi_{ij}(x, x') = \langle -\delta(x - x')\delta_{ij}\partial_{A_i} j_i(x) + j_i(x)j_j(x')\rangle\Big|_{A=0}, \tag{3.3}$$

where $\langle \cdots \rangle$ represents averaging over the ground state [136]. In the case of a weakly correlated system we can use the approximation that the Casimir effect is determined by the local current-current response functions; i.e., we need to consider only the $q = 0$ limit of $\hat{\Pi}$ since nonlocal behavior is screened out. Equivalently, this is a simple

extension of the usual plasma model to a spin-orbit-coupled Hamiltonian, which describes the plates. Furthermore, coupling of the spin to the magnetic fluctuations of the vacuum field do not need to be considered. In this limit, the correlation function for the spin-orbit-coupled plates has the form

$$\hat{\Pi}(i\omega) = -\frac{e^2}{h}\begin{pmatrix} \Pi_L(i\omega) & \Pi_H(i\omega) \\ -\Pi_H(i\omega) & \Pi_L(i\omega) \end{pmatrix}, \tag{3.4}$$

where e^2/h is the quantum of conductance,

$$\Pi_H(i\omega) = V_z\left[\cot^{-1}\left(\frac{\omega}{2\epsilon^+}\right) - \cot^{-1}\left(\frac{\omega}{2\epsilon^-}\right)\right] \tag{3.5}$$

$$\Pi_L(i\omega) = \mu\left[\Theta(\mu - |V_z|) + \Theta(\mu + |V_z|)\right] + \frac{\epsilon^+ - \epsilon^-}{2} + \frac{\omega^2 - 4V_z^2}{4V_z\omega}\Pi_H(i\omega)$$

and $\epsilon^{\pm}$ are the positive square roots of

$$(\epsilon^{\pm})^2 = V_z^2 + \max\left\{0, 2m^*\beta^2(\mu + m^*\beta^2)\left[1 \pm \sqrt{1 - \tfrac{\mu^2 - V_z^2}{(\mu + m^*\beta^2)^2}}\right]\right\}. \tag{3.6}$$

3.2.2 Casimir effect results

We use a microscopic quantum field theoretic method to calculate the Casimir energy at zero temperature in terms of the current-current correlation functions of the two electron systems under consideration and virtual photons in the three-dimensional (3D) vacuum between them. Summing up the diagrams in Eq. (1.6), the Casimir energy at zero temperature for parallel 2D plates separated by a distance a is given by

$$\mathcal{E}_c(a) = \frac{1}{4\pi^2}\int_0^\infty dq_\perp\, q_\perp \int_0^{q_\perp} d\omega\ \mathrm{tr}\ln\left[\hat{\mathbf{1}} - \hat{\tilde{\Pi}}_A\hat{D}(a)\hat{\tilde{\Pi}}_B\hat{D}(a)\right], \tag{3.7}$$

where $\hat{D}(a) = \hat{D}(q_\perp, i\omega, a)$ is the photon propagator and $\hat{\tilde{\Pi}}_i = \hat{\tilde{\Pi}}_i(q_\perp, i\omega)$ is the current-current correlation function for plate i, dressed by interactions with 3D photons. We choose the gauge with no scalar potential, $\phi = 0$, so the relevant components of the photon propagator have the form

$$\hat{D}(q_\perp, i\omega, z) = \frac{\hbar}{2} \begin{pmatrix} \frac{q_\perp}{\omega^2} & 0 \\ 0 & \frac{1}{q_\perp} \end{pmatrix} e^{-q_\perp |z|}.$$

The dressed current-current correlation function can be expressed in terms of the bare correlation function, $\hat{\Pi}$, as

$$\hat{\tilde{\Pi}} = \left[\hat{\mathbf{1}} - \hat{\Pi}\hat{D}(z=0)\right]^{-1} \hat{\Pi},$$

which accounts for dynamical screening of photons in the random-phase approximation (RPA).

We take the derivative of Eq. (3.7) with respect to the plate separation, a, to obtain an expression for the Casimir force. We then integrate this expression numerically for fixed separation $a = 50\,\text{nm}$ and Fermi energy μ, while varying $|V_z|$, i.e., varying the magnetic field in an actual experiment. We consider two Fermi energies, $\mu = \pm 6$ and $\pm 10\,\text{meV}$, which give that the magnetic fields needed to reach the transition are $B_L = 2$ and $3.35\,\text{T}$. For all numerical results, we give the Casimir force in our considered system, F_c, normalized by the Casimir force between ideal conducting plates, $F_0 = -\hbar c\pi^2/240a^4$, calculated for the same plate separation. The dependence on plate separation closely follows the usual dependence for the Casimir force with the magnitude of the force increasing at shorter separations. Furthermore, the qualitative nature of the effect we find is not affected by the plate

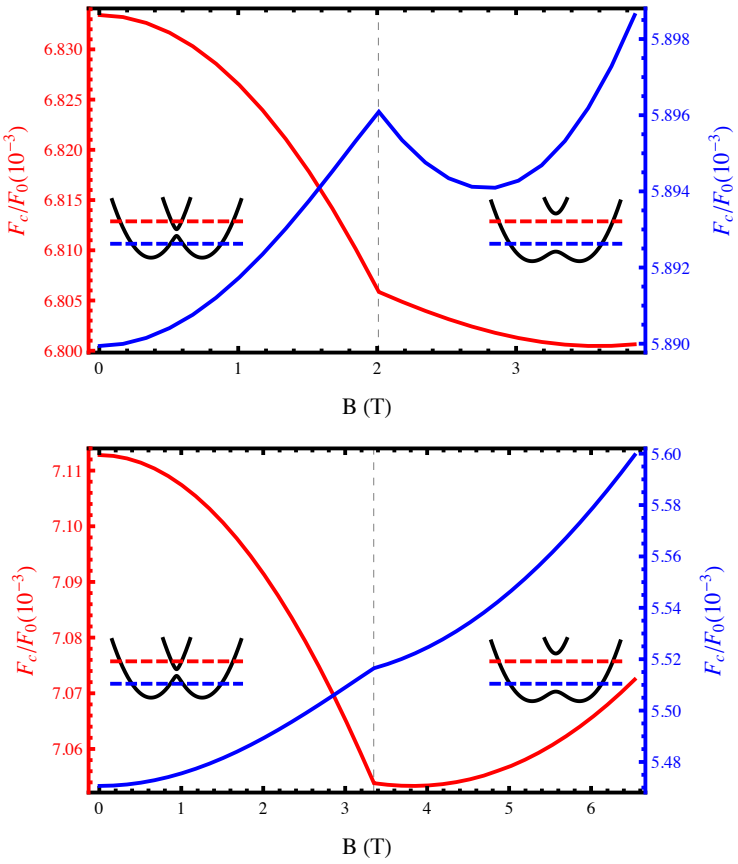

Figure 3.2: The Casimir force F_c normalized by the ideal conductor value between one semiconductor plate and one metallic plate separated by $a = 50\,\text{nm}$ as a function of applied magnetic field. The red plot (left axis) corresponds to $\mu > 0$, and the blue plot (right axis) corresponds to $\mu < 0$. The upper plot uses $\mu = \pm 6\,\text{meV}$ and the lower uses $\mu = \pm 10\,\text{meV}$. The insets show the band structure above and below the transition point (marked with a dashed line) along with the two fixed values of the Fermi energy.

separation.

For the simple system with *no* spin-orbit coupling ($\beta = 0$), i.e., two metallic plates, the Casimir force as a function of magnetic field is shown in Fig. 3.3. The magnetic fields needed to drive a Lifshitz transition in a typical system here is prohibitively large.

As the magnetic field is tuned and the chemical potential is kept fixed and positive, the Fermi surface changes by the removal of an electron pocket:

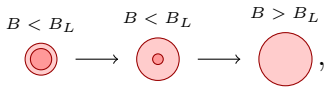

$$\mu > 0 \text{ fixed}, \tag{3.8}$$

where the shaded circles represent filled electron states in the 2D k-space. In Fig. 3.3, we see that for $B < B_L$ the Casimir force is constant with varying B, since the carrier density of the material, which in this case is the only free parameter determining the value of $\hat{\Pi} = -\frac{e^2}{h}\left[2\mu\,\Theta(\mu - |V_z|) + (\mu + |V_z|)\,\Theta(|V_z| - \mu)\right]$, is constant in this region. As the upper band is raised above the Fermi level, the closing of the upper band Fermi surface is indicated by a kink in the Casimir force, above which the magnitude of the force increases with B, consistent with the increase in the carrier density in this region. Unlike spin-orbit-coupled materials – the subject of this paper – this simple system has a critical field $B_L = \frac{|\mu|}{g\mu_B}$ which is unreasonably large (on the order of 10 000 T) due to large Fermi energies and small g factors. However, the spin-orbit-coupled semiconductors have small Fermi energies and large g factors, leading to a more reasonable value of B_L.

For the semiconductors under consideration, the Casimir force as a function of the magnetic field is presented in Fig. 3.2 for the case of one metallic plate and

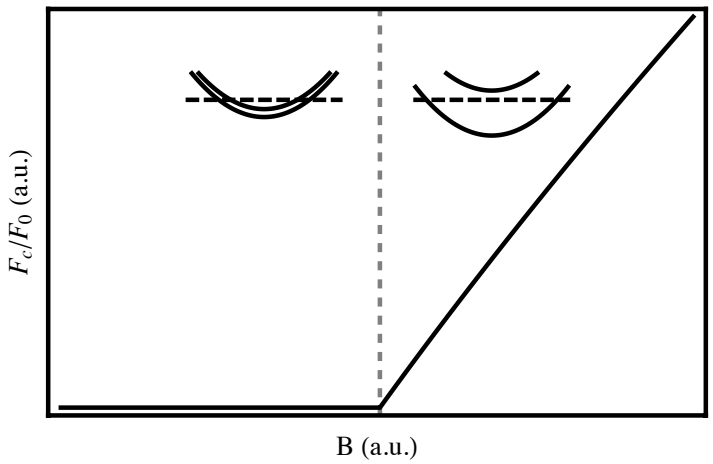

Figure 3.3: The Casimir force F_c normalized by the ideal conductor value between two metallic plates at a fixed separation as a function of the applied magnetic field. The insets show the band structure above and below the transition along with the fixed value of the Fermi energy. With a large Fermi energy and small electronic g factor (≈ 2), a prohibitively large magnetic field is needed to reach the transition.

one InSb plate and in Fig. 3.4 for the case of two InSb plates. Additionally, relevant numerical quantities (chemical potential, value of the force, change of force from the zero magnetic field value, and change of the slope characterizing the kink) associated with these plots are given in Tables 3.1 and 3.2. As the Zeeman energy changes, the value of the chemical potential has a strong influence on the behavior of the Casimir force. For positive values of μ (red curves), the Fermi surface sees behavior similar to that seen in Eq. (3.8). The behavior of the Casimir force above and below the transition is similar in both systems we consider, with the force decreasing in magnitude as the magnetic field strength is increased towards the transition and the force increasing above the transition for sufficiently large values of B. This increase at large B is irrespective of Fermi energy or case, and $V_z \gg \beta\sqrt{2m^*|\mu|}$, leading to a suppression of the spin-orbit-coupling term and a crossover to the simple metallic behavior.

For negative values of μ (blue curves), the InSb Fermi surface changes begins with a hole pocket that disappears at the critical magnetic field

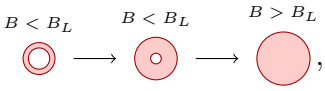

$$\mu < 0 \text{ fixed}, \tag{3.9}$$

where now the empty hole is the hole pocket. The behavior of the Casimir force is different in the two systems. When considering one InSb plate and one metallic plate, the force increases with increasing B below the Lifshitz transition for all values of μ considered and then increases above the transition as well for a sufficiently strong magnetic field (again, in a crossover to the simple metal case). In the system composed of two InSb plates, there is no common trend seen in the Casimir force

μ (meV)	$\frac{F_c(B_L)}{F_0}$	$\frac{F_c(B_L)-F_c(0)}{F_0}$	$\frac{dF_c}{dB}\|_{B=B_L^+} - \frac{dF_c}{dB}\|_{B=B_L^-}$ (F_0/T)
6	6.806	-0.02756	0.0212
10	7.054	-0.0589	0.0326
-6	5.896	0.0061	-0.0097
-10	5.516	0.0458	-0.0125

Table 3.1: Some important numerical results from the case of the Casimir force between one metallic plate and one InSb plate, all in units of $F_0 = -\hbar c\pi^2/240a^4 \times 10^{-3}$. The first column gives the value of the force at the transition. The second column gives the change in the force from $B = 0$ to the transition. The last column gives the jump in the derivative of the force with respect to the applied magnetic field across the transition, giving a measure of the severity of the kink.

μ (meV)	$\frac{F_c(B_L)}{F_0}$	$\frac{F_c(B_L)-F_c(0)}{F_0}$	$\frac{dF_c}{dB}\|_{B=B_L^+} - \frac{dF_c}{dB}\|_{B=B_L^-}$ (F_0/T)
6	5.138	-0.0291	0.0200
10	5.346	-0.0619	0.0310
-6	4.367	-0.0020	-0.0056
-10	4.041	0.0192	-0.0035

Table 3.2: The same as Table 3.1 but for the case of two identical InSb plates.

for the negative values of the Fermi energy we consider, except that, again, above a certain magnetic field strength the force increases with increasing B. For the lowest of the Fermi energies considered, we see that the Casimir force decreases with B below the transition and then even more quickly directly above the transition.

The main feature of all of these plots is the sharp kink seen at the Lifshitz transition point, and this feature should be discernible even considering the effects of temperature and a substrate. We expect the features to remain for temperatures much less than the energy of the gap at the transition point (i.e. the chemical potential): 70 K and 116 K for chemical potentials of 6 and 10 meV, respectively. Additionally, as long as the substrate for either the InSb or Au is a poor conductor, nonmagnetic, and does not experience an electronic transition in the range of magnetic fields needed to reach the Lifshitz transition, then we would expect it to have at most a small effect on our results, and not to change the nature of the features we find.

These features can be understood by examining the imaginary frequency AC conductivities of the InSb plates as a function of magnetic field at a fixed nonzero frequency; since the plates have no disorder there is no dissipation and the longitudinal DC conductivity is infinite. Both the longitudinal and Hall conductivities at finite frequency have a discontinuity in their derivatives with respect to B at the point where $|\mu| = V_z$, just as we find with the Casimir force. The overall trend in the longitudinal conductivity, shown in Fig. 3.5, mimics the behavior of the Casimir force we find for positive Fermi energies—decreasing in magnitude below the transition, then decreasing less drastically directly above the transition until reaching a

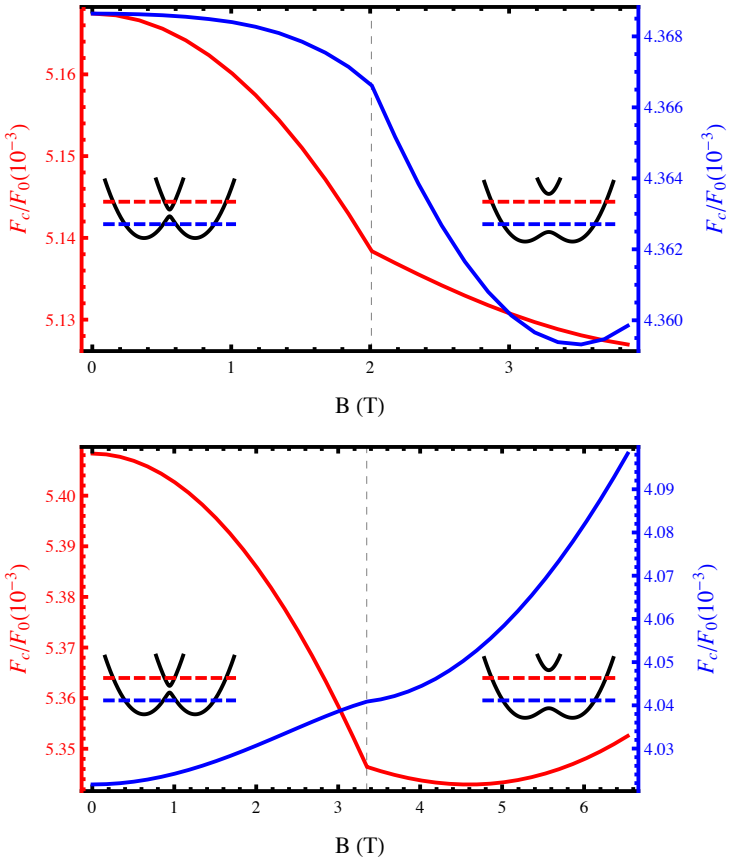

Figure 3.4: The Casimir force F_c normalized by the ideal conductor value F_0 between two semiconductor plates separated by $a = 50\,\text{nm}$ as a function of applied magnetic field. The red plot (left axis) corresponds to $\mu > 0$, and the blue plot (right axis) corresponds to $\mu < 0$. The upper plot uses $\mu = \pm 6\,\text{meV}$ and the lower plot uses $\mu = \pm 10\,\text{meV}$. The insets show the band structure above and below the transition point along with the two fixed values of the Fermi energy.

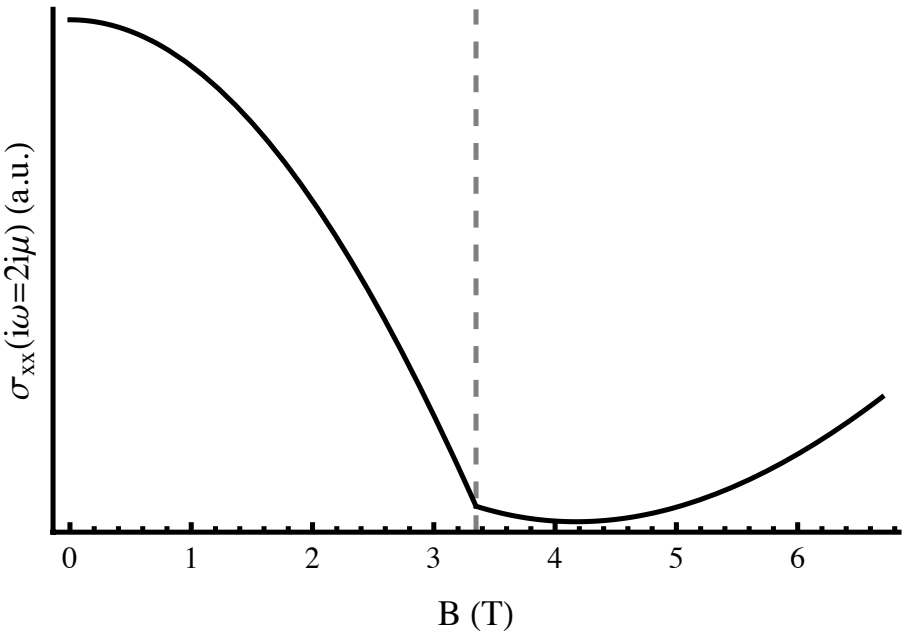

Figure 3.5: The imaginary frequency longitudinal conductivity of the InSb plate at $i\omega = 2i\mu$ for $\mu = 10\,\text{meV}$ as a function of the applied magnetic field. The Lifshitz transition point is indicated with a dashed line.

minimum and increasing with B. All of these results taken together suggest that the Hall contribution to the Casimir effect from interband spin-orbit interactions, which are stronger when the bands are closer in energy (i.e., small V_z), works to suppress the strength of the Casimir force. Since the Lifshitz transition occurs precisely when $V_z = |\mu|$, for smaller values of the Fermi energy the transition occurs for smaller values of V_z, meaning that the bands are not so far removed from each other and interband effects are stronger. Additionally, these effects are stronger in the system with two InSb plates, as would be expected if they were the result of spin-orbit coupling.

3.3 Quantum Interference phenomenon in the Casimir effect

In this section, we provide a new way to experimentally test the validity of the diffusive electron model by tuning an external magnetic field (or temperature from a less practical standpoint) in a Casimir system with a two-dimensional plate. The proposed experiment would be the typical experiment seen in Fig. 3.6 where the plate would be quasi-two-dimensional. We find a dramatic change in the Casimir effect between Drude model plates due to weak localization, shown in Fig. 3.7, that is just not seen with the plasma model.

Additionally, we test if particular disorder realizations can have a strong impact on our model. The theory behind the use of a diffusive models relies upon performing an average over all possible realization of a disorder potential in the material. However, if this disorder average is done at the level of linear response instead of on the Casimir energy itself, then all effects from, e.g., the nonuniform nature of physical disorder realizations are neglected. While exact calculation of these neglected effects is prohibitively difficult, it is possible to estimate whether ignoring them gives a valid approximation to the Casimir energy.

A fundamental assumption of the WL effect is that electronic motion is diffusive in nature, and its contribution to conductivity is calculated as a correction to the Drude model. Therefore, any impact found on the nature of the Casimir effect due to WL would apply only to a diffusive model of metallic plates and not a ballistic model; a sensitive experimental test of the effects of WL on the Casimir effect would provide a clear indication of whether a diffusive picture of electronic

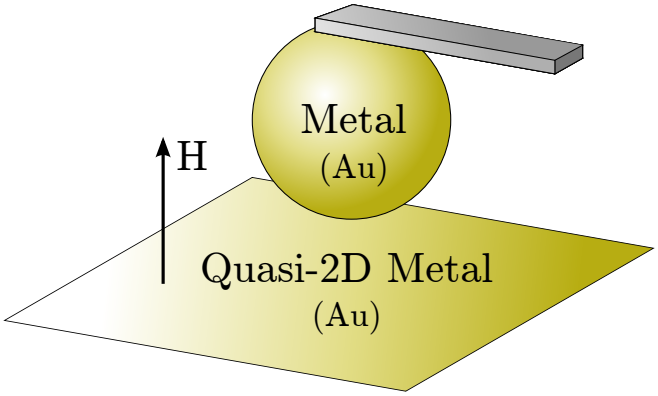

Figure 3.6: The geometry typically used in experimental measurements of the Casimir force is a gold coated sphere above a planar plate. Here we show the sphere suspended from a cantilever. We consider a lower plate of very thin metal with a weak applied perpendicular magnetic field.

motion correctly describes the physics of the electrons in the experiment.

3.3.1 Casimir effect results

The basic inputs into Eq. (3.10) are the electromagnetic linear response functions for the two plates under consideration which contain all the electromagnetic properties necessary for a calculation of the Casimir effect. These are in Eqs. (1.15) and (1.16) in Sec. 1.4.2.

To explore the effects of WL on the Casimir effect, we consider a system consisting of two flat parallel plates: one thick plate described by the Drude model and one two-dimensional plate described by the Drude model with an additional term giving the weak localization effect. With an experimental setup in the typical plate-sphere geometry, as shown in Fig. 3.6, the gold layer on the sphere is thick

enough to be most accurately described as a three dimensional material. Since the effect of weak localization in 3D materials is much weaker than in 2D films, we only consider the WL effect in the 2D plate. In addition to this system of primary interest, we also consider the Casimir pressure between two plasma plates and between two Drude plates without weak localization for points of comparison. The latter of these will also give the expected behavior of the system including the 2D plate with WL correction at sufficiently high magnetic fields to completely suppress the WL effect ($H \gtrsim 100\,\text{gauss}$). In these cases we consider the same geometry, with one thick semi-infinite plate and a parallel 2D plate. For a calculation of the Casimir pressure in these systems we start from the well-known Lifshitz equation for the Casimir energy density at finite temperature [40] without mixing of polarizations upon reflection,

$$\mathcal{E}_c(a) = k_B T \sum_{\{\omega_n\}}{}' \int \frac{d^2q}{(2\pi)^2} \left[\ln\left(1 - r_{\text{TM}}^{(1)} r_{\text{TM}}^{(2)} e^{-2\sqrt{q^2+\omega_n^2}a}\right) + \ln\left(1 - r_{\text{TE}}^{(1)} r_{\text{TE}}^{(2)} e^{-2\sqrt{q^2+\omega_n^2}a}\right)\right]. \quad (3.10)$$

In this expression, $\sum'$ denotes a sum over positive Matsubara frequencies, counting the $n = 0$ term with half weight. The functions $r_{\text{TM}}^{(i)}$ and $r_{\text{TE}}^{(i)}$ are the reflection coefficients of plate i for the two polarizations of light. The subscript TM refers to the polarization where the magnetic field is perpendicular to the plane of incidence, and similarly for TE with the electric field. The reflection coefficients depend on both q and the Matsubara frequency $\omega_n = 2\pi n k_B T$, and may also depend on the other parameters of the system under consideration, such as the applied magnetic field H and additional temperature dependence. The reflection coefficients can be written explicitly in terms of the dielectric functions of the plates, $\epsilon_i(i\omega_n)$, or alternatively in

terms of the electromagnetic linear response functions of the plates, $\Pi_i(i\omega_n)$, which are related to the dielectric functions as

$$\epsilon(i\omega_n) = \begin{cases} 1 - \Pi^{2D}(i\omega_n)\delta(z)/\omega_n^2 & \text{for 2D systems} \\ 1 - \Pi(i\omega_n)/\omega_n^2 & \text{for 3D systems.} \end{cases} \tag{3.11}$$

The reflection coefficients have the form

$$\begin{aligned} r_{\mathrm{TM}}^{2D}(q, i\omega_n) &= \frac{\Pi^{2D}(i\omega_n)}{\Pi^{2D}(i\omega_n) - \frac{2\omega_n^2}{q_\perp}} \\ r_{\mathrm{TE}}^{2D}(q, i\omega_n) &= \frac{\Pi^{2D}(i\omega_n)}{\Pi^{2D}(i\omega_n) - 2q_\perp} \end{aligned} \tag{3.12}$$

for two-dimensional plates, where we have defined $q_\perp = \sqrt{q^2 + \omega_n^2}$. For very thick three-dimensional metallic plates (thickness $d \to \infty$), the reflection coefficients have the form

$$\begin{aligned} r_{\mathrm{TM}}^{3D}(q, i\omega_n) &= -\frac{\sqrt{q_\perp^2 - \Pi(i\omega_n)} - q_\perp + \frac{q_\perp}{\omega_n^2}\Pi(i\omega_n)}{\sqrt{q_\perp^2 - \Pi(i\omega_n)} + q_\perp - \frac{q_\perp}{\omega_n^2}\Pi(i\omega_n)} \\ r_{\mathrm{TE}}^{3D}(q, i\omega_n) &= -\frac{\sqrt{q_\perp^2 - \Pi(i\omega_n)} - q_\perp}{\sqrt{q_\perp^2 - \Pi(i\omega_n)} + q_\perp}. \end{aligned} \tag{3.13}$$

The Casimir pressure is found from Eq. (3.10) by taking its derivative with respect to plate separation, a.

We consider three systems of one thick plate and one 2D plate: both plasma plates, both Drude plates, and most importantly, a thick Drude plate with a 2D Drude plate including the weak localization correction term given in Eq. (1.16). In all of these systems, we fix the plate separation at $a = 250\,\mathrm{nm}$ and calculate the Casimir pressure as a function of either an externally applied magnetic field or temperature, staying in the low temperature regime where Eq. (1.17) is valid. Additionally, we set the elastic mean free path of the electrons in disordered plates to be $l = 15\,\mathrm{nm}$ and the Fermi energy and effective electron mass to be those of

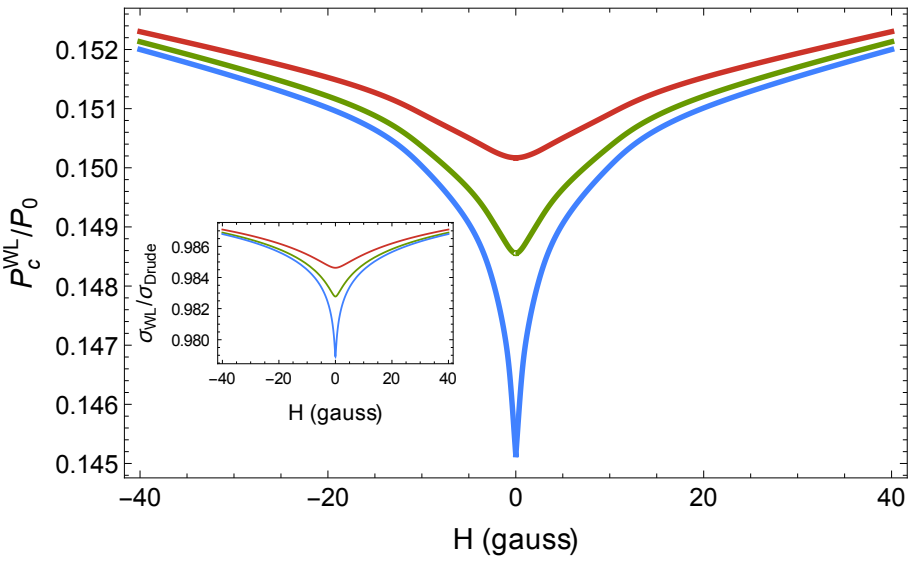

Figure 3.7: The dependence of the Casimir pressure on the applied magnetic field between two disordered plates (one 3D and one 2D) at a separation of $a = 250\,\text{nm}$. The 2D plate is described by the Drude model with the weak localization correction. The force is normalized by the ideal conductor result and is plotted for three temperatures–3, 1, and 0.1 K, from top to bottom. The Casimir pressure is normalized by the ideal result, $P_0 = -\frac{\hbar c \pi^2}{240 a^4}$. The inset shows the conductivity of the 2D plate with WL correction as a function of the applied magnetic field, normalized by the uncorrected Drude conductivity, at the same three temperatures.

gold: $\epsilon_F = 5.53\,\text{eV}$ and $m^* = 1.10m_0$ where m_0 is the free electron mass [187]. We normalize all Casimir pressures by the ideal conductor result, $P_0 = -\frac{\hbar c \pi^2}{240 a^4}$, with $a = 250\,\text{nm}$.

In addition to the disagreement on the magnitude of the effect between Drude and plasma models, we find that there is qualitatively different behavior when accounting for the effect of weak localization. The Casimir pressure between plasma plates has no dependence on the strength of the applied magnetic field, at least for such weak fields as we consider here, and only a very weak dependence on temperature in this low temperature regime—the change of the normalized pressure from 10 K to 0.1 K is a decrease of 1.7×10^{-4}. In stark contrast, the Casimir pressure when considering a Drude plate with WL effects shows both a highly nontrivial dependence on even a weak applied magnetic field (at low temperatures), shown in Fig. 3.7, and also a sharp decrease with decreasing temperature (with no applied magnetic field), shown in Fig. 3.8. Both the temperature and magnetic field effects are expected when considering the Casimir pressure as a function of the conductivity of the plates. The sharp drop in the Casimir pressure with decreasing temperatures matches the drop in conductivity of the 2D plate obtained from theory, shown in the inset of Fig. 3.8, and the strong dependence of the Casimir pressure on a weak magnetic field closely follows the dependence of the conductivity of the 2D plate as obtained from theory, shown in the inset of Fig. 3.7, and seen in magnetoresistance experiments with 2D thin films [133, 134]. Indeed, we find that applying a magnetic field of only $H = 40\,\text{gauss}$ perpendicular to the plates is enough to reduce the suppression of the pressure by approximately 40%.

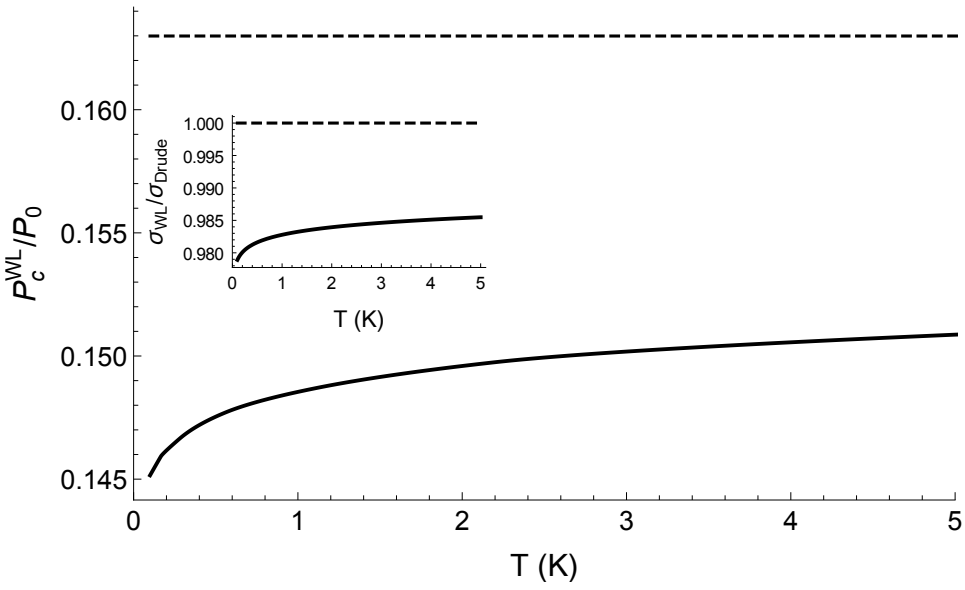

Figure 3.8: The dependence of the Casimir pressure on temperature between two Drude model plates (one 3D and one 2D) at a separation of $a = 250\,\text{nm}$. The force is normalized by the ideal conductor result, and there is no applied magnetic field. The solid line is obtained from including the WL correction in the 2D plate, and the dashed line is the result obtained if the effect of WL is ignored. The inset shows the dependence of the conductivity of the 2D plate as a function of temperature normalized by the uncorrected Drude model conductivity. The solid curve is obtained from the Drude model with WL correction and the dashed line at 1 is for comparison to the uncorrected Drude model.

At $T = 0.1\,\mathrm{K}$ and $H = 0\,\mathrm{gauss}$ we find that by correctly accounting for the effect of WL in the 2D plate the Casimir pressure is 11% less than if the 2D plate were described by a simple Drude model without the WL correction. At this temperature and magnetic field, the change in the Casimir pressure from including the WL correction is larger in magnitude than the difference in the Casimir pressures predicted by the plasma model and naive Drude model, i.e.,

$$\frac{P_c^{\mathrm{Drude}} - P_c^{\mathrm{WL}}}{P_c^{\mathrm{plasma}} - P_c^{\mathrm{Drude}}} = 1.14 \text{ for } T = 0.1\,\mathrm{K}, \tag{3.14}$$

so the effect is large enough to be measurable for a low enough temperature.

There are several ways to increase the size of the effect even beyond this, the most straightforward being to lower the temperature even further. We also find that the effect can be increased by decreasing the electron mean free path, l, equivalent to increasing the impurity concentration, which can be seen by examining the dependence of Eq. (1.16) on the mean free path, given partially through the dephasing time in Eq. (1.17). When considering smaller values of l, however, one must be sure that the impurity concentration is still below the limit of complete Anderson localization, or else this model of diffusion breaks down. Alternatively, when considering much larger values of l, which would make the effect smaller, one must be sure that the mean free path is much smaller than the sample dimension L or else the model of a disordered system breaks down. In an actual experimental system neither of these issues is likely to arise.

Since a controlled smooth variation of temperature in Casimir effect experiments is almost an impossibility, especially at low temperatures where vibrational

noise is difficult to remove due to the boiling of cryogenic liquids [188], an experimental test of the effects of weak localization on the Casimir effect could more easily be performed at fixed low temperature with varying magnetic field, looking for the effect shown in Fig. 3.7. Only weak magnetic fields would be necessary for such an experiment, as applying a magnetic field as weak as tens of gauss perpendicular to the plates would be enough to reduce the effect by a significant percentage. We propose that an experimental test of these effects could be performed in the normal plate-sphere geometry with a very thin metallic film at a fixed separation, at a fixed low temperature, and with a varying weak magnetic field. While the exact numerical values the forces measured in this geometry are almost guaranteed to differ from the results we find, the general trends in the temperature and magnetic field dependence of the force are expected to remain.

3.3.2 Mesoscopic disorder fluctuations

When considering disordered systems one must determine when to perform averaging over disorder potential realizations. Different realizations of the disorder potential will give different Casimir energies, and local fluctuations in the disorder away from this average will cause certain patches on each plate to vary in how attractive they are–very similar to the phenomenon of universal conductance fluctuations (UCF) [189, 190]—leading to a self-averaging of the Casimir energy between two macroscopic plates. This argument would imply that instead of carrying out the averaging procedure on the linear response Π, which gives the Lifshitz formula with

the Drude model, we should perform averaging over the entire Casimir energy itself. In practice, however, it is not possible to consider an exact disorder potential or to perform the averaging procedure over the entire Lifshitz formula, and it is unknown if the simplification of using the disorder averaged linear response (i.e. the Drude model) in the Lifshitz formula is still a legitimate approximation.Another way of phrasing this issue is that the approximation

$$\langle \mathcal{E}_c[\Pi] \rangle = \mathcal{E}_c[\langle \Pi \rangle] + \delta \mathcal{E}_c \approx \mathcal{E}_c[\langle \Pi \rangle] \tag{3.15}$$

leads to a naive violation of the Nernst theorem [191, 192] (though this seems to actually be an order of limits issue that has since been resolved [193]), but it is unclear if it nonetheless closely approximates the exact expression for the Casimir energy one would obtain if disorder were to be treated exactly or if averaging were done at the appropriate stage of the calculation.

Here we calculate what effect fluctuations from the average in any particular realization of a disorder potential have on the Casimir energy at low temperature, where conductance fluctuations are strongest. We start from a microscopic version of the Lifshitz formula in position space directly written down from Eq. (1.7),

$$\mathcal{E}_c \left[\Pi_1, \Pi_2\right] = k_B T \sum_{\{\omega_n\}}{}' \operatorname{Tr} \ln \left(1 - M\right), \tag{3.16}$$

where

$$M = \int dr_1 dr_2 dr_3 \hat{\tilde{\Pi}}_1(r, r_1) \hat{D}(r_1, r_2) \hat{\tilde{\Pi}}_2(r_2, r_3') \hat{D}(r_3, r').$$

Here, $\hat{D}$ is the photon propagator, which in M connect the screened response of one plate to the other, and $\hat{\tilde{\Pi}}_i$ is the RPA screened electromagnetic linear response

functions for plate i, schematically given by $(\hat{\mathbf{1}} - \hat{\Pi}_i \hat{D}(0))^{-1}\hat{\Pi}_i$, where $\hat{\Pi}$ is the unscreened linear response function and $\hat{D}(0)$ is the photon propagator along the plate. From this point on we will consider plate 1 to be disordered with a particular disorder realization and for simplicity we will assume that plate 2 is homogeneous and not disordered. We will further take both plates to be two-dimensional. For two-dimensional plates, the linear response function and photon propagator are 2×2 matrices, with the components of Π being proportional to the AC conductivity of the plates.

We are interested in the case of metallic plates without a Hall effect so both response functions are proportional to the identity matrix. The photon propagator is diagonal as well. The matrix trace in Eq. (3.16) becomes trivial, leaving us with a sum over photon polarizations. We make the further approximation that the Casimir energy is well described by just the first term obtained from expanding the logarithm,

$$\mathcal{E}_c\left[\Pi_1, \Pi_2\right] \approx -k_B T {\sum_{\{\omega_n\}}}' \int \prod_{i=1}^{4} dr_i \sum_{X=TE,TM} \widetilde{\Pi}_1^X(r_4, r_1) D^X(r_1, r_2) \widetilde{\Pi}_2^X(r_2, r_3) D^X(r_3, r_4), \tag{3.17}$$

where now we label the two photon polarization with the superscript X. Diagrammatically, this approximation can be represented as in Fig. 3.9.

To ensure the following procedures are analytically tractable, we must make one further simplifying approximation. We assume that the response function for plate 1, Π_1, which depends on an exact disorder realization, can be written as $\Pi_1 = \langle \Pi_1 \rangle + \delta\Pi_1$, i.e. the exact response function can be written as the disorder

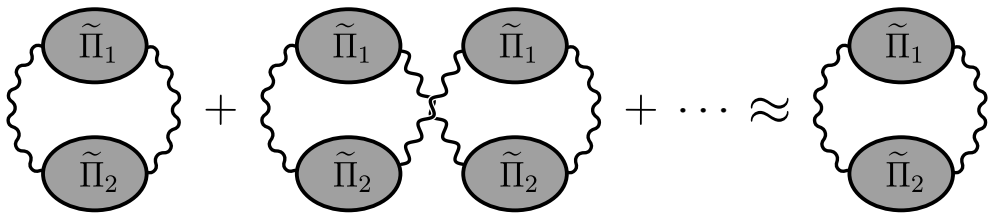

Figure 3.9: The lowest order approximation to the Casimir energy given in Eq. (3.17). The grey ovals represent the RPA screened linear response functions, and the wavy lines represent photon propagators.

averaged (Drude) response plus another small term to account for the particular disorder realization, here called $\delta\Pi_1$. (Note that this $\delta\Pi_1$ is distinct from the function of similar name given in Eq. (3.3) and Eq. (1.16) which define a correction to the correlation function obtained after disorder averaging.) With this notation, we now expand the RPA on plate 1 to first order in $\delta\Pi_1$ as,

$$\widetilde{\Pi}_1 \approx \underbrace{\frac{\langle\Pi_1\rangle}{1-\langle\Pi_1\rangle\, D}}_{=\widetilde{\Pi}_1^D} + \left[\frac{1}{1-\langle\Pi_1\rangle\, D} + \frac{\langle\Pi_1\rangle\, D}{\left(1-\langle\Pi_1\rangle\, D\right)^2}\right]\delta\Pi_1 \tag{3.18}$$

$$\approx \widetilde{\Pi}_1^D + \underbrace{\frac{1}{1-\langle\Pi_1\rangle\, D(0)}\left(1+\widetilde{\Pi}_1^D D(0)\right)}_{=\Gamma_1}\delta\Pi_1. \tag{3.19}$$

This is the form of $\widetilde{\Pi}_1$ that is used in Eq. (3.17).

We now look to the probability distribution of the Casimir energy due to fluctuations in the disorder realization in plate 1, now contained entirely within the

function $\delta\Pi_1$, which is given by

$$\begin{aligned}\mathcal{P}_{\mathcal{E}_c}[\mathcal{E}] &= \langle \delta(\mathcal{E}_c - \mathcal{E})\rangle \\ &= \int \mathcal{D}(\delta\Pi_1) \int \frac{dx}{2\pi} e^{ix(\mathcal{E}_c-\mathcal{E})} \times \\ \times \exp&\left[-\frac{1}{2}\int \prod_{i=1}^{4} dr_i \delta\Pi_1(r_1,r_2) K_1(r_1,\cdots,r_4)\delta\Pi_1(r_3,r_4)\right].\end{aligned} \tag{3.20}$$

This expression makes use of the disorder averaged correlator of two unaveraged response functions for the disordered plate, which can be written as,

$$K_1^{-1}(r_1,r_2,r_3,r_4) = \langle \delta\Pi_1(r_1,r_2)\delta\Pi_1(r_3,r_4)\rangle\,, \tag{3.21}$$

and is also given diagrammatically in Fig. 3.10. The function K_1^{-1} is very similar to the central object of interest considered in the context of UCF [189, 190, 194], and it is calculated in the same manner. It is related to the size of the fluctuations of the conductivity, $\delta\sigma^2$, (or equivalently in 2D, the conductance) in a similar way to how the linear response function Π is related to the conductivity. The only difference between the calculation of this function here and in the context of UCF is that the latter is primarily concerned with conduction of electrons through a system with attached leads, usually at zero temperature, while we consider a system with no leads at finite temperature. As such, most of the qualitative properties of conductance fluctuations apply in our analysis of fluctuations in the Casimir energy as well, though the exact form of K_1^{-1} differs by small numerical factors. With this insight, we can already draw several conclusions about the nature of the distribution we will obtain from Eq. (3.20). Most importantly, for weak disorder we can expect fluctuations of the Casimir energy around the average value to be

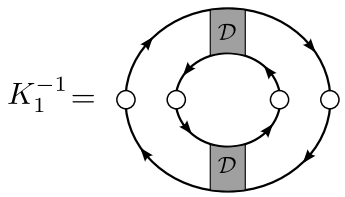

Figure 3.10: The primary diagram giving the correlation of disorder fluctuations, as defined in Eq. (3.21). The components of the diagrams have the same meanings as given in Fig. 1.1. Diagrams containing more diffusons are found either not to contribute to the correlator or are found to have a contribution $\mathcal{O}(1/\epsilon_F\tau)$ smaller.

small since conductance fluctuations are small in good metals: $\delta\sigma^2/\sigma^2 \sim 1/(\epsilon_F\tau)^2$. Additionally, we could expect the size of the fluctuations to be reduced by a factor of 2 if a magnetic field were applied to the sample. This is because the diagram for K_1^{-1} given in Fig. 3.10 gives the same contribution at zero magnetic field if all diffusons are replaced with cooperons, but the cooperon contribution is suppressed in magnetic fields in the same way as the weak localization correction to the conductivity.

In order to evaluate Eq. (3.20), we perform a saddle point approximation on the functional integral over the disorder fluctuation, $\delta\Pi_1$, which after a straightforward calculation gives,

$$\mathcal{P}_{\mathcal{E}_c}[\mathcal{E}] = \frac{1}{\sqrt{2\pi W^2}} \exp\left[-\frac{(\mathcal{E} - \mathcal{E}_0^{\text{Drude}})^2}{2W^2}\right], \tag{3.22}$$

where we have defined the quantities $\mathcal{E}_0^{\text{Drude}}$, the average, and W, the width of the energy distribution. We find that the average energy is given by the same expression as in Eq. (3.17), but with the substitution $\widetilde{\Pi}_1 \to \widetilde{\Pi}_1^{\text{D}}$, i.e. replacing the exact unaveraged response function Π_1 with the disorder averaged (Drude) response. Therefore, the average $\mathcal{E}_0^{\text{Drude}}$ is simply an approximation of the exact Drude result.

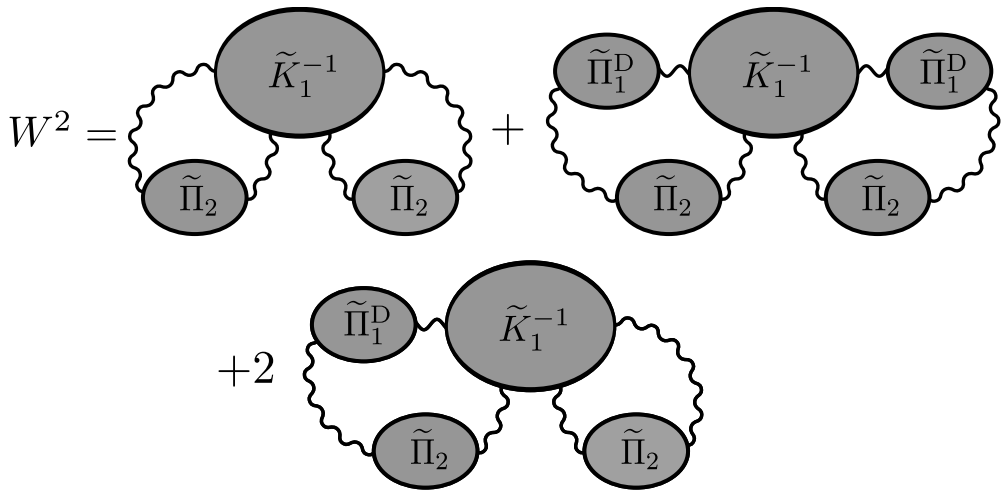

Figure 3.11: The diagrams giving the width of the distribution, explicitly given in Eq. (3.23).

Additionally, we find that the square of the width of the distribution can be written explicitly as,

$$W^2 = (k_B T)^2 {\sum_{\{\omega_n, \omega_{n'}\}}}' \int \prod_{i=1}^{4} dr_i dr_i' \sum_{X,Y} D^X(r_1, r_2) \widetilde{\Pi}_2^X(r_2, r_3) D^X(r_3, r_4) \times$$
$$\times D^Y(r_1', r_2') \widetilde{\Pi}_2^Y(r_2', r_3') D^Y(r_3', r_4') \Gamma_1^X \Gamma_1^Y K_1^{-1}(r_1, r_4, r_1' r_4'), \quad (3.23)$$

which can be represented diagrammatically as in Fig. 3.11. The multiple diagrams in this figure result from an expansion of the Γ_1 factors of Eq. (3.23),

$$\Gamma_1^X \Gamma_1^Y K_1^{-1} = \frac{\left(1 + \widetilde{\Pi}_1^{\mathrm{D}} D^X(0)\right)\left(1 + \widetilde{\Pi}_1^{\mathrm{D}} D^Y(0)\right) K_1^{-1}}{\left(1 - \langle \Pi_1 \rangle D^X(0)\right)\left(1 - \langle \Pi_1 \rangle D^Y(0)\right)}$$
$$\equiv \left(1 + \widetilde{\Pi}_1^{\mathrm{D}} D^X(0)\right)\left(1 + \widetilde{\Pi}_1^{\mathrm{D}} D^Y(0)\right) \widetilde{K}_1^{-1}.$$

We compute these expressions numerically in the same way that we calculate the Casimir pressure in Sec. 3.3.1. For both plates we use the Fermi energy and electron mass of gold, and we consider plate 1 to be disordered while plate 2 is a

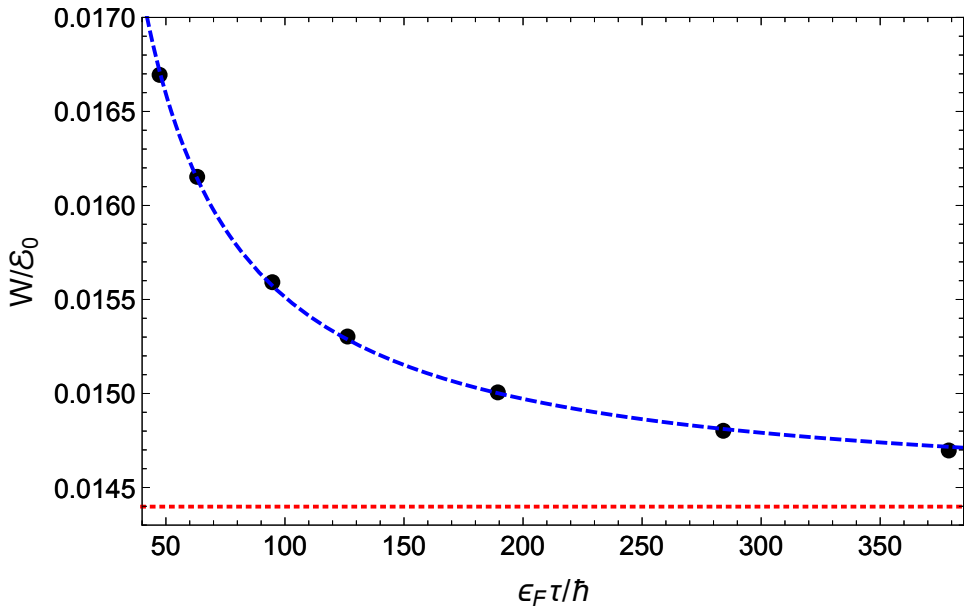

Figure 3.12: The fit of numerical data for the quantity $W/\mathcal{E}_0^{\text{Drude}}$ to the expected functional dependence given in Eq. (3.24). The black dots are the numerical data, the dashed blue line is the fit function, and the dotted red line is the asymptotic value $W/\mathcal{E}_0^{\text{plasma}}$, which has no dependence on τ in the leading approximation.

clean plasma plate. We use the material parameters for gold in plate 2 so that in the limit of weakening disorder we are left with identical plasma plates. We vary the parameter τ to determine the dependence of W and E_0, and the numerical results for their ratio are fit to the expected functional dependence, as shown in Fig. 3.12. In the parameter range we are interested in, we find the result,

$$\frac{W}{\mathcal{E}_0^{\text{Drude}}} \approx \frac{W}{\mathcal{E}_c^{\text{plasma}}} + C_1 \frac{\hbar}{\epsilon_F \tau}. \tag{3.24}$$

In this expression $C_1 \approx 0.096$ is a distance independent constant and $\mathcal{E}_0^{\text{plasma}}$ is the Casimir energy between two clean plasma model plates calculated in the same approximation as $\mathcal{E}_0^{\text{Drude}}$, given in Eq. (3.17). In the same way, we also find this

ratio's dependence on the distance between the plates. It suffices to consider only the first term for this purpose, since the second term in Eq. (3.24) has no dependence on a. We find,

$$\frac{W}{\mathcal{E}_c^{\text{plasma}}} \approx C_2 \sqrt{\frac{\hbar c}{\epsilon_F a}}, \tag{3.25}$$

where $C_2 \approx 0.038$ is another constant independent of both τ and a. The form of the disorder dependence in Eq. (3.24) is expected since a weakening of disorder, interpreted as an increase of the scattering time τ, will make a disordered plate more like a plasma plate. Therefore, a very large scattering time should give a very good approximation to the plasma result. Note, however, that the complete removal of disorder through the limit $\tau \to \infty$ has no physical meaning at this point in the calculation, since W has already necessarily been calculated in the presence of disorder. We can see from these two expressions that the distribution will be relatively sharply peaked, in the sense that $W/\mathcal{E}_0^{\text{Drude}} \ll 1$, for plates that are not too close together and are in the disorder regime $1/\epsilon_F \tau \ll 1$, as we have considered thus far.

We can get a better understanding of how peaked the energy distribution is around its average value by comparing its width W to a smaller relevant energy scale, $\mathcal{E}_0^{\text{Drude}} - \mathcal{E}_0^{\text{plasma}}$, by combining Eq. (3.24) and Eq. (3.25). We obtain,

$$\frac{W}{|\mathcal{E}_0^{\text{Drude}} - \mathcal{E}_0^{\text{plasma}}|} \approx C_2 \left(\sqrt{\frac{\hbar c}{\epsilon_F a}} + \frac{C_2}{C_1} \frac{c\tau}{a} \right). \tag{3.26}$$

We see that the nature of the energy distribution Eq. (3.22) depends on the two dimensionless quantities $\hbar c/(\epsilon_F a)$ and $c\tau/a$. Both of these dependencies can be understood intuitively. The dependence on $\hbar c/(\epsilon_F a)$ can be understood as arising

from the relevant photonic energy scale. The most important photons are those with wavelength equal to twice the distance between the plates, and when this distance is large, these long wavelength photons are able to average over larger areas of the plates, reducing the effect of local fluctuations. The dependence on $c\tau/a$ is similarly straightforward. It is a comparison of two time scales: the impurity scattering time, τ, and the time for photons to traverse the distance between the plates, a/c. When the ratio is small, electrons will have many impurity scattering events before interacting with a photon, so any effects due to impurities will be very important.

There are several regimes we can now explore. Here, we will always consider plates of the same material, so the Fermi energy is a fixed parameter and we can only vary a and τ. First, if the plates are very close, meaning $\hbar c/(\epsilon_F a)$ is large, then the distribution is very wide regardless of the size of τ. Second, if τ is large compared to a/c, meaning that photons interact with any given electron many times between impurity scattering events, then the distribution is again very wide, regardless of the size of $\hbar c/(\epsilon_F a)$. The only regime in which the distribution is very sharply peaked is when both dimensionless parameters are small. This requires that the plates are much farther apart than both length scales $\hbar c/\epsilon_F$ and $c\tau$, so that each electron undergoes many impurity scattering events between photon interactions and effect of disorder is more pronounced, but also so that long wavelength photons are most important, averaging out the disorder fluctuations.

Ultimately, this result means that for a given level of disorder, we can always go to large enough plate separations so that relatively small local fluctuations in the disorder potential of metallic plates are not likely to greatly affect the Casimir

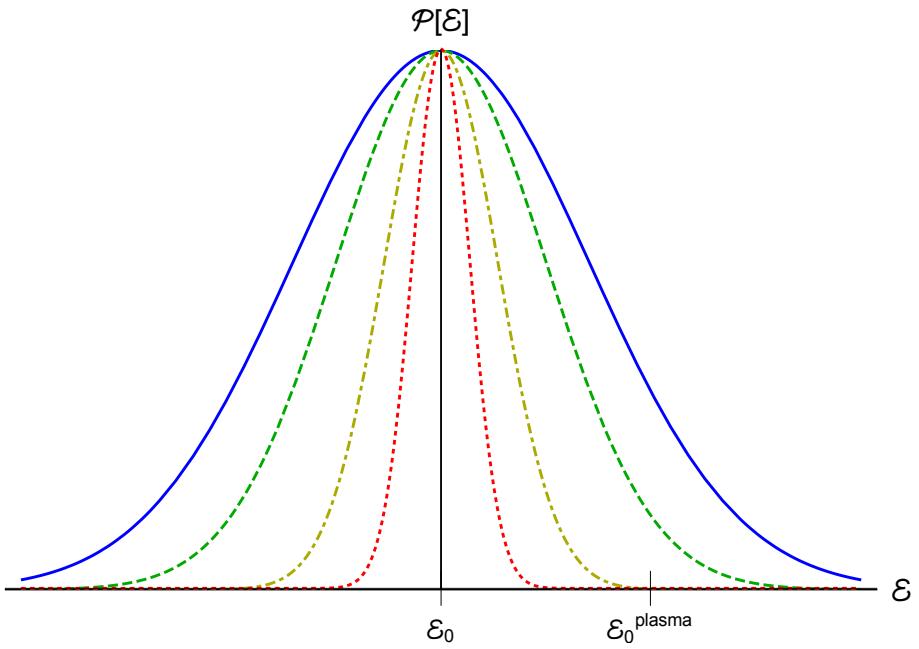

Figure 3.13: A plot of the distribution Eq. (3.22) given for several values of a for a constant value of $\tau = 4.5 \times 10^{-14}\,\text{s}$, corresponding to $l = 60\,\text{nm}$. The values of a are 250 (solid blue), 400 (dashed green), 800 (dash-dotted yellow), and 1600 nm (dotted red). The average $\mathcal{E}_0^{\text{Drude}}$ and width W are calculated numerically using Eq. (3.17) and Eq. (3.23). The plots are scaled so the distributions are all the same height, and so $|\mathcal{E}_0^{\text{Drude}} - \mathcal{E}_0^{\text{plasma}}|$ is always the same width. Also indicated is the value of $\mathcal{E}_0^{\text{plasma}}$. One sees that as a is increased the distribution becomes sharply peaked even compared to the small energy scale set by the difference from the plasma model.

energy, as shown in Fig. 3.13. The difficulty here is that for large values of the inelastic scattering time τ, the distance at which the distribution becomes very sharply peaked may be so large that the Casimir effect itself will become unmeasurably small. We note that the values of the parameters τ and a used to get the results in Sec. 3.3.1 give a distribution very sharply peaked around its average, so we are justified in our use of the Drude model despite any of the stated concerns over the disorder averaging procedure.

3.4 Conclusions

As we have shown in the first part of this chapter, tuning through a Lifshitz transition in this material causes a kink in the Casimir force while the microscopics control the nature and severity of the kink. We expect similar features to be found in other materials with such transitions – particularly due to the change in the carrier concentration across such a transition. This is one way in which precision Casimir force experiments could be used as a probe of nontrivial electronic properties or transitions. This is not exclusive to the particular semiconductor considered here; not only could the Casimir effect be used to probe Lifshitz transitions in other materials, but it could conceivably be used to detect other phenomena such as the Fermi surface reconstruction and the superconducting transition in cuprates and disorder-driven phenomena such as localization.

In the second part of this chapter, we showed that the weak localization correction to the Drude model at low temperatures may give the Casimir pressure

a nontrivial dependence on both temperature and applied perpendicular magnetic field. Moreover, we find that, for low enough temperatures, WL effects changes the Casimir pressure from the expected value without WL by an amount greater than the difference between the Drude and plasma model predictions. Since these effects are not applicable in a model of a 2D plate without disorder, i.e. the plasma model, a high precision experimental test measuring this temperature or magnetic field dependence would give a definitive indication of whether a diffusive model truly describes the behavior of electrons in Casimir experiments.

Lastly, we explored the effect that fluctuations in the disorder potential can have on the Casimir energy and the validity of using the Drude model considering that the correct averaging procedure would give a result that differs from the Drude model by the inclusion of nonlocal disorder fluctuation contributions. We find that for a given level of disorder, one can always overcome the effects of fluctuations by holding the plates far enough apart, which justifies the use of the Drude model theoretically.

Chapter 4: The repulsive Casimir effect between Weyl semimetals

4.1 Overview

In this chapter, we calculate the Casimir effect in a topological material not considered before with the Casimir force: Weyl semimetals. This is work based on and largely taken from the work done in the paper [6].

In the Sec. 1.3.2, we gave a brief overview of what Weyl semimetals are and the possibilities for experimental realizations. At the time of this writing, there has not been an experimental realization of the time-reversal symmetry breaking variety (but there has been some that break inversion symmetry [195]), so we proceed with a discussion including the pure band structure. We begin first with the electrodynamics in the Weyl semimetal resulting from an axionic action (which results in a bulk Hall effect). Using the reflection coefficients, we calculate the Casimir effect, Fig. 4.2. From there, we connect this to the known thin-film result for Chern insulators [38, 39] by making the object a thickness d as seen in Fig. 4.1 and results in Fig. 4.4.

Taking $d \ll a$ justifies a thin film limit where the two-dimensional conductivities are $\sigma_{\mu\nu}^{\mathrm{2D}} = \sigma_{\mu\nu} d$. In this case, we investigate the role that the full frequency response of the conductivities has on the Casimir effect—finding that at shorter

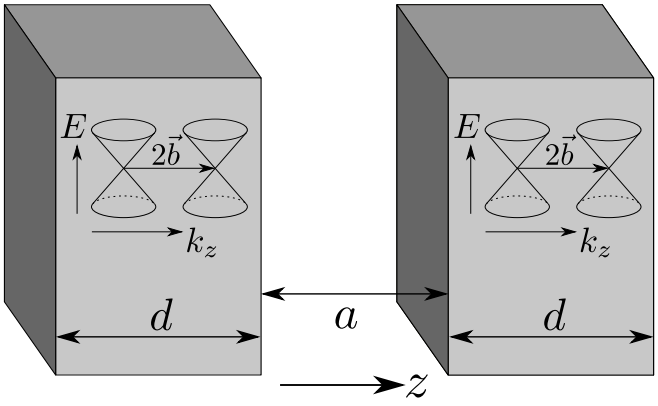

Figure 4.1: The setup we will consider here is two Weyl semimetals separated by a distance a in vacuum, and with distance between Weyl cones $2\mathbf{b}$ in k-space (split in the z-direction).

distances, attraction prevails, creating an "anti-trap" Figs. 4.5, 4.6, and 4.8.

From here, we tune the chemical potential in order to guarantee long distance attraction simulating the effect of a finite DC conductivity (see the appendix B). This reveals a finite region where the plates remain repulsive.

In this letter, we are concerned with Casimir repulsion in identical time-reversal broken systems. Specifically, we will study how Weyl semimetals with time-reversal symmetry breaking can exhibit Casimir repulsion. The key ingredient to Casimir repulsion in this letter is the existence of a nonzero bulk Hall conductance $\sigma_{xy} \neq 0$, $\sigma_{xy} = -\sigma_{yx}$ [9].

The material we are interested in is marginal in both the case of longitudinal conductance and an overwhelming Hall effect: Weyl semimetals [9] with the Casimir setup seen in Fig. 4.1 and resulting normalized Casimir pressure in Fig. 4.4.

We simulate this effect in the latter part of this letter by raising the chemical

potential in our clean system, leading to intraband transitions that contribute to the longitudinal conductivity (in the DC limit these are singular contributions).

4.2 Electrodynamics of a bulk-Hall effect

While the reference [117] discusses the electrodynamics we discuss here, it only gives the dispersion relation. So, we present as part of this work the derivation of the electrodynamics inside this material.

First, as we discussed in Sec. 1.3.2, the action that modifies the usual Maxwell action $S_0 = -\frac{1}{4}\int d^4x\, F_{\mu\nu}F^{\mu\nu}$ is

$$S_A = \frac{e^2}{32\pi^2\hbar c}\int d^3r\, dt\, \theta(\mathbf{r},t)\epsilon^{\mu\nu\alpha\beta}F_{\mu\nu}F_{\alpha\beta}, \tag{4.1}$$

where $\theta(\mathbf{r},t) = 2\mathbf{b}\cdot\mathbf{r} - 2b_0 t$, and $2\mathbf{b}$ is the distance between Weyl nodes in $\mathbf{k}$-space while $2b_0$ is their energy offset; e is the charge of an electron; $\hbar$ is Planck's constant; c is the speed of light; $F_{\mu\nu} = \partial_\mu A_\nu - \partial_\nu A_\mu$ is the electromagnetic field strength tensor; and $\epsilon^{\mu\nu\alpha\beta}$ is the fully antisymmetric 4-tensor. From here on out we will use the fine-structure constant $\alpha = e^2/4\pi\hbar c \approx 1/137$ where convenient.

These yield the following Maxwell equations [117]

$$\begin{aligned}
\nabla\cdot\mathbf{E} &= -\frac{2}{\pi}\alpha\mathbf{b}\cdot\mathbf{B},\\
\nabla\times\mathbf{B} &= \frac{1}{c}\frac{\partial\mathbf{E}}{\partial t} + \frac{2}{\pi}\alpha(b_0\mathbf{B} + \mathbf{b}\times\mathbf{E}),\\
\nabla\cdot\mathbf{B} &= 0,\\
\nabla\times\mathbf{E} &= -\frac{1}{c}\frac{\partial\mathbf{B}}{\partial t}
\end{aligned} \tag{4.2}$$

Consider this material in the semi-infinite space $z > 0$. First, we confirm that this does not produce any surface currents.

The action can be written simply as

$$S_A = \frac{e^2}{8\pi^2\hbar c}\int_{z>0} d^3r\, dt\, \theta(\mathbf{r},t)\epsilon^{\mu\nu\alpha\beta}\partial_\mu A_\nu \partial_\alpha A_\beta. \tag{4.3}$$

If we take the functional derivative, we obtain the 4-current $j^\mu(x) = \frac{\delta S_A}{\delta A_\mu(x)}$ with the form

$$j^\mu(x) = \frac{\alpha}{\pi}[\Theta(z)\epsilon^{\mu\nu\alpha\beta}\partial_\nu\theta(x)\,\partial_\alpha A_\beta + \delta(z)\theta(x)\epsilon^{\mu\alpha\beta z}\partial_\alpha A_\beta]. \tag{4.4}$$

The term proportional to the Heaviside theta function $\Theta(z)$ is just the bulk response that we have already written down in Eq. (4.2), but the other term is a boundary term (proportional to the Dirac delta-function $\delta(z)$), and it diverges at large x since $\theta(x)$ is not bounded in our case.

Thus, in order to simplify things, we let $b_0 = 0$ and $\mathbf{b} = b\hat{\mathbf{z}}$. This ensures that there is no surface current since $\theta(z=0) = 0$; we are purely looking at the bulk Hall effect in this material. The other surfaces with a surface current have the so-called Fermi-arcs [9], and for this work we won't consider them.

In the material itself Maxwell's equations (4.2) are satisfied. To keep track of the Hall response, $\sigma_{xy} = \frac{e^2 b}{2\pi^2\hbar}$ so that Maxwell's equations take the form in k-space

$$\mathbf{k}\cdot\mathbf{E} = -i\frac{\sigma_{xy}}{c}\hat{\mathbf{z}}\cdot\mathbf{B} \tag{4.5}$$

$$\mathbf{k}\times\mathbf{B} = -\frac{\omega}{c}\mathbf{E} + i\frac{\sigma_{xy}}{c}\hat{\mathbf{z}}\times\mathbf{E} \tag{4.6}$$

$$\mathbf{k}\cdot\mathbf{B} = 0 \tag{4.7}$$

$$\mathbf{k}\times\mathbf{E} = \frac{\omega}{c}\mathbf{B} \tag{4.8}$$

If we take Eq. (4.8) and substitute it into Eq. (4.5), we obtain a modified equation

$$\mathbf{k}\cdot\left(\mathbf{E} - i\frac{\sigma_{xy}}{\omega}\hat{\mathbf{z}}\times\mathbf{E}\right) = 0, \tag{4.9}$$

as well as the rewriting of Eq. (4.6)

$$\mathbf{k} \times \mathbf{B} = -\frac{\omega}{c}\left(\mathbf{E} - i\frac{\sigma_{xy}}{\omega}\hat{z} \times \mathbf{E}\right). \tag{4.10}$$

This suggests the displacement field $\mathbf{D} = \mathbf{E} - i\frac{\sigma_{xy}}{\omega}\hat{z} \times \mathbf{E}$ which corresponds to a frequency-dependent dielectric constant

$$\epsilon(\omega) = \begin{pmatrix} 1 & i\sigma_{xy}/\omega & 0 \\ -i\sigma_{xy}/\omega & 1 & 0 \\ 0 & 0 & 1 \end{pmatrix}. \tag{4.11}$$

With this, we can combine Maxwell's equations into (setting $c = 1$ for ease of calculations)

$$[\mathbf{k} \otimes \mathbf{k} - k^2\mathbb{I}]\epsilon^{-1}(\omega)\mathbf{D}(\omega) = \omega^2\mathbf{D}(\omega). \tag{4.12}$$

If we assume we have a wave vector $\mathbf{k}$ propagating in this material, then we can determine the two polarizations by taking the determinant of the matrix in Eq. (4.12)

$$\det[\mathbf{k} \otimes \mathbf{k} - k^2\mathbb{I} + \omega^2\epsilon(\omega)] = 0. \tag{4.13}$$

Solving for $\omega = \omega_{\mathbf{k}}$ reveals two frequencies

$$(\omega_{\mathbf{k}}^{\pm})^2 = k^2 + \tfrac{1}{2}\sigma_{xy}^2 \pm \sigma_{xy}\sqrt{k_z^2 + \tfrac{1}{4}\sigma_{xy}^2}. \tag{4.14}$$

Now, to figure out what the polarizations are, we use the fact that we still have rotational symmetry in the xy-plane, and that $\mathbf{k} \cdot \mathbf{D} = 0$. Thus, as a basis for polarizations, we choose $\mathbf{e}_1 = \frac{1}{k}(-k_z, 0, k_x)$ and $\mathbf{e}_2 = (0, 1, 0)$ with $\mathbf{k} = (k_x, 0, k_z)$.

The resulting equations for $\mathbf{D}^{\pm}(\mathbf{k})$ can be solved by usual linear algebra, resulting in the unnormalized vector

$$\tilde{\mathbf{D}}^{\pm}(\mathbf{k}) = \tfrac{\omega_{\mathbf{k}}^{\pm}}{k}(\sqrt{k_z^2 + \tfrac{1}{4}\sigma_{xy}^2} \mp \tfrac{1}{2}\sigma_{xy})\mathbf{e}_1 \pm ik_z\mathbf{e}_2. \tag{4.15}$$

Notice how the polarizations $\tilde{\mathbf{D}}^{\pm}(\mathbf{k})$ are elliptical in opposite ways, and oscillate at different frequencies. The former property will lead to interesting reflection and transmission properties—essential ingredients to the calculating of the Casimir effect.

4.3 Reflection off a bulk-Hall system

Now consider a wave in the vacuum coming towards the material ($z < 0$) incident on the material with wave vector $\mathbf{k}$ ($k_z > 0$). Due to time translational invariance and spatial invariance in the x and y directions, k_x, k_y, and ω remain the same between materials, but k_z changes across the boundary. To assess this, we match $\omega^2 = k_x^2 + k_y^2 + k_z^2$ to the dispersion in Eq. (4.14) to obtain the two new $k_z^{\pm}$. We find (restoring c)

$$(k_z^{\pm})^2 = k_z(k_z \pm \sigma_{xy}/c). \tag{4.16}$$

Along with the polarization vectors (these are not the same as $\tilde{\mathbf{D}}^{\pm}$, those kept $\mathbf{k}$ constant, these keep everything but k_z constant)

$$\mathbf{D}^{\pm} = \tfrac{k}{k^{\pm}}\mathbf{e}_1 \mp i\tfrac{k_z}{k_z^{\pm}}\mathbf{e}_2. \tag{4.17}$$

Notice that for $k_z < |\sigma_{xy}/c|$, one of the elliptical polarizations does not propagate into the material, independent of angle of incidence.

Now, to obtain the reflection matrix, we call our incident wave $\mathbf{E}_0$ with previously defined wave-vector $\mathbf{k}$. Our reflected wave $\mathbf{E}_r$ has wave-vector $\mathbf{k}_r = (k_x, k_y, -k_z)$, and in the material $\mathbf{E}^{\pm} = \epsilon^{-1}(\omega)\mathbf{D}^{\pm}$ are the two polarizations transmitted with wave vectors $\mathbf{k}_{\pm}$. The relevant Maxwell equations at the interface

between vacuum and the bulk-Hall material are then given by matching the electric and magnetic field parallel to the surface

$$\begin{aligned}(\mathbf{E}_0 + \mathbf{E}_r - \mathbf{E}_+ - \mathbf{E}_-) \times \hat{\mathbf{z}} = 0,\\ (\mathbf{q} \times \mathbf{E}_0 + \mathbf{q}_r \times \mathbf{E}_r - \mathbf{k}_+ \times \mathbf{E}_+ - \mathbf{k}_- \times \mathbf{E}_-) \times \hat{\mathbf{z}} = 0.\end{aligned} \tag{4.18}$$

We can break up the polarization of the incident and reflected waves into transverse electric (TE) and transverse magnetic (TM) where $\mathbf{E} = E^{\mathrm{TM}}\mathbf{e}_1 + E^{\mathrm{TE}}\mathbf{e}_2$, and the reflection matrix is defined such that

$$\begin{pmatrix} E_r^{\mathrm{TM}} \\ \\ E_r^{\mathrm{TE}} \end{pmatrix} = R(\omega, \mathbf{k}) \begin{pmatrix} E_0^{\mathrm{TM}} \\ \\ E_0^{\mathrm{TE}} \end{pmatrix}. \tag{4.19}$$

Note that $R(\omega, \mathbf{k})$ is being written as a function of ω, k_x, and k_y; k_z is defined in terms of them. Solving for these sets of equations for $\mathbf{E}_r$ in terms of $\mathbf{E}_0$, we obtain

$$R_\infty(\omega, \mathbf{k}) = \frac{c}{\sigma_{xy}} \begin{pmatrix} \sigma_{xy}/c + k_z^- - k_z^+ & i(2k_z - k_z^- - k_z^+) \\ \\ -i(2k_z - k_z^- - k_z^+) & \sigma_{xy}/c + k_z^- - k_z^+ \end{pmatrix}. \tag{4.20}$$

For the Lifshitz formula (see Eq. (1.8)), it is calculationally useful to put this formula in terms of imaginary frequency $\omega \to i\omega$ and define $q_z^2 = \omega^2/c^2 + k_x^2 + k_y^2 = -k_z^2$ and so we can let $k_z \to iq_z$. Rotating $k_z^\pm$ is problematic due to branch cuts in the square root function, so we rewrite the above expressions before we make the rotations using

$$k_z^+ \pm k_z^- = \sqrt{2k_z(k_z \pm \sqrt{k_z^2 - \sigma_{xy}^2/c^2})}. \tag{4.21}$$

Rotating from the real k_z axis to the imaginary $k_z = iq_z$ axis is now not an issue, the only relevant branch cut is for $k_z < \alpha$ and slightly below the real-axis. Defining

$$Q_\pm = \sqrt{2q_z(\sqrt{q_z^2 + \sigma_{xy}^2/c^2} \pm q_z)}, \tag{4.22}$$

the rotated version of Eq. (4.20) takes the form

$$R_\infty(iq_z) = \frac{1}{\sigma_{xy}/c}\begin{pmatrix} Q_- - \sigma_{xy}/c & -Q_+ + 2q_z \\ Q_+ - 2q_z & Q_- - \sigma_{xy}/c \end{pmatrix}. \tag{4.23}$$

But we are also interested in thickness dependence, not just the semi-infinite case. This requires restricting our action Eq. (4.1) to $0 < z < d$. To solve this, we just need to add another set of matching conditions. In addition to the incident $\mathbf{E}_0$ and reflected $\mathbf{E}_r$ waves, we now have forward moving Weyl polarizations $\mathbf{E}^\uparrow_\pm$ with $\mathbf{k}^\uparrow_\pm = (k_x, k_y, k^\pm_z)$, backwards moving Weyl polarizations $\mathbf{E}^\downarrow_\pm$ with $\mathbf{k}^\downarrow_\pm = (k_x, k_y, -k^\pm_z)$, and a transmitted wave $\mathbf{E}_t$ with wave-vector the same as the transmitted $\mathbf{k}$.

The resulting matching conditions are

$$\begin{aligned}
(\mathbf{E}_0 + \mathbf{E}_r - \mathbf{E}^\uparrow_+ - \mathbf{E}^\uparrow_- - \mathbf{E}^\downarrow_+ - \mathbf{E}^\downarrow_-) \times \hat{\mathbf{z}} = 0,\\
(\mathbf{k}\times\mathbf{E}_0 + \mathbf{k}_r\times\mathbf{E}_r - \mathbf{k}^\uparrow_+\times\mathbf{E}^\uparrow_+ - \mathbf{k}^\uparrow_-\times\mathbf{E}^\uparrow_- - \mathbf{k}^\downarrow_+\times\mathbf{E}^\downarrow_+ - \mathbf{k}^\downarrow_-\times\mathbf{E}^\downarrow_-) \times \hat{\mathbf{z}} = 0,\\
(\mathbf{E}^\uparrow_+ e^{ik^+_z d} + \mathbf{E}^\uparrow_- e^{ik^-_z d} + \mathbf{E}^\downarrow_+ e^{-ik^+_z d} + \mathbf{E}^\downarrow_- e^{-ik^-_z d} - \mathbf{E}_t e^{ik_z d}) \times \hat{\mathbf{z}} = 0,\\
(\mathbf{k}^\uparrow_+\times\mathbf{E}^\uparrow_+ e^{ik^+_z d} + \mathbf{k}^\uparrow_-\times\mathbf{E}^\uparrow_- e^{ik^-_z d}\\
+\mathbf{k}^\downarrow_+\times\mathbf{E}^\downarrow_+ e^{-ik^+_z d} + \mathbf{k}^\downarrow_-\times\mathbf{E}^\downarrow_- e^{-ik^-_z d} - \mathbf{k}\times\mathbf{E}_t e^{ik_z d}) \times \hat{\mathbf{z}} = 0.
\end{aligned} \tag{4.24}$$

These equations can still be solved for the reflection matrix with the result

$$R_d(\omega, \mathbf{q}) = \begin{pmatrix} R_{xx}(\omega,\mathbf{q}) & R_{xy}(\omega,\mathbf{q}) \\ -R_{xy}(\omega,\mathbf{q}) & R_{xx}(\omega,\mathbf{q}) \end{pmatrix}, \tag{4.25}$$

where

$$R_{xx}(\omega,\mathbf{q}) = \sigma_{xy}\{\sin(k_z^- d)[ik_z^+\cos(k_z^+ d) + \sigma_{xy}\sin(dk_z^+)] - ik_z^-\cos(k_z^- d)\sin(k_z^+ d)\}/D, \tag{4.26}$$

$$R_{xy}(\omega,\mathbf{q}) = \sigma_{xy}\{k_z^-\cos(k_z^- d)\sin(k_z^+ d) + \sin(k_z^- d)[k_z^+\cos(k_z^+ d) - 2ik_z\sin(k_z^+ d)]\}/D, \tag{4.27}$$

$$D = [2ik_z^-\cos(k_z^- d) + (2k_z - \sigma_{xy})\sin(k_z^- d)][2ik_z^+\cos(k_z^+ d) + (2k_z + \sigma_{xy})\sin(k_z^+ d)]. \tag{4.28}$$

Again, for analytic continuation purposes, it is useful to get the expression in terms of $k_z^+ \pm k_z^-$ which can be done and after the whole procedure is carried out and a lot of algebra done,

$$R_d(iq_z) = \begin{pmatrix} R_{xx}(iq_z) & R_{xy}(iq_z) \\ -R_{xy}(iq_z) & R_{xx}(iq_z) \end{pmatrix}, \tag{4.29}$$

with

$$R_{xx}(iq_z) = -\tfrac{1}{2}\tfrac{\sigma_{xy}}{c}(Q_-\sinh Q_+ d + \tfrac{\sigma_{xy}}{c}\cosh Q_+ d - Q_+\sin Q_- d - \tfrac{\sigma_{xy}}{c}\cos Q_- d)/D, \tag{4.30}$$

$$R_{xy}(iq_z) = -\tfrac{1}{2}\tfrac{\sigma_{xy}}{c}(Q_+\sinh Q_+ d + 2q_z\cosh Q_+ d - Q_-\sin Q_- d - 2q_z\cos Q_- d)/D, \tag{4.31}$$

where

$$D = (Q_+^2 + \tfrac{1}{2}\tfrac{\sigma_{xy}^2}{c^2})\cosh Q_+ d + (2q_z Q_+ + \tfrac{\sigma_{xy}}{c}Q_-)\sinh Q_+ d + (Q_-^2 - \tfrac{1}{2}\tfrac{\sigma_{xy}^2}{c^2})\cos Q_- d + (2q_z Q_- - \tfrac{\sigma_{xy}}{c}Q_+)\sin Q_- d. \tag{4.32}$$

There are two limits of this expression to consider. One is the semi-infinite limit where $q_z d \to \infty$, and the other is in the thin film limit where $q_z d \to 0$ as $\sigma_{xy} d = \sigma_{xy}^{\mathrm{2D}}$ is held constant.

In the limit as $q_z d \to \infty$, only the hyperbolic sines and cosines remain and we obtain

$$\lim_{q_z d \to \infty} R_{xx}(iq_z) = \frac{-\frac{1}{2}\frac{\sigma_{xy}}{c}(Q_- + \frac{\sigma_{xy}}{c})}{Q_+^2 + \frac{1}{2}\frac{\sigma_{xy}^2}{c^2} + 2q_z Q_+ + \frac{\sigma_{xy}}{c} Q_-} = \frac{Q_- - \sigma_{xy}/c}{\sigma_{xy}/c}, \tag{4.33}$$

$$\lim_{q_z d \to \infty} R_{xy}(iq_z) = \frac{-\frac{1}{2}\frac{\sigma_{xy}}{c}(Q_+ + 2q_z)}{Q_+^2 + \frac{1}{2}\frac{\sigma_{xy}^2}{c^2} + 2q_z Q_+ + \frac{\sigma_{xy}}{c} Q_-} = \frac{2q_z - Q_+}{\sigma_{xy}/c}. \tag{4.34}$$

We have recovered the semi-infinite limit.

On the other hand, the thin film result as found by [39, 109] and derived for completion in Appendix A (setting $\sigma_{xx} = \sigma_{yy} = 0$ as well as $\sigma_{xy} = -\sigma_{yx}$) is

$$R_0(iq_z) = \frac{1}{1 + (\sigma_{xy}^{\mathrm{2D}}/2c)^2} \begin{pmatrix} -(\sigma_{xy}^{\mathrm{2D}}/2c)^2 & -\sigma_{xy}^{\mathrm{2D}}/2c \\ \sigma_{xy}^{\mathrm{2D}}/2c & -(\sigma_{xy}^{\mathrm{2D}}/2c)^2 \end{pmatrix}, \tag{4.35}$$

And indeed, if $\sigma_{xy} d \equiv \sigma_{xy}^{\mathrm{2D}}$ is held constant, then

$$\lim_{q_z d \to 0} R_d(iq_z) = R_0. \tag{4.36}$$

Thus, R_d interpolates between the thin film and semi-infinite case. We will see in the next section that these limits are both important in the calculation of the Casimir effect.

4.4 The Casimir effect between two idealized Weyl semimetals

To begin this section we quote again the formula for the Casimir force obtained from the Lifshitz formula Eq. (1.8), the source of the main integral which we

compute. If R_1 and R_2 are the reflection matrices for plates 1 and 2 respectively and they are separated by a distance a, then the Casimir pressure is

$$P_c(a) = 2\hbar \int \frac{d^2k}{(2\pi)^2} \int \frac{d\omega}{2\pi}\, q_z \,\mathrm{tr}([\mathbb{I} - R_1 R_2 e^{-2q_z a}]^{-1} R_1 R_2) e^{-2q_z a},, \tag{4.37}$$

where the trace is a matrix trace and $q_z = \sqrt{\omega^2/c^2 + k^2}$. This integral generally yields an attractive force; however, if we break time reversal symmetry as the Weyl semimetals do, we can obtain antisymmetric off-diagonal terms for the reflection matrix $R_{xy} = -R_{yx}$ there is the possibility of Casimir repulsion [40].

Considering the semi-infinite case first, we see that $R_\infty(iq_z)$ only depends on the ratio cq_z/σ_{xy}. This dependence has implications for the Casimir force. After changing variables to solely q_z, we can inspect the Casimir pressure, and we have an expression

$$P_c = \frac{2\hbar c}{(2\pi)^2} \int dq_z\, q_z^3\, g\left[\tfrac{q_z}{\sigma_{xy}/c}, 2q_z a\right], \tag{4.38}$$

with a function $g(\frac{q_z}{\sigma_{xy}/c}, 2q_z a)$ given by

$$g(\tfrac{q_z}{\sigma_{xy}/c}, 2q_z a) = \mathrm{tr}([\mathbb{I} - R_\infty(iq_z)^2 e^{-2q_z a}]^{-1} R_\infty(iq_z)^2) e^{-2q_z a} \tag{4.39}$$

If we then change variables to $x = 2aq_z$ and normalize by Casimir's original result for perfect conductors $P_0 = -\frac{\hbar c \pi^2}{240 a^4}$ [2], we can write the equation for the pressure as

$$P_c = -P_0 \frac{15}{2\pi^4} \int_0^\infty dx\, x^3\, g\left[\tfrac{x}{2\sigma_{xy} a/c}, x\right], \tag{4.40}$$

so $P_c/P_0 = f(\sigma_{xy} a/c)$ a function of only $\sigma_{xy} a/c$.

With this formulation, we plot normalized force P_c/P_0 as a function of $\sigma_{xy} a/c$ obtaining the single function seen in Fig. 4.2. We see that for $\sigma_{xy} a/c \lesssim 4.00$ we

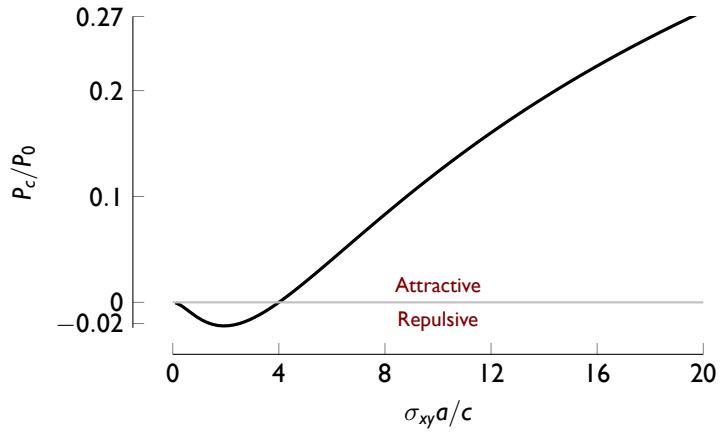

Figure 4.2: The normalized Casimir force between two semi-infinite bulk Hall materials. Repulsion is seen for $\sigma_{xy}a/c \lesssim 4.00$. $P_0 = -\frac{\hbar c\pi^2}{240a^4}$ is the distant-dependent ideal Casimir Force [2]. For $\sigma_{xy}a/c \to \infty$, $P_c/P_0 \to 1$.

obtain repulsion while for $\sigma_{xy}a/c \gtrsim 4.00$ we obtain attraction. Thus, these similar materials trap each other at a fixed distance simply dependent on the Hall conductivity,

$$a_{\text{Trap}} \approx \frac{4.00}{\sigma_{xy}/c}. \tag{4.41}$$

If we insert the value of $\sigma_{xy} = e^2 b/2\pi^2\hbar$ into this expression, we find $a_{\text{Trap}} \approx 860/b$. This means that if $1/b \sim O(\text{nm})$, then $a_{\text{Trap}} \sim O(\mu\text{m})$ quite reasonable.

As the distance between the materials gets large, $P_c/P_0 \to 1$. This behavior is markedly different from the thin film Hall case obtained by Tse and MacDonald in [38, 39]. They found a small (two-dimensional) quantum Hall effect implies a quantized and repulsive Casimir force at large distance. In our case, we get attraction at large distances for a bulk Hall material independent of the magnitude of the Hall effect. To resolve this seeming inconsistency, imagine a finite thickness

of the bulk Hall material of thickness d, then the two-dimensional conductivity $\sigma_{xy}d$ diverges as $d \to \infty$, and in the case of a 2D quantum Hall plate with infinite Hall conductivity, the Casimir effect is attractive and approaches P_0.

To make this argument more precise, we consider Weyl plates that are of thickness d (using R_d given in Eq. (4.29))

Notice that we can write R_d as a function of only two variables $R_d = R_d(cq_z/\sigma_{xy}, \sigma_{xy}^{\mathrm{2D}}/c)$ where $\sigma_{xy}^{\mathrm{2D}} = \sigma_{xy}d$. Thus, we can perform similar transformations as before to see that the Casimir force for two ideal Weyl semimetals of thickness d,

$$P_c = -P_0 \frac{15}{2\pi^4} \int_0^\infty dx\, x^3\; g\Big[\tfrac{x}{2\sigma_{xy}a/c}, \sigma_{xy}d/c, x\Big]\,. \tag{4.42}$$

Thus, we have $P_c = P_0 f(\sigma_{xy}a/c, \sigma_{xy}d/c)$.

The limiting cases can be understood now by considering first Eq. (4.37). The exponential constrains $q_z \sim 1/a$ and since the "thin-film" limit is $\lim_{q_z d\to 0} R_d(iq_z) = R_0(iq_z)$, we have that $d/a \to 0$. In other words, the thin film limit is applicable when we are considering $d \ll a$. Notably, it applies when we're in the long distance limit independent of thickness. The opposite limit is just when $q_z d \to \infty$, and by similar arguments, that means $d \gg a$ is when the semi-infinite case applies. Both limits leave $\sigma_{xy}a/c$ and $\sigma_{xy}d/c$ unaffected (though in the thin film case $\sigma_{xy}a$ drops out while in the semi-infinite case $\sigma_{xy}d \to \infty$ has the same limit as $q_z d \to \infty$).

We can thus conclude that no matter what we calculate, for $a \gg d$, we should eventually approach the thin film limit. The thin film limit can actually be calculated exactly [38, 39] and is

$$P_c^{\mathrm{TF}} = P_0 \frac{90}{\pi^4} \,\mathrm{Re}\{\mathrm{Li}_4\left[(\sigma_{xy}^{\mathrm{2D}}/c)^2/(\sigma_{xy}^{\mathrm{2D}}/c + 2i)^2\right]\} \tag{4.43}$$

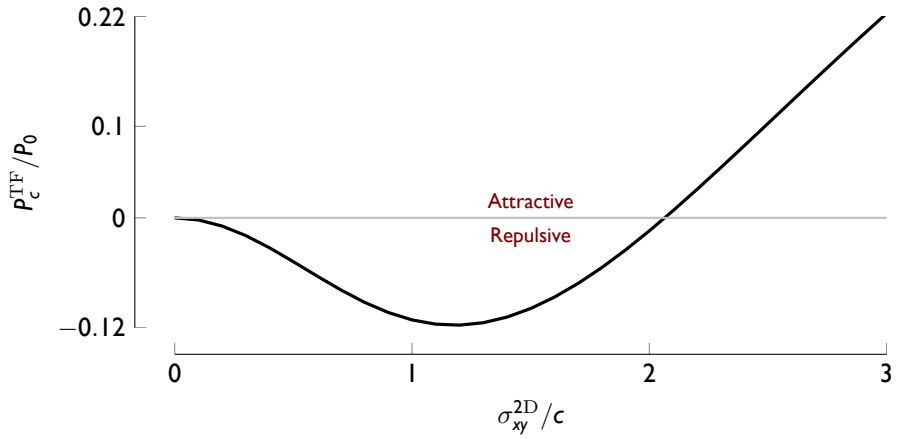

Figure 4.3: The normalized Casimir force for a thin film Hall plate. This is the value as a function of the Hall conductivity $\sigma_{xy}^{\mathrm{2D}}$ and it is inherently independent of distance (i.e. the pressure goes as $1/a^4$).

where Li_4 is the polylogarithm of degree 4, defined by

$$\mathrm{Li}_s(z) = \sum_{k=1}^{\infty} \frac{z^k}{k^s}.$$

The resulting P_c^{TF}/P_0 function is plotted in Fig. 4.3 as a function of $\sigma_{xy}^{\mathrm{2D}}$. Note that this function has a minimum value of $P_c^{\mathrm{TF}} \approx -0.117 P_0$ representing how repulsive we can get. For large enough $\sigma_{xy}^{\mathrm{2D}}/c$, the force does become attractive—corresponding roughly to when $(\sigma_{xy}^{\mathrm{2D}}/2c)^2 > \sigma_{xy}^{\mathrm{2D}}/2c$ (i.e. when Kerr rotation is suppressed as can be easily seen from Eq. (4.35)).

The cross-over between the thin film case and the semi-infinite case can be seen in Fig. 4.4. As $\sigma_{xy} d/c$ is increased, the Casimir energy approaches the semi-infinite case. However, for any finite d, each curve asymptotically approaches its thin-film value (and never goes lower than the minimum value represented by dashed horizontal line in Fig. 4.4). Thus, coming from the semi-infinite case, the trap gets

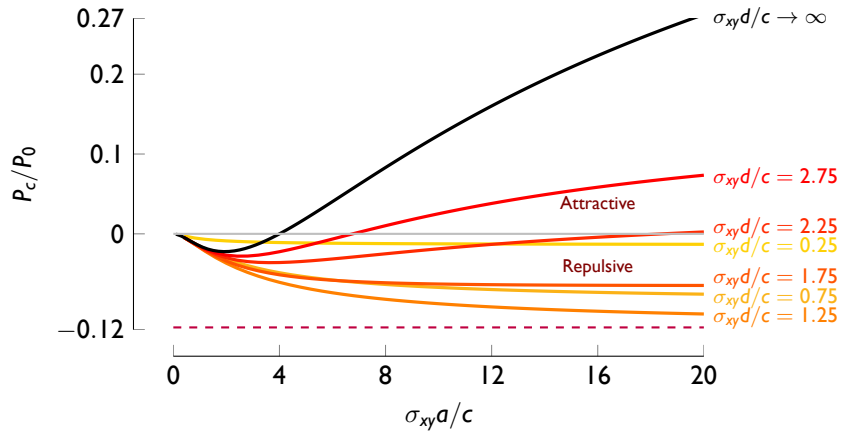

Figure 4.4: A plot of the normalized Casimir force for various thicknesses of a bulk Hall material (idealized Weyl semimetal). It begins slightly repulsive for small $\sigma_{xy}d/c$, and as this increases, it becomes more repulsive until it reaches the maximum for a thin film material (the dashed line) at which point it increases to the semi-infinite limit. $P_0 = -\frac{\hbar c\pi^2}{240a^4}$ and $\sigma_{xy} = e^2b/2\pi^2\hbar$ is the bulk Hall response. Figs. 4.5, 4.6, 4.7, and 4.8 takes into account more material properties.

pushed further and further out for smaller thicknesses until the Casimir pressure becomes purely repulsive for all distances. This not only clearly connects our case to the previously known thin-film result, it also provides a theoretical justification for considering a thin-film limit $d \ll a$ with a two-dimensional conductivity $\sigma_{\mu\nu} d$.

4.5 Conductivity for a clean Weyl semimetal

In order to add in more material effects and see how they might affect the Casimir force, we need to calculate the conductivity tensor for the band theory offered by Weyl semimetals.

We will mainly be interested in the effects of virtual vacuum transitions that are low in energy, which corresponds to plates that are far apart from one another (in the two-dimensional case, as seen in the Appendix B). Thus, we will use the low-energy chiral Hamiltonian for a pair of Weyl nodes

$$H_W = \pm \hbar v_{\mathrm{F}} \boldsymbol{\sigma} \cdot (\mathbf{k} \pm \mathbf{b}), \tag{4.44}$$

where v_{F} is the Fermi velocity and $\mathbf{b}$ is the position of the of Weyl node in $\mathbf{k}$-space. The exact band structure will be important as the plates get closer though weighting will still be larger on the lower energy modes.

For calculational ease, we set $\hbar = 1 = v_{\mathrm{F}}$. Now, if we calculate the conductivity for a fixed k_z, we obtain basically the same conductivity for the surface of a topological insulator with a chemical potential both in and out of the gap.

In fact, the eigenstates differ only slightly from that considered in Eq. (2.1).

We restrict ourselves to H_W with $k_z - b$. If $e^{i\mathbf{k}\cdot\mathbf{x}}|f_{\mathbf{k}\pm}\rangle$ diagonalizes H_W, then

$$\langle f_{k+}|\sigma_x|f_{k-}\rangle = \frac{(k_z-b)k_x + i\epsilon k_y}{\epsilon\sqrt{\epsilon^2-(k_z-b)^2}}, \tag{4.45}$$

$$\langle f_{k+}|\sigma_y|f_{k-}\rangle = \frac{(k_z-b)k_y - i\epsilon k_x}{\epsilon\sqrt{\epsilon^2-(k_z-b)^2}}, \tag{4.46}$$

$$\langle f_{k\pm}|\sigma_x|f_{k\pm}\rangle = \pm\frac{k_x}{\epsilon}, \tag{4.47}$$

where $\epsilon \equiv \sqrt{k_x^2+k_y^2+(k_z-b)^2}$. The inter-band contribution to the conductivity takes the form

$$\tilde{\sigma}^{\text{inter}}_{\mu\nu}(i\omega;k_z) = \frac{e^2}{i\hbar}\sum_{\mathbf{k},\gamma\neq\gamma'}\frac{n_{\mathbf{k}\gamma}-n_{\mathbf{k}\gamma'}}{\epsilon_{\mathbf{k}\gamma}-\epsilon_{\mathbf{k}\gamma'}}\frac{\langle f_{\mathbf{k}\gamma}|j_\mu|f_{\mathbf{k}\gamma'}\rangle\langle f_{\mathbf{k}\gamma'}|j_\nu|f_{\mathbf{k}\gamma}\rangle}{i\omega+\epsilon_{\mathbf{k}\gamma}-\epsilon_{\mathbf{k}\gamma'}}, \tag{4.48}$$

where $n_{\mathbf{k}\gamma}$ is the occupation in that band at momentum $\mathbf{k}$ and $j_\mu = \sigma_\mu$ are the single particle current operators. For intra-band quantities with $n_{\mathbf{k}\pm} = \theta(\mu \mp \epsilon_{\mathbf{k}})$

$$\tilde{\sigma}^{\text{intra}}_{\mu\nu}(i\omega;k_z) = -\frac{e^2}{i\hbar}\sum_{\mathbf{k}}\delta(\mu-\epsilon_{\mathbf{k},+})\frac{\langle f_{\mathbf{k}+}|j_\mu|f_{\mathbf{k}+}\rangle\langle f_{\mathbf{k}+}|j_\nu|f_{\mathbf{k}+}\rangle}{i\omega}, \tag{4.49}$$

assuming only the upper-band for simplicity and without loss of generality (due to particle-hole symmetry).

Putting these together and performing the integrals, we obtain the result at finite chemical potential

$$\tilde{\sigma}_{xx}(i\omega;k_z) = \frac{e^2}{4\pi\hbar}\left[\left(1-\frac{4(k_z-b)^2}{\omega^2}\right)\frac{i}{4}\log\left(\frac{2\Delta-i\omega}{2\Delta+i\omega}\right)+\frac{\Delta}{\omega}\right], \tag{4.50}$$

$$\tilde{\sigma}_{xy}(i\omega;k_z) = \frac{e^2}{2\pi\hbar}\left[\frac{k_z-b}{\omega}\frac{i}{2}\log\left(\frac{2\Delta-i\omega}{2\Delta+i\omega}\right)\right], \tag{4.51}$$

where $\Delta = \max\{|k_z-b|,|\mu|\}$. With these quantities we can then use the cutoff procedure explained in [196]

$$\sigma_{\mu\nu}(i\omega) = \int_{-\Lambda}^{\Lambda}\frac{dk_z}{2\pi}\tilde{\sigma}_{\mu\nu}(i\omega;k_z). \tag{4.52}$$

With Eq. (4.52) we obtain (throwing away terms that go to zero as the cutoff increases to infinity and multiplying by two for the two nodes and bringing back in the constants $\hbar$ and v_{F})

$$\sigma_{xx}(i\omega) = \frac{e^2}{12\pi^2\hbar v_{\mathrm{F}}}\left[\tfrac{5}{3}\omega + 2\omega\log\left(\tfrac{v_{\mathrm{F}}\Lambda}{\omega}\right) + 4\tfrac{\mu^2}{\hbar^2\omega} - \omega\log\left(1+\tfrac{4\mu^2}{\hbar^2\omega^2}\right)\right], \tag{4.53}$$

$$\sigma_{xy}(i\omega) = \frac{e^2 b}{2\pi^2\hbar}. \tag{4.54}$$

These quantities are what we use in the next section as input for the Casimir Force. Notice that $\sigma_{xy}(i\omega)$ is unchanged at this order. Due to the linear dispersion of the Weyl nodes, we have a logarithmic cutoff dependence. This regulation comes more naturally in a low energy theory that has parabolic k_z such as $H = \hbar v_{\mathrm{F}}[k_x\sigma_x + k_y\sigma_y + \ell(k_z^2 - b^2)\sigma_z]$, where ℓ is a length scale. Note that in Eq. (4.53), rotating to real frequencies we get the correct result for two Weyl nodes for $\mathrm{Re}[\sigma_{xx}(\omega)]$ [114], and a result with the appropriate logarithmic divergence for $\mathrm{Im}[\sigma_{xx}(\omega)]$ [197]. This can be understood in terms of charge renormalization due to the band structure, but for ease of our purposes we let $\Lambda \sim 1/a_0$ where a_0 is the lattice spacing. For our plots in Figs. 4.5, 4.6, 4.7, and 4.8 we choose a lattice spacing of $a_0 = 1\,\mathrm{nm}$, a thickness of $d = 20\,\mathrm{nm}$, $b = 0.3(2\pi/a_0)$, $\Lambda = 2\pi/a_0$, $v_{\mathrm{F}} = 6\times10^5\,\mathrm{m/s}$, and $\mu = 0$ unless its the parameter we are varying.

One can use one of the two equivalent ways of calculating the Casimir energy: the reflection matrix as given in [38] (and calculated in Appendix A) along with Lifshitz formula Eq. (1.8). In order to avoid an unphysical negative $\sigma_{xx}(i\omega)$ as well as for consistency, we cutoff the photon energies in the Lifshitz formula to run from 0 to Λ—an approximation valid for $a \gg \frac{c}{v_{\mathrm{F}}}\Lambda^{-1}$.

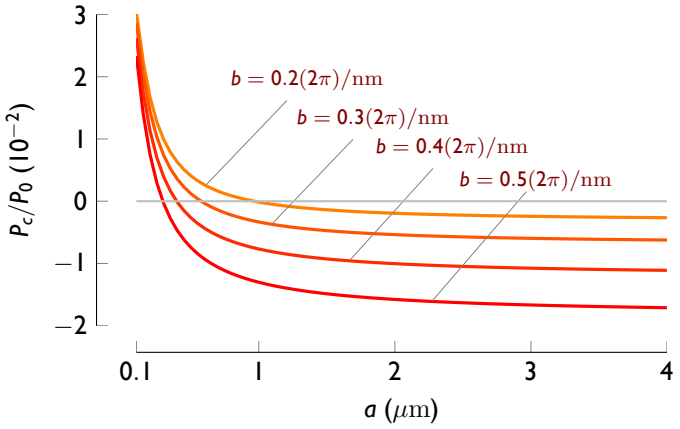

Figure 4.5: The Casimir force for a thin film Weyl semimetal taking into account low-energy virtual transitions in the band structure. An anti-trap clearly develops when the longitudinal conductivity overwhelms the Hall conductivity. We compare different values of b (or equivalently, changing the Hall effect). For this plot, $a_0 = 1\,\text{nm}$, $d = 20\,\text{nm}$, $\Lambda = 2\pi/a_0$, $v_\text{F} = 6 \times 10^5\,\text{m/s}$, and $\mu = 0$.

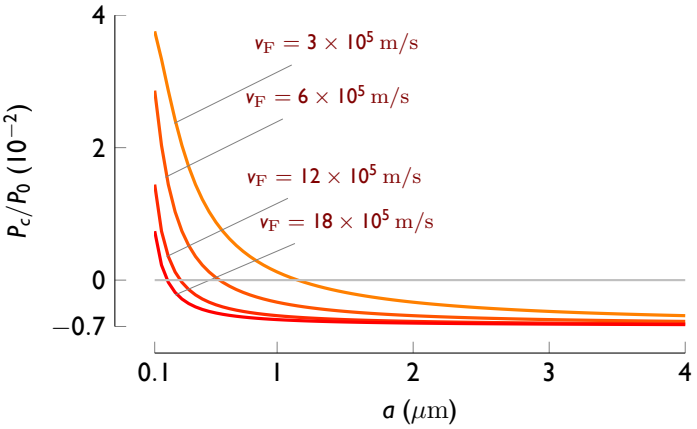

Figure 4.6: The Casimir force for a thin film Weyl semimetal taking into account low-energy virtual transitions in the band structure. Here we compare different v_F (the larger v_F the smaller σ_{xx} is). For this plot,$a_0 = 1\,\text{nm}$, $d = 20\,\text{nm}$, $b = 0.3(2\pi/a_0)$, $\Lambda = 2\pi/a_0$, and $\mu = 0$.

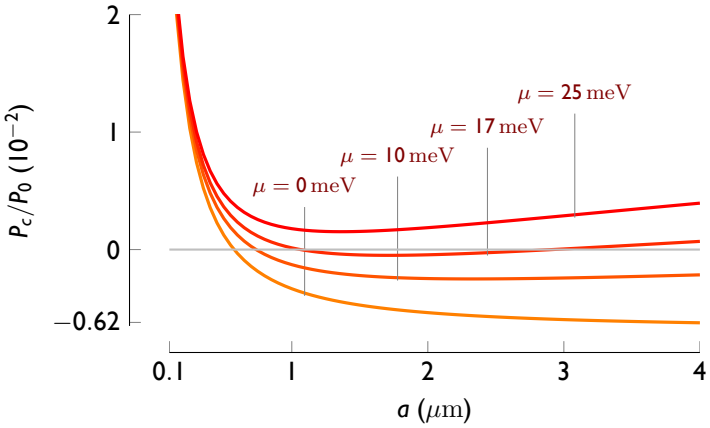

Figure 4.7: The Casimir force for a thin film Weyl semimetal taking into account low-energy virtual transitions in the band structure. Here we turn on a finite chemical potential which causes attraction at very large distances (and hence a trap). Even small chemical potentials have this property but the trap is quite far out. For this plot, $a_0 = 1\,\mathrm{nm}$, $d = 20\,\mathrm{nm}$, $b = 0.3(2\pi/a_0)$, $\Lambda = 2\pi/a_0$, and $v_\mathrm{F} = 6 \times 10^5\,\mathrm{m/s}$.

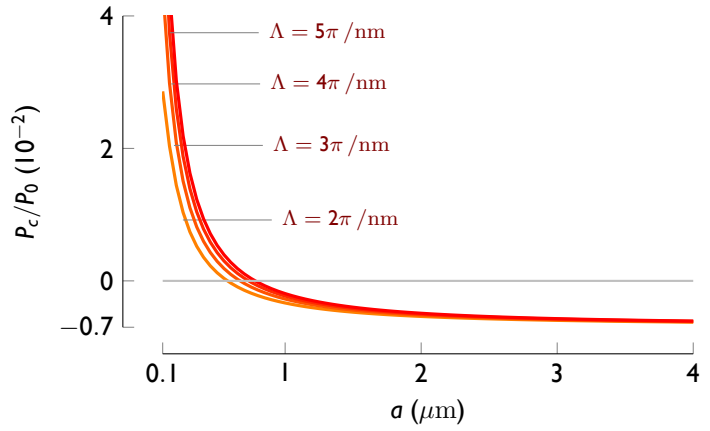

Figure 4.8: Here, we vary the cutoff to see how it depends. It is very similar to varying $v_\mathbf{F}$ as one can see in Fig. 4.6. For this plot, $a_0 = 1\,\mathrm{nm}$, $d = 20\,\mathrm{nm}$, $b = 0.3(2\pi/a_0)$, $v_\mathrm{F} = 6 \times 10^5\,\mathrm{m/s}$, and $\mu = 0$

First, in all of the plots in Figs. 4.5, 4.6, 4.7, and 4.8, we see that we get an anti-trap for these at approximately 650 nm, and if we increase b as in Fig. 4.5 (with, say, an applied magnetic field), it not only moves closer to zero separation, but the overall repulsive behavior can be enhanced. On the other hand, if we increase v_{F} as we see in Fig. 4.6, we see the region of attraction is suppressed, but the overall repulsive behavior at large distances is maintained. Modifying Λ, as we see in Fig. 4.8 will have effects similar to modifying v_{F}, but since it appears logarithmically, it needs to change by orders of magnitude to give appreciable changes. The cutoff Λ is actually a stand-in for higher band effects, and we can see that here it saves the analysis for short distances. This "anti-trap" effect occurs at short distances when higher order band effects also play a role, but any other effects will contribute to the longitudinal conductivity in such a way that an anti-trap will appear.

Interesting effects at larger distances begin to occur when we introduce a finite chemical potential as we see in Fig. 4.7. In addition to the anti-trap we get at shorter distances, we start to see a *trap* at much longer distances. This is not surprising since at zero frequency there is a divergent longitudinal conductivity, see Appendix B. Thus, we know that at long distances, the Casimir force must be attractive, but by modifying the Hall effect, we have an intermediate regime of repulsion.

A similar effect would occur if we took finite temperature or disorder corrections to the longitudinal conductivities—both yield finite DC conductivities.

4.6 Conclusions

Considering the form of the conductance in terms of the fine structure constant, $\sigma_{xy}d/c = \alpha\frac{2bd}{\pi}$, we see that bd controls the strength of the repulsion in the thin film limit. Without longitudinal conductance, the repulsive regime roughly corresponds to when $(\sigma_{xy}d/c)^2 \lesssim \sigma_{xy}d/c$ or equivalently $\frac{2bd}{\pi} \lesssim \frac{1}{\alpha}$. The longitudinal conductance introduces v_{F} into the scheme; relevant photons have $\omega \approx c/a$ and thus it becomes important for $\sigma_{xx}d/c \sim \alpha\frac{c}{v_{\mathrm{F}}}\frac{d}{a}$ (neglecting constants) which both emphasizes that v_{F} controls the longitudinal conductance's contribution to the Casimir effect and that the term is suppressed at longer distances.

We have shown here how Weyl semimetals can exhibit a tunable repulsive Casimir force (with, for instance, magnetic field tuning $\mathbf{b}$) and how it can depend on the thickness of the material. In the thin film limit, we showed how the semimetallic nature of these materials can work to create attraction at smaller distances scales, and how a finite longitudinal conductivity will create long distance attraction along with repulsion at intermediate distances. The marginal nature of these (at present purely theoretical) materials could be useful for controlling the Casimir force between attractive and repulsive regimes.

Chapter 5: The breakdown of the coherent state path integral

5.1 Overview

In this chapter, we change subjects away from optical and Casimir effects to a purely theoretical paradigm: path integration. This bares no relation to what we have previously discussed.

We outline another problem with the time-continuous coherent state path integral. This problem manifests itself in two simple examples: (i) the spin-coherent state path integral and (ii) the harmonic oscillator coherent state path integral (in particular, the single-site Bose-Hubbard model). The single-site Bose-Hubbard Hamiltonian is a minimal model that demonstrates the problem with the normal-ordered path integral. However, the problem itself is more general than the toy model considered here and clearly persists in more complicated models, including lattice Bose-Hubbard models. We use an exact method of calculating the partition function mathematically developed by Alekseev *et al.* [198] (and more recently used by Cabra *et al.* [199] for the spin path integral with $H = S_z$), and demonstrate that the exact result differs from the correct partition function in the cases of both normal-ordering of operators (as prescribed by most textbooks) and when using Weyl ordering (i.e., it cannot be accounted for with the phase anomaly found by

Solari and Kochetov [153, 155] and elaborated on by Stone *et al.* [154]).

This breakdown is yet to be fully resolved, but there has been interesting effort in this regard by others inspired by this work [200]. The culprit of the problem seems to be, unsurprisingly to those familiar with coherent state path integrals, the continuity assumption for paths. However, the path integral works just fine when one has a Hamiltonian that is a linear combination of generators of some Lie algebra used to generate the coherent states. We illustrate these points with two examples, and elaborate on the analysis of these points in what follows.

This chapter is mostly based on the paper [7], copyright APS.

5.2 Breakdown of the spin-coherent state path integral

We begin with the coherent state path integral for spin with the standard SU(2) algebra defined on the operators $\{S_x, S_y, S_z\}$ with $[S_i, S_j] = i\epsilon_{ijk}S_k$, and we define our Hilbert space by taking the matrix representation of the SU(2) group in $(2s+1)$-by-$(2s+1)$ matrices (s being the spin of the system). Irrespective of the algebra, we can in general define a Hermitian matrix H that acts on states in our Hilbert space, and this will be our Hamiltonian. Generally, H can be written as a polynomial of algebra generators.

If $|s\rangle$ is the maximal state of S_z in our spin-s system, then we can define spin-coherent states as

$$|\mathbf{n}\rangle = e^{-i\phi S_z} e^{-i\theta S_y} |s\rangle \tag{5.1}$$

where (θ, ϕ) are coordinates on the sphere S^2 along the unit vector $\mathbf{n}$ (i.e., a point

on the standard Bloch sphere). These coherent states are overcomplete such that

$$\frac{2s+1}{4\pi}\int_{S^2} d\mathbf{n}\,|\mathbf{n}\rangle\,\langle\mathbf{n}| = 1 \tag{5.2}$$

where $d\mathbf{n} = d\phi\, d(\cos\theta)$ is the standard measure on S^2. Using this continuous, overcomplete basis, one can derive the standard path integral for the partition function for spin from $\mathcal{Z} = \operatorname{tr} e^{-\beta H}$ in the standard way [136] discussed in the Sec. 1.5

$$\mathcal{Z}' = \int \mathcal{D}\mathbf{n}(\tau)\,\exp\left\{-\int_0^\beta d\tau\,[-\langle\mathbf{n}(\tau)|\partial_\tau\mathbf{n}(\tau)\rangle + \langle\mathbf{n}(\tau)|H|\mathbf{n}(\tau)\rangle]\right\}. \tag{5.3}$$

We call the partition function as given by the time-continuous path integral $\mathcal{Z}'$ in order to distinguish it from $\mathcal{Z} = \operatorname{tr} e^{-\beta H}$ since we will find that in general they may not agree. The path integral is over all closed paths (since it is the parititon function). The first term in the action for Eq. (5.3), $\langle\mathbf{n}|\partial_\tau\mathbf{n}\rangle$, is the Berry phase term and in (θ,ϕ) coordinates

$$-\langle\mathbf{n}|\partial_\tau\mathbf{n}\rangle = -is(1-\cos\theta)\partial_\tau\phi. \tag{5.4}$$

We assume $\langle\mathbf{n}|H|\mathbf{n}\rangle = H(\cos\theta)$ for some function $H(x)$ (this is true if and only if H is diagonal). This puts the ϕ dependence of the action solely in the Berry phase term of the action. We then integrate the Berry phase term by parts; the boundary term becomes

$$\int_0^\beta d\tau\ \langle\mathbf{n}(\tau)|\partial_\tau\mathbf{n}(\tau)\rangle = is(\phi(\beta)-\phi(0))(1-\cos\theta(0)) + is\int_0^\beta d\tau\,\phi(\tau)\frac{d\cos\theta}{d\tau}, \tag{5.5}$$

remembering that the paths considered in $\mathcal{Z}'$ are closed paths (so $\cos\theta(0) = \cos\theta(\beta)$). By the same logic, $\phi(\beta) = \phi(0) + 2\pi k$ for any integer k, and we can break up the integral into topological sectors given by the integer k (the winding number of a path

around the z-axis). Note that this makes the (perfectly reasonable) assumption for continuous paths that the ϕ-integral is the universal covering of S^1 (simply: the real numbers).

At this point in calculations our path integral now takes the form

$$\mathcal{Z}' = \sum_{k\in\mathbb{Z}} \int \mathcal{D}\mathbf{n}(\tau)\, \exp\Big\{2\pi i s k(1-\cos\theta(0)) + is\int_0^\beta d\tau\phi(\tau)\frac{d\cos\theta}{d\tau} - \int_0^\beta d\tau H(\cos\theta)\Big\}, \quad (5.6)$$

and we can now consider the measure $\mathcal{D}\mathbf{n}(\tau) = \mathcal{D}\phi\,\mathcal{D}(\cos\theta)$. For each time-slice $\mathcal{D}\phi$ integrates over the universal covering of S^1, so we can perform this integral. This is due to the fact that our only ϕ-dependence is multiplying $\frac{d\cos\theta}{d\tau}$ from integrating by parts, and we use the standard identity for functional integrals (derived easily from a the usual δ-function identity)

$$\int \mathcal{D}\phi\, e^{-i\int_0^\beta d\tau\,\phi(\tau)f(\tau)} = \delta(f), \quad (5.7)$$

to get that $\cos\theta$ must be constant (i.e., $\frac{d\cos\theta}{d\tau} = 0$). This δ-function allows us to do the path integral over $\mathcal{D}(\cos\theta)$, except for the initial value which we call $x := \cos\theta(0)$[1]. Taking all of this into account, the path integral can then be written as

$$\mathcal{Z}' = \sum_{k=-\infty}^{\infty} \int_{-1}^{1} dx\, e^{2\pi i k s(1-x)-\beta H(x)}. \quad (5.8)$$

The sum over k can be evaluated as a sum of delta functions using the formula

$$\sum_{k=-\infty}^{\infty} e^{2\pi k s(1-x)} = \sum_{n=-\infty}^{\infty} \delta(s(1-x)-n) \quad (5.9)$$

[1]This is even clearer in the case of a time slice picture, where each time slice imposes $f(\tau_i) = f(\tau_{i+1})$ except that one of these remains undefined, which we take to be $f(0)$ for convenience

of the form for all integers n. Since x is in the interval -1 to $+1$, only finitely many n contribute ($n = 0$ to $n = 2s$ to be exact). We can rewrite the sum over n as a sum over (suggestively) $m := s - n$ and we get the answer (dropping overall constants)

$$\mathcal{Z}' = \sum_{m=-s}^{s} e^{-\beta H(m/s)}. \tag{5.10}$$

Eq. (5.10) looks very promising, but $H(m/s)$ is not the same as $\langle m|H|m\rangle$. First let us see where it *does* work. Take the simple Hamiltonian $H = S_z$, then $\langle \mathbf{n}|H|\mathbf{n}\rangle = s\cos\theta$, and thus $H(x) = sx$. This immediately yields

$$\mathcal{Z}'_{H=S_z} = \sum_{m=-s}^{s} e^{-\beta m}, \tag{5.11}$$

and it is easily calculated (in operator language) that $\mathcal{Z}'_{H=S_z} = \mathcal{Z}_{H=S_z}$. The two methods agree for the particular Hamiltonian $H = S_z$ (the case considered by Cabra *et al.* [199]). On the other hand, if we take $H = S_z^2$ and $s = 1$, we can evaluate $\langle \mathbf{n}|S_z^2|\mathbf{n}\rangle = \frac{1}{2}(\cos^2\theta + 1)$; from which we have

$$H(x) = \frac{1}{2}\left(x^2 + 1\right). \tag{5.12}$$

Thus, $\mathcal{Z}'_{H=S_z^2} = 2e^{-\beta} + e^{-\beta/2}$, but this conflicts with $\mathcal{Z}_{H=S_z^2} = 2e^{-\beta} + 1$ by more than just a multiplicative constant. Thus, we have $\mathcal{Z}'_{H=S_z^2} \neq \mathcal{Z}_{H=S_z^2}$ for $s = 1$, and in fact $\mathcal{Z}'_{H=S_z^2} \neq \mathcal{Z}_{H=S_z^2}$ for all $s > 1/2$.

Importantly, the two methods agree for any Hamiltonian when $s = 1/2$. This comes from the fact that any (diagonalized) Hamiltonian for a two state sytem ($s = 1/2$) can be written as $H = a + bS_z$ after an appropriate rotation (and, in fact, $S_z^2 = 1/4$), and the above method gives $\mathcal{Z}' = \mathcal{Z}$ when $H = a + bS_z$.

Further, say we have a Hamiltonian that is a polynomial of S_z/s (any finite-dimensional Hamiltonian, with an appropriate unitary transformation can be written in this way)

$$H = \sum_{i=1}^{N} a_i \left(\frac{S_z}{s}\right)^n . \tag{5.13}$$

First we note that

$$\langle m|H|m\rangle = E_m = \sum_{k=0}^{2s} a_k \left(\frac{m}{s}\right)^k .. \tag{5.14}$$

On the other hand,

$$H(m/s) = \langle \theta_m, \phi|H|\theta_m, \phi\rangle \,, \tag{5.15}$$

where θ_m is defined by $\cos\theta_m = m/s$ and this expression is independent of ϕ. Equivalently, we can write

$$H(m/s) = \langle s|e^{i\theta_m S_y} H e^{-i\theta_m S_y}|s\rangle \,.$$

The expression we are now interested in is

$$\begin{aligned}
\langle s|e^{i\theta_m S_y} H e^{-i\theta_m S_y}|s\rangle &= \sum_{k=0}^{N} a_k \frac{1}{s^k} \langle s|e^{i\theta_m S_y} S_z^k e^{-i\theta_m S_y}|s\rangle \\
&= \sum_{k=0}^{N} a_k \frac{1}{s^k} \langle s|(e^{i\theta_m S_y} S_z e^{-i\theta_m S_y})^k|s\rangle \\
&= \sum_{k=0}^{N} a_k \frac{1}{s^k} \langle s|[S_z m/s - S_x(1-m^2/s^2)^{1/2}]^k|s\rangle \,.
\end{aligned}$$

We can do a binomial expansion at this point, but we must note that if we have an odd amount of S_x's the expectation value will be zero (recall $S_x = (S_+ + S_-)/2$).

Thus, the first two terms in this expansion are

$$h_k := \frac{1}{s^k}\langle s|[S_z m/s - S_x(1-m^2/s^2)^{1/2}]^k|s\rangle = \frac{1}{s^k}\langle s|S_z^k m^k/s^k|s\rangle + \frac{1}{s^k}\left(\frac{m}{s}\right)^{k-2}\left(1-\frac{m^2}{s^2}\right)\sum_{n=0}^{k-2}\sum_{l=0}^{k-2-n}\langle s|S_z^l S_x S_z^n S_x S_z^{k-2-l-n}|s\rangle + \cdots . \quad (5.16)$$

Evaluating the right hand side of Eq. (5.16), we can write it as

$$\begin{aligned} h_k &= \left(\frac{m}{s}\right)^k + \frac{1}{s^{2+n}}\left(\frac{m}{s}\right)^{k-2}\left(1-\frac{m^2}{s^2}\right)\sum_{n=0}^{k-2}\sum_{l=0}^{k-2-n}\langle s|S_x S_z^n S_x|s\rangle + \cdots , \\ &= \left(\frac{m}{s}\right)^k + \frac{1}{2s}\left(\frac{m}{s}\right)^{k-2}\left(1-\frac{m^2}{s^2}\right)\sum_{n=0}^{k-2}(k-1-n)\left(1-\frac{1}{s}\right)^n + \cdots . \end{aligned}$$

Recall that $k \leq N$ so it does not grow with s, then the second term is clearly of the order $1/s$ and can be dropped for large enough spin s.

This method clearly works for H being any polynomial of S_z, and after that polynomial is set, taking $s \to \infty$ (or when the polynomial's degree is much smaller than two times the spin).

Putting this together with the conditions found

$$H(m/s) \sim \langle m|H|m\rangle + O(1/s).$$

This general result shows that "semiclassically" (i.e. s tends to infinity), we will still arrive at sensible results.

5.3 Breakdown of the harmonic-oscillator coherent state path integral

To motivate looking for this same issue in a system with the Weyl-Heisenberg algebra (i.e., the harmonic oscillator algebra), it is known [201] that one can contract

$\mathfrak{u}(2)$ (since we constructed our coherent states for spins with $\mathfrak{su}(2)$) into the Weyl-Heisenberg algebra by considering $\mathfrak{u}(2) = \text{span}\{S_0, S_x, S_y, S_z\} = \mathfrak{u}(1) \oplus \mathfrak{su}(2)$, where we define $[S_0, S_i] = 0$. Then define the operators $J_0 := S_0$, $J_{1,2}(\epsilon) := \epsilon S_{y,x}$, and $J_3(\epsilon) := S_0 + \epsilon^{-2} S_z$ to get the commutation relations $[J_3, J_{1,2}] = \mp i J_{2,1}$, $[J_1, J_2] = -i\epsilon^2 J_3 + i J_0$, and $[J_0, J_i] = 0$. If we let $\epsilon \to 0$, we recover exactly the Weyl-Heisenberg algebra: $\mathfrak{h}_4 = \text{span}\{1, x, p, a^\dagger a\}$ with $[x, p] = i$, $[a^\dagger a, x] = -ip$, $[a^\dagger a, p] = ix$. Intuitively, imagine the Bloch sphere that S_x, S_y, and S_z define with a radius s. As s grows, if we concentrate, say, on the south pole, it looks like a plane in phase-space[2]. This is what the contraction captures: It essentially goes to a tangent plane which asymptotically is exact as $s \to \infty$. Observe that S_z is related to $a^\dagger a$ in this contraction, so we might suspect that terms quadratic in $a^\dagger a$ give problems like those found with S_z^2 in the spin-coherent state path integral.

A Hamiltonian that uses the Weyl-Heisenberg algebra to construct its coherent states is the Bose-Hubbard model. For a single site, we can write

$$H = -\mu n + \frac{U}{2} n(n-1), \tag{5.17}$$

where $n = a^\dagger a$ and the a ($a^\dagger$) is the annihilation (creation) operator for the algebra $[a, a^\dagger] = 1$. The form $n(n-1) = a^\dagger a^\dagger a a$ comes from the normal ordering required from a path integral of the form

$$\mathcal{Z}' = \int \mathcal{D}^2 z \, \exp\left\{ -\int_0^\beta d\tau \left[\frac{1}{2}(z^* \dot{z} - \dot{z}^* z) - \mu |z|^2 + \frac{U}{2} |z|^4 \right] \right\}. \tag{5.18}$$

We can solve this path integral with the same method used to obtain Eq. (5.10) in

[2]Technically, the contraction is independent of the representation s defines, but in this large representation, it operates nearly identically.

the spin-coherent state path integral. Let $z = \sqrt{n}e^{i\theta}$, so that the measure becomes $\mathcal{D}^2 z = \mathcal{D}n\mathcal{D}\theta$ and the action becomes

$$S = \int d\tau (in\dot{\theta} - \mu n + \frac{U}{2}n^2). \tag{5.19}$$

Integrating by parts on the $n\dot{\theta}$ term then integrating over $\mathcal{D}\theta$ will fix n to be constant and give us a separation into different topological sectors (depending on how many times a path wraps around zero in phase-space), and the boundary term will fix n to be an integer. Since n is radial, it can only be positive so we directly obtain

$$\mathcal{Z}' = \sum_{n=0}^{\infty} e^{\mu n\beta - \frac{U}{2}n^2\beta}. \tag{5.20}$$

But this differs from the partition function that we can easily calculate in operator language:

$$\mathcal{Z} = \sum_{n=0}^{\infty} e^{\mu n\beta - \frac{U}{2}n(n-1)\beta}. \tag{5.21}$$

We see that a similar problem to that of the spin coherent state path integral here. To see it explicitly, for $U \gg 1$, we have $\mathcal{Z}' \sim 1 + e^{\mu - U/2} + \cdots$, but $\mathcal{Z} \sim 1 + e^{\mu} + e^{2\mu - U} + \cdots$. With different asymptotics, $\mathcal{Z}$ and $\mathcal{Z}'$ are different expressions. Note that if we let $\mu \to \mu + \frac{U}{2}$ in $\mathcal{Z}'$, that we will get same result. This substitution for μ corresponds to replacing n in Eq. (5.17) by $\langle n \rangle = |z|^2$ when writing down our action (so instead of $\langle n^2 \rangle$, one gets $\langle n \rangle^2$—just as in the case of S_z, fluctuations in the generators are getting in the way).

5.4 (Lack of) Relation to the semiclassical anomaly

As discussed in the introduction, others have identified problems in the coherent state path integral that are related to the semiclassics of the model. To get the correct result, an anomaly in the fluctuation determinant modifies the propagator in a non-trivial manner giving the correct result. This is usually discussed in the literature in context of the SU(2) coherent state path integrals, and here we do the calculation for the single-site Bose-Hubbard model as we have used in Sec. 5.3. However, as early as Berezin [140], it was recognized that the semiclassics of the coherent state path integral was correct if one used *Weyl-ordering* instead of *normal-ordering*. To be specific, if one has a complex function $H(z, z^*)$ in the Lagrangian of the coherent state path integral, the normal-ordering scheme defines $\langle z|H|z\rangle = H(z, z^*)$. This means that we can directly map

$$H = \sum_{nm} \alpha_{nm} (a^\dagger)^m a^n \implies \langle z|H|z\rangle = \sum_{nm} \alpha_{nm} (z^*)^m z^n, . \tag{5.22}$$

On the other hand, the Weyl symbol is defined such that

$$H = \sum_{nm} \alpha_{nm} [(a^\dagger)^m a^n]_S \implies H_W(z, z^*) = \sum_{nm} \alpha_{nm} (z^*)^m z^n, \tag{5.23}$$

where $[\cdots]_S$ represents the fully symmetric operator product (e.g. $[a^\dagger a]_S = (aa^\dagger + a^\dagger a)/2$). These two representations can be mapped into one another, such as [140]

$$\langle z|H|z\rangle = \int \frac{d^2v}{2\pi} H_W(v, v^*) e^{-\frac{1}{2}(z^* - v^*)(z - v)}. \tag{5.24}$$

However, the semiclassical picture actually tracks H_W instead of $\langle z|H|z\rangle$.

In order to do semiclassics, we need a small parameter. Still considering Eq. (5.17), let us change our algebra slightly to incorporate this small parameter (akin to the standard $\hbar \to \infty$ for normal semiclassics): h^{-1} such that $[a, a^\dagger] = h$. The quantity h^{-1} is the representation index (called γ in [155]). We note here that different h's change the coherent states $|z\rangle$ in the following way: if $z = \frac{1}{\sqrt{2}}(u + iv)$, then $u = q/c$, $v = p/d$, and $h = \hbar/(cd)$. We have used q and p as the standard position and momentum for the harmonic oscillator. Up until now we have been considering $h = 1$.

We first look at the Hamiltonian $H = \omega n/h$ where $n = a^\dagger a$. We first find the propagator between two coherent states. The propagator as defined by the path integral with the Lagrangian $L = iz^*\dot{z} - \langle z|H|z\rangle$ is then given by

$$\langle z_f|e^{-iHT}|z_i\rangle = e^{-\frac{1}{2h}(|z_f|^2+|z_i|^2)+\frac{1}{h}z_f^* z_i e^{-i\omega T}-\frac{1}{2}i\omega T}. \tag{5.25}$$

Let us try to prove this in the operator language, we can insert a complete set of states and obtain

$$\langle z_f|e^{-iHT}|z_i\rangle = \sum_n \langle z_f|n\rangle \langle n|z_i\rangle e^{-i\omega T n/h} \tag{5.26}$$

$$= e^{-\frac{1}{2h}(|z_f|^2+|z_i|^2)} \sum_n \left(\frac{1}{h} z_f^* z_i\right)^n \frac{1}{n!} e^{-i\omega T n} \tag{5.27}$$

$$= e^{-\frac{1}{2h}(|z_f|^2+|z_i|^2)+\frac{1}{h}z_f^* z_i e^{-i\omega T}}. \tag{5.28}$$

But we have that Eq. (5.28) is *not* the same as Eq. (5.25). However, if we use the Weyl-ordered version of the Hamiltonian though ($H_W = \omega(aa^\dagger + a^\dagger a)/(2h) = \omega n/h + \omega/2h$, then we would have a multiplicative constant term that would go as $e^{-\frac{i}{2}\omega T}$—in agreement with the path integral approach.

Now, we move to the more interesting case of the path integral for the single-site Bose-Hubbard model. We will be interested in the Lagrangian that has

$$H(z, z^*) = -\frac{\mu}{h}|z|^2 + \frac{U}{2h}|z|^4. \tag{5.29}$$

In the algebra described in the previous section, we can write our single-site Bose-Hubbard Hamiltonian as

$$H = -\frac{\mu}{h}n + \frac{U}{2h}n(n-h), \tag{5.30}$$

which if we consider normal ordering $\langle z|H|z\rangle = H(z, z^*)$. If we let $\tilde{\mu} := \mu + \frac{Uh}{2}$, then we can write

$$H = -\frac{\tilde{\mu}}{h}n + \frac{U}{2h}n^2. \tag{5.31}$$

We will be using this form of H throughout. The propagator looks like

$$K(z_f^*, z_i; T) = \langle z_f|e^{i\tilde{\mu}n\frac{T}{h} - \frac{i}{2}Un^2\frac{T}{h}}|z_i\rangle \tag{5.32}$$

Now, we want to decouple n^2, so we make use of the Hubbard-Stratonvich transformation

$$e^{-\frac{i}{2}Un^2\frac{T}{h}} = \sqrt{\frac{iT}{2\pi Uh}}\int d\omega\, e^{\frac{i}{2U}\omega^2\frac{T}{h} + ni\omega\frac{T}{h}}, \tag{5.33}$$

and this leads directly to an evaluation of the propagator which we can write now as

$$K(z_f^*, z_i; T) = \sqrt{\frac{iT}{2\pi Uh}}\int d\omega\, e^{\frac{i}{2Uh}\omega^2 T}\,\langle z_f|e^{i(\tilde{\mu}+\omega)n\frac{T}{h}}|z_i\rangle \tag{5.34}$$

$$= \sqrt{\frac{iT}{2\pi Uh}}\int d\omega\, e^{\frac{1}{h}z_f^* z_i e^{i(\omega+\tilde{\mu})T} - \frac{1}{2h}(|z_f|^2+|z_i|^2) + \frac{i}{2Uh}\omega^2 T}. \tag{5.35}$$

We will take the stationary phase approximation of this quantity later to obtain agreement with (or rather, disagreement with) the semiclassics given by the path integral.

If we change variables so that $\bar{\omega} + \mu = \omega + \tilde{\mu}$, we get

$$K(z_f^*, z_i; T) = \sqrt{\frac{iT}{2\pi U}} \int d\bar{\omega}\, e^{\frac{1}{h} z_f^* z_i e^{i(\bar{\omega}+\mu)T} - \frac{1}{2h}(|z_f|^2+|z_i|^2) + \frac{i}{2Uh}\bar{\omega}^2 T + \frac{i}{2}\bar{\omega}T + \frac{i}{8}UhT}. \quad (5.36)$$

On the other hand, we can Weyl order the Hamiltonian to get

$$H_W = -\frac{1}{2h}\mu\left(a^\dagger a + aa^\dagger\right) + \frac{U}{2h}\left[a^\dagger a^\dagger aa\right]_S \quad (5.37)$$

$$= -\frac{1}{h}\mu\left(n + \frac{h}{2}\right) + \frac{U}{2h}\left(n^2 + nh + \frac{h^2}{2}\right) \quad (5.38)$$

$$= -\frac{1}{h}\left(\mu - \frac{Uh}{2}\right)n + \frac{U}{2h}n^2 + \frac{Uh}{4} \quad (5.39)$$

In order to check the above propagator K with its analogue with the Weyl Hamiltonian K_W, we can use the previous result in Eq. (5.36) to find the result for this Weyl symmetric Hamiltonian

$$K_W(z_f^*, z_i; T) = \sqrt{\frac{iT}{2\pi U}} \int d\bar{\omega}\, e^{\frac{1}{h} z_f^* z_i e^{i(\bar{\omega}+\mu)T} - \frac{1}{2h}(|z_f|^2+|z_i|^2) + \frac{i}{2Uh}\bar{\omega}^2 T - \frac{i}{2}\bar{\omega}T - \frac{i}{8}UhT}. \quad (5.40)$$

In terms of the path integral we can write out

$$K(z_f^*, z_i; T) = \int_{z(0)=z_I}^{z^*(T)=z_f^*} \mathcal{D}^2 z\, \exp\left\{\Phi[z, z^*]/h\right\}, \quad (5.41)$$

where we have defined

$$\Phi = S + \Gamma, \quad (5.42)$$

$$\Gamma = \frac{1}{2}\left[z_f^* z(T) + z^*(0) z_I - |z_f|^2 - |z_I|^2\right], \quad (5.43)$$

$$S = \frac{1}{2}\int_0^T dt\,(z\dot{z}^* - z^*\dot{z}) - i\int_0^T dt\, hH(z, z^*), \quad (5.44)$$

and where $H(z, z^*)$ is defined by Eq. (5.29). We solve for the classical state by varying the action to get separate equations for z and z^*. These look like

$$\dot{z}_{\rm cl} = -ih\frac{\partial H}{\partial z^*_{\rm cl}} \qquad z_{\rm cl}(0) = z_i \tag{5.45}$$

$$\dot{z}^*_{\rm cl} = ih\frac{\partial H}{\partial z_{\rm cl}} \qquad z^*_{\rm cl}(T) = z_f. \tag{5.46}$$

This allows us to evaluate the semiclassical propagator to be

$$K_{\rm sc}(z_f, z_i; T) = \left[\frac{\partial^2 \Phi_{\rm cl}}{\partial z^*_f \partial z_i}\right]^{1/2} \exp\left\{\Phi_{\rm cl}/h + \frac{i}{2}\int_0^T B\, dt\right\}, \tag{5.47}$$

where $\Phi_{\rm cl} := \Phi[z_{\rm cl}, z^*_{\rm cl}]$ and

$$B = \left[h\frac{\partial^2 H}{\partial z \partial z^*}\right]_{z=z_{\rm cl}}. \tag{5.48}$$

With our specific Hamiltonian, the classical equations to be satisfied are

$$\dot{z}_{\rm cl} = -iz_{\rm cl}\left(-\mu + U|z_{\rm cl}|^2\right) = i(\mu+\omega)z_{\rm cl}, \tag{5.49}$$

$$\dot{z}^*_{\rm cl} = iz^*_{\rm cl}(-\mu + U|z_{\rm cl}|^2) = -i(\omega+\mu)z^*_{\rm cl}, \tag{5.50}$$

where we defined

$$\omega(z_{\rm cl}, z^*_{\rm cl}) = -U|z_{\rm cl}|^2, \tag{5.51}$$

and we can see that we get $\frac{d}{dt}\omega = 0$. This allows us to solve the equations (5.50) to get

$$z_{\rm cl}(t) = e^{i(\omega+\mu)t} z_i, \tag{5.52}$$

$$z^*_{\rm cl}(t) = e^{i(\omega+\mu)(T-t)} z^*_f. \tag{5.53}$$

And we get the consistency equation

$$\omega = -U z_f^* z_i e^{i(\omega+\mu)T}. \tag{5.54}$$

Now, we go about evaluating everything

$$\Phi_{\rm cl} = \int_0^T dt \left[-i(\omega+\mu)|z_{\rm cl}|^2 - i\left(-\mu|z_{\rm cl}|^2 + \frac{U}{2}|z_{\rm cl}|^4 \right) \right] \tag{5.55}$$

$$= \int_0^T dt \left[i(\omega+\mu)\frac{\omega}{U} - i\left(\mu\frac{\omega}{U} + \frac{U}{2}\frac{\omega^2}{U^2} \right) \right] \tag{5.56}$$

$$= \frac{iT}{2}\frac{\omega^2}{U} \tag{5.57}$$

$$\Gamma_{\rm cl} = z_f^* z_i e^{i(\omega+\mu)T} - \frac{1}{2}\left(|z_f|^2 + |z_i|^2 \right). \tag{5.58}$$

This allows us to write

$$\Phi_{\rm cl} = z_f^* z_i e^{i(\omega+\mu)T} + \frac{iT}{2U}\omega^2 - \frac{1}{2}\left(|z_f|^2 + |z_i|^2 \right). \tag{5.59}$$

Now, we define

$$\Phi_\omega = z_f^* z_i e^{i(\omega+\mu)T} + \frac{iT}{2U}\omega^2, \tag{5.60}$$

that independently depends on ω. We notice that

$$\frac{\partial \Phi_\omega}{\partial \omega} = 0, \tag{5.61}$$

in fact this is just the consistency equation Eq. (5.54). We now perform some partial differentiation

$$\frac{\partial^2 \Phi_{\rm cl}}{\partial z_f^* \partial z_i} = \frac{\partial}{\partial z_f^*}\left[\frac{\partial \Phi_\omega}{\partial z_i} + \frac{\partial \Phi_\omega}{\partial \omega}\frac{\partial \omega}{\partial z_i} \right] \tag{5.62}$$

$$= \frac{\partial^2 \Phi_\omega}{\partial z_f^* \partial z_i} + \frac{\partial^2 \Phi_\omega}{\partial \omega \partial z_i}\frac{\partial \omega}{\partial z_f^*} + \frac{\partial^2 \Phi_\omega}{\partial z_f^* \partial \omega}\frac{\partial \omega}{\partial z_i} + \frac{\partial^2 \Phi_\omega}{\partial \omega^2}\frac{\partial \omega}{\partial z_i}\frac{\partial \omega}{\partial z_f^*}. \tag{5.63}$$

Now Eq. (5.61) gives us that

$$\frac{\partial^2 \Phi_\omega}{\partial z_f^* \partial \omega} + \frac{\partial^2 \Phi_\omega}{\partial \omega^2} \frac{\partial \omega}{\partial z_f^*} = 0 \tag{5.64}$$

$$\frac{\partial^2 \Phi_\omega}{\partial z_i \partial \omega} + \frac{\partial^2 \Phi_\omega}{\partial \omega^2} \frac{\partial \omega}{\partial z_i} = 0. \tag{5.65}$$

Eq. (5.64) and Eq. (5.65) can be used to get rid of derivatives of ω in Eq. (5.63) and we get

$$\frac{\partial^2 \Phi_{\text{cl}}}{\partial z_f^* \partial z_i} = \frac{\partial^2 \Phi_\omega}{\partial z_f^* \partial z_i} - \frac{\partial^2 \Phi_\omega}{\partial \omega \partial z_i} \frac{\partial^2 \Phi_\omega}{\partial \omega \partial z_f^*} \left(\frac{\partial^2 \Phi_\omega}{\partial \omega^2} \right)^{-1}. \tag{5.66}$$

If we write out things we get

$$\frac{\partial^2 \Phi_\omega}{\partial z_f^* \partial z_i} = e^{i(\omega+\mu)T}, \tag{5.67}$$

$$\frac{\partial^2 \Phi_\omega}{\partial \omega \partial z_i} = iT z_f^* e^{i(\omega+\mu)T}, \tag{5.68}$$

$$\frac{\partial^2 \Phi_\omega}{\partial \omega \partial z_f^*} = iT z_i e^{i(\omega+\mu)T}, \tag{5.69}$$

$$\frac{\partial^2 \Phi_\omega}{\partial \omega^2} = \frac{iT}{U} - T^2 z_f^* z_i e^{i(\omega+\mu)T}. \tag{5.70}$$

Putting this together we get

$$\frac{\partial^2 \Phi_{\text{cl}}}{\partial z_f^* \partial z_i} = e^{i(\omega+\mu)T} + \frac{T^2 z_i z_f^* e^{2i(\omega+\mu)T}}{iT/U - T^2 z_f^* z_i e^{i(\omega+\mu)T}} \tag{5.71}$$

$$= \frac{iT e^{i(\omega+\mu)T}/U}{iT/U - T^2 z_f^* z_i e^{i(\omega+\mu)T}} \tag{5.72}$$

$$= \left(\frac{iT}{U} \right) \left(\frac{\partial^2 \Phi_\omega}{\partial \omega^2} \right)^{-1} e^{i(\omega+\mu)T}. \tag{5.73}$$

Thus we have

$$\left[\frac{\partial^2 \Phi_{\text{cl}}}{\partial z_f^* \partial z_i} \right]^{1/2} = \left(\frac{iT}{hU} \right)^{1/2} \left(\frac{1}{h} \frac{\partial^2 \Phi_\omega}{\partial \omega^2} \right)^{-1/2} e^{\frac{i}{2}(\omega+\mu)T}. \tag{5.74}$$

And lastly,

$$B = -\mu + 2U|z_{\rm cl}|^2 = -(\mu + 2\omega), \tag{5.75}$$

so that

$$\frac{i}{2}\int_0^T B\, dt = -\frac{i}{2}T(\mu + 2\omega). \tag{5.76}$$

Finally, we have the full semiclassical operator (summing over ω, solutions to the consistency equation (5.54))

$$K_{\rm sc}(z_f^*, z_i; T) = \sum_\omega \left(\frac{iT}{hU}\right)^{1/2} \left(\frac{1}{h}\frac{\partial^2 \Phi_{\rm cl}}{\partial \omega^2}\right)^{-1/2} \exp\left[\frac{1}{h}\Phi_{\rm cl} + \frac{i}{2}(\omega + \mu)T - i\Delta\right], \tag{5.77}$$

$$= \sum_\omega \left(\frac{iT}{hU}\right)^{1/2} \left(\frac{1}{h}\frac{\partial^2 \Phi_{\rm cl}}{\partial \omega^2}\right)^{-1/2} \exp\left[\frac{1}{h}\Phi_{\rm cl} - \frac{i}{2}\omega T\right], \tag{5.78}$$

where

$$i\Delta = \frac{i}{2}(\mu + 2\omega)T, \tag{5.79}$$

and the sum is over solutions to the consistency equation $\partial_\omega \Phi_\omega = 0$. The Δ term comes from the anomaly in the fluctuation determinant and as evaluated by Kochetov [155]. Notice that this coincides with Eq. (5.40) when we take the steepest descent of the $\bar{\omega}$ integral as $h \to 0$. Thus, we see that the path integral is giving a result inconsistent with normal ordering and consistent with Weyl ordering. This speaks to the fact that we lose operator order when going to the path integral [202].

However, let us see if this was actually the problem with the coherent state path integral as we had evaluated before. Recall Eq. (5.20) and Eq. (5.21) define $\mathcal{Z}$

and $\mathcal{Z}'$ (exact Hamiltonian and path integral respectively). Now if $\mathcal{Z}_W$ represents the exact partition function as given by the Weyl ordering, we obtain

$$\mathcal{Z}_W = \sum_n e^{\beta\mu n - \beta\frac{U}{2}(n^2+n+1/2)+\beta\mu/2} \sim e^{\beta(U+\mu)/2}(1 + e^{\beta(\mu-U)} + \cdots). \tag{5.80}$$

We see from this that $\mathcal{Z} \neq \mathcal{Z}' \neq \mathcal{Z}_W$. This solution, as it exists for the semiclassical analysis, does not apply to the calculational procedure we used for the exact calculation found in Sec. 5.3.

5.5 Conclusions

While the semiclassical result is not a new one, it shows that the path integral is not dealing with the same Hamiltonian. Unfortunately, our exact calculation of $\mathcal{Z}'$ (see Eq. (5.61)) suggests that the path integral is dealing with $H' = -\mu n + \frac{U}{2}n^2$ while semiclassics suggests it is dealing with $H_W = -\mu n + \frac{U}{2}n(n+1)$ (going back to $h = 1$). These two methods differ but both are not dealing with the Hamiltonian under consideration, Eq. (5.30). In the case of the Weyl ordered Hamiltonian, we can write our original Hamiltonian in Eq. (5.30) as $H = H_W - Un$ which is Weyl ordered (up to a constant). This ordering can be used to modify the path integral by an extra term: $-U|z|^2$. This correction to the path integral suggested by Weyl ordering does not fix the exact calculation of $\mathcal{Z}'$ as can be easily shown, but it does motivate an *ad hoc* correction to the path integral to "fix" our exact calculation. We use the following action:

$$S = \int dt \left(-\mu|z|^2 + \frac{U}{2}|z|^2(|z|^2 - 1) \right). \tag{5.81}$$

This action is constructed by just changing the operator n to a function $|z|^2$; while this gives correct results with the method which gives Eq. (5.20), there is no *a priori* reason to suspect this of being the action. Similarly, if in the spin-coherent state path integral, we replace the operator S_z with its expectation value $\langle \mathbf{n}|S_z|\mathbf{n}\rangle$ everywhere, we will get the correct result. This means, in particular, for $H = S_z^2$ that instead of $\langle S_z^2\rangle$ in the spin-path integral we have $\langle S_z\rangle^2$. In general, if one substitutes the generators of the coherent states in the Hamiltonian with their expectation value, one obtains the correct result for $\mathcal{Z}$ with the methods used to derive Eq. (5.54) and Eq. (5.61).

Corrections aside, a simple way to see what has gone wrong is to return to Eq. (5.12). This $H(x)$ function can not achieve the value 0, but $H = S_z^2$ clearly has such an eigenvalue. This is due to the fact that for higher dimensional representations of SU(2) not every eigenvector of S_z can be rotated into another with a standard SU(2) rotation. On the other hand, the coherent states we used are a complete set for even higher dimensional representations, so in principle, we should not lose any information about the $m = 0$ state. Continuity in $\mathbf{n}$ seems to be the culprit: $H(x)$ came from a time discretized form (between time slices j and $j+1$) $\langle \mathbf{n}_{j+1}|S_z^2|\mathbf{n}_j\rangle$, and we have $\langle \mathbf{n}|S_z^2|-\mathbf{n}\rangle = 0$, so $\langle \mathbf{n}_{j+1}|S_z^2|\mathbf{n}_j\rangle$ can attain zero, but not for any paths that are "close" to each other (i.e. $\mathbf{n}_j \approx \mathbf{n}_{j+1}$) as the continuous time path integral assumes. As such, the discrete time path integral (before a continuity assumption is imposed) can unambiguously give the correct results to a calculation.

To conclude, in the time-continuous formulation of the path integral, neither the action suggested by Weyl-ordering nor the action constructed by normal ordering

gives correct results when evaluating $\mathcal{Z}$ via path integrals.

Chapter 6: Conclusion

In this dissertation, we have largely been concerned with how electromagnetic phenomena are modified due to materials considered to be topological (Chapters 2 and 4) or undergoing a topological transition (a Lifshitz transition, Sec. 3.2). Along the way, we investigated the question of how to test diffusive models of metals in the Casimir effect theoretically and experimentally (Sec. 3.3), and we looked into the breakdown of the coherent state path integral (Chapter 5).

The main effects considered here considered both the classical and quantum aspects of the electromagnetic field. The classical electromagnetic field experiences magneto-optical effects captured by the Faraday and Kerr rotations, and those see a dependence on the optical conductivity of a material—which can be a proxy for many interesting effects such as AQHE and resonant structure of impurities or excitons, as Chapter 2 discusses. For thin film TIs at finite frequencies, the Kerr and Faraday rotations differ from their low frequency, universal behavior due to other material phenomena. We added to this picture of finite frequency optical experiments on thin film TIs, captured in Fig. 2.1, by including the resonant behavior of localized impurity states.

The quantum electromagnetic field has virtual vacuum fluctuations of pho-

tons that cause a force between materials. Using one object as a probe, one can look for interesting material phenomenon like those considered in Chapter 3. The band structure can experience a topological phase transition known as a Lifshitz transition, causing a "kink" in the optical conductivity that translates directly to a "kink" in the Casimir force as we found in Fig. 3.2 which could be measured. Additionally, we shed light on the problem in the Casimir community of how to model the low frequency behavior of a material: with a diffusive model (Drude) or a ballistic model (Plasma). In this vein, we proposed an experiment to use an effect, namely weak localization, to see a qualitative change in the Casimir effect if and only if the electronic model the Casimir effect is accessing is diffusive (as it should be in the metals under consideration). The results for how a diffusive model changes the Casimir effect are captured in Fig. 3.7, where magnetic field tunes this weak localization effect. Instead of the usual numerical differences in models, this would get at the effect in a profound way. Theoretically, we also checked to see if the approximation of disorder averaging our linear response instead of the Casimir energy itself was accurate, and found that in the parameter ranges usually under consideration, it is fine provided the plates are not closer to each other than roughly $c/v_{\mathrm{F}} \times \ell_{\mathrm{MF}}$ where ℓ_{MF} is the mean free path of electrons in the disordered material (a photon should not travel between the plates many times before an electron done scattering).

In search of materials that could experience a Casimir repulsion, we turn to Weyl semimetals in Chapter 4 and their peculiar electromagnetic properties. Beginning with idealized case of semi-infinite and thick Weyl plates characterized

solely by a low-energy axionic action Eq. (4.1), we find that a region of repulsion that can be increased for smaller thicknesses (see Fig. 4.4). We then determine how the actual low-energy band structure could modify these results by calculating the optical conductivity in Eq. (4.53) and then modifying parameters to see how the Casimir effect changes. Repulsion is replaced with attraction at shorter distances scales, but survives at larger scaled, see Figs. 4.6 and 4.5. Even the inclusion of a technically infinite DC conductivity by means of a finite chemical potential does not entirely destroy this intermediate repulsive region as Fig. 4.7 demonstrates.

Finally, in Chapter 5 we discussed how a particular exact method for calculating the path integral exposes a breakdown that does not fit into the usual known schemes that correct for such problems. The problem seems to be connected to continuity of paths, since calculational methods used prior to this assumption seem to produce correct results. Curiously, if the Hamiltonian used to generate the path integral is linear in the generators of the Lie algebra with which the coherent states are formed, the procedure goes through smoothly and gives the correct result.

The electromagnetic force—the fundamental force responsible for nearly all condensed matter phenomenon—and topology are important to probing, classifying, and discovering new materials. The realization of topology in band structure gives interesting novel physical phenomena, and the use of direct electromagnetic phenomena in optics and Casimir experiments, as we have considered here, can very powerfully probe material properties resulting from this topology.

Appendix A: Optical reflection from a suspended thin film

In this appendix we consider the reflection and transmission of an electromagnetic wave incident on a thin-film material characterized by conductance $\sigma_{\mu\nu}(\omega)$. Similar calculations have been previously done [109]; we provide this here for completeness—especially when connecting the classical electrodynamcs to the RPA from quantum field theory in Eqs. (1.9) and Eqs. (1.10).

To begin say we have a thin film at $z = 0$ characterized by $\sigma_{\mu\nu}(\omega)$ such that $\mathbf{J}(\mathbf{x}, \omega) = \boldsymbol{\sigma}(\omega) \cdot \mathbf{E}(x, \omega)\, \delta(z)$. Taking continuity into account, if we Fourier transform in position space, we have, by the continuity equation (defining $\mathbf{k}_\parallel = (k_x, k_y)$)

$$\rho = \frac{\mathbf{k}_\parallel}{\omega} \cdot \boldsymbol{\sigma} \cdot \mathbf{E}. \tag{A.1}$$

Consider an incident plane wave in $z < 0$: $\mathbf{E}_0 e^{i\mathbf{k}\cdot\mathbf{x} - i\omega t}$, the reflected wave $\mathbf{E}_r e^{i\mathbf{k}_r\cdot\mathbf{x} - i\omega t}$ with $\mathbf{k}_r = (k_x, k_y, -k_z)$, and transmitted wave $\mathbf{E}_t e^{i\mathbf{k}\cdot\mathbf{x} - i\omega t}$. Then, the relevant Maxwell equations are

$$\nabla \cdot \mathbf{E} = \rho, \tag{A.2}$$

$$\nabla \times \mathbf{B} = \frac{1}{c}\frac{\partial \mathbf{E}}{\partial t} + \frac{1}{c}\boldsymbol{\sigma} \cdot \mathbf{E}\, \delta(z). \tag{A.3}$$

$$\nabla \times \mathbf{E} = -\frac{1}{c}\partial_t \mathbf{B} \tag{A.4}$$

By $\nabla \times \mathbf{E} = -\frac{1}{c}\partial_t \mathbf{B}$, we know that the parallel component of $\mathbf{E}$ is parallel across

the film, or

$$\hat{\mathbf{z}} \times (\mathbf{E}_0 + \mathbf{E}_r - \mathbf{E}_t) = 0. \tag{A.5}$$

Now, we can take Eq. (A.3), and integrate around a closed contour illustrated in to get

$$\begin{aligned} \mathbf{e}_1 \cdot (\mathbf{B}_0 + \mathbf{B}_r - \mathbf{B}_t) &= \frac{1}{c}(\mathbf{e}_1 \times \hat{\mathbf{z}}) \cdot \boldsymbol{\sigma} \cdot \mathbf{E} \\ &= \frac{1}{c}\mathbf{e}_1 \cdot (\hat{\mathbf{z}} \times \boldsymbol{\sigma} \cdot \mathbf{E}). \end{aligned}$$

This is true for any $\mathbf{e}_1$ perpendicular to $\hat{\mathbf{z}}$, so we can just write our equations to be solved as

$$\hat{\mathbf{z}} \times (\mathbf{k} \times \mathbf{E}_0 + \mathbf{k}_r \times \mathbf{E}_r - \mathbf{k} \times \mathbf{E}_t) = -\frac{\omega}{c}\boldsymbol{\sigma} \cdot \mathbf{E}_t, \tag{A.6}$$

$$\hat{\mathbf{z}} \times (\mathbf{E}_0 + \mathbf{E}_r - \mathbf{E}_t) = 0. \tag{A.7}$$

If we satisfy these, then Eq. (A.2) will be automatically satisfied across the boundary. At this point, we specify the components: transverse electric and transverse magnetic (depending on whether the electric or magnetic field, respectively, is perpendicular to the plane of incidence).

Without loss of generality, assume $\hat{\mathbf{y}}$ is perpendicular to the plane of incidence so that $\hat{\mathbf{y}} \cdot \mathbf{k} = 0$, $\mathbf{E}_0 = E_0^{\mathrm{TM}}\mathbf{k} \times \hat{\mathbf{y}}/k + E_0^{\mathrm{TE}}\hat{\mathbf{y}}$ (similarly for $\mathbf{E}_t$), and $\mathbf{E}_r^{\mathrm{TM}}\mathbf{k} \times \hat{\mathbf{y}}/k - E_r^{\mathrm{TE}}\hat{\mathbf{y}}$.

Solving these linear equations is quite simple. Remembering our designation of the x-direction in the plane of incidence, and y-direction perpendicular (transverse),

we have

$$\boldsymbol{\sigma} = \begin{pmatrix} \sigma_{xx} & \sigma_{xy} \\ \\ \sigma_{yx} & \sigma_{yy} \end{pmatrix} \tag{A.8}$$

in general. This leads to the reflection matrix that connects

$$\begin{pmatrix} E_r^{\mathrm{TM}} \\ \\ E_r^{\mathrm{TE}} \end{pmatrix} = R(\omega, \mathbf{k}) \begin{pmatrix} E_r^{\mathrm{TM}} \\ \\ E_r^{\mathrm{TE}} \end{pmatrix}, \tag{A.9}$$

and the transmission matrix

$$\begin{pmatrix} E_t^{\mathrm{TM}} \\ \\ E_t^{\mathrm{TE}} \end{pmatrix} = T(\omega, \mathbf{k}) \begin{pmatrix} E_r^{\mathrm{TM}} \\ \\ E_r^{\mathrm{TE}} \end{pmatrix}. \tag{A.10}$$

Appropriately defined, the resulting matrices are

$$R(\omega, \mathbf{k}) = \frac{1}{D} \begin{pmatrix} \frac{ck_z}{\omega}\frac{\sigma_{xx}}{2c} + \det\frac{\boldsymbol{\sigma}}{2c} & -\frac{\sigma_{xy}}{2c} \\ \\ -\frac{\sigma_{yx}}{2c} & \frac{\omega}{ck_z}\frac{\sigma_{yy}}{2c} + \det\frac{\boldsymbol{\sigma}}{2c} \end{pmatrix}, \tag{A.11}$$

$$T(\omega, \mathbf{k}) = \frac{1}{D} \begin{pmatrix} 1 + \frac{\omega}{ck_z}\frac{\sigma_{yy}}{2c} & \frac{\sigma_{xy}}{2c} \\ \\ \frac{\sigma_{yx}}{2c} & 1 + \frac{ck_z}{\omega}\frac{\sigma_{xx}}{2c} \end{pmatrix}, \tag{A.12}$$

where

$$D = 1 + \frac{ck_z}{\omega}\frac{\sigma_{xx}}{2c} + \frac{\omega}{ck_z}\frac{\sigma_{yy}}{2c} + \det\frac{\boldsymbol{\sigma}}{2c}. \tag{A.13}$$

These coefficients can be used for optical (Faraday and Kerr effects) and Casimir calculations (with the Lifshitz formula Eq. (1.8)).

Appendix B: Long distance behavior of the Casimir force

For the thin film geometry, we can easily analyze the long distance behavior of the Casimir force. To see this we look at Eq. (A.11). Rotating to imaginary frequencies $\omega \to i\omega$ and $k_z \to iq_z$ leaves things relatively unchanged. Now, we expect $\omega \sim O(cq_z)$ and photons between the plates will have $q_z \sim c/a$. Thus, large distances correspond to small frenquency/wavenumber (as compared to the length scales inherent in $\sigma_{\mu\nu}$). To see this, look at the Lifshitz formula Eq. (1.8), rewritten by changing variables to $q_z^2 = \omega^2 + k^2$.

$$E_c(a) = \hbar \int_0^\infty \frac{q_z\, dq_z}{(2\pi)^2} \int_0^{cq_z} \frac{d\omega}{2\pi}\ \mathrm{tr}\log[\mathbb{I} - R^2(\omega, q_z)e^{-2q_z a}]. \tag{B.1}$$

If we change variables to $x = \omega/cq_z$ and $u = 2q_z a$, then we obtain

$$E_c(a) = \frac{\hbar c}{(2a)^3} \int_0^\infty \frac{u^2\, du}{(2\pi)^2} \int_0^1 \frac{dx}{2\pi}\ \mathrm{tr}\log\left[\mathbb{I} - R^2\left(\tfrac{cux}{2a}, \tfrac{u}{2a}\right) e^{-u}\right]. \tag{B.2}$$

The exponential keeps $u \sim O(1)$ while clearly $x \sim O(1)$. Thus, when a is large compared to the length scales in $R(\omega, q_z)$, we can expand $R^2(\omega, q_z)$ in this expression and clearly $\omega = q_z = 0$ is the very far limit ($a \to \infty$) of this expression.

Thus, we consider two limiting cases that are relevant to the text. To simplify things we take the case $\sigma_{xx} = \sigma_{yy}$ and $\sigma_{xy} = -\sigma_{yx}$.

Case 1 (*Diamagnetic response*):

$$\frac{\sigma_{xx}}{c} = \frac{\omega_{\rm p}}{\omega} + O(\omega^0), \qquad\qquad \frac{\sigma_{xy}}{c} = O(\omega^0). \tag{B.3}$$

A pure system has a diamagnetic response which in a dirty system translates to a Drude peak in the optics and finite conductivity. This response has this $1/\omega$ behavior which for photons that go as c/a, will be quite large. The origin of this might be understood with a free electron system where (at imaginary frequencies)

$$\sigma_{xx}^{\rm bulk} = \frac{ne^2}{m}\frac{1}{\omega}, \tag{B.4}$$

where n is the three-dimensional density of electrons, m is their mass, and e is their charge. As a thin film, we might just naively integrate this over the bulk for simplicity to obtain

$$\frac{\sigma_{xx}}{c} = \frac{ne^2 d}{mc}\frac{1}{\omega}. \tag{B.5}$$

Thus, $\omega_{\rm p} = \frac{ne^2 d}{mc}$. As an aside, this takes the form $\omega_{\rm p} = 2nd\lambda v_f \alpha$ where λ is the de-Broglie wavelength of the electrons, v_f their Fermi velocity, and α is the fine-structure constant.

At large distances ($a \gg c/\omega_{\rm p}$), this will dominate the reflection matrix leaving us solely with

$$R(\omega, q_z) = \frac{1}{\frac{cq_z}{2\omega}\frac{\omega_{\rm p}}{\omega} + \frac{\omega}{2ck_z}\frac{\omega_{\rm p}}{\omega} + \frac{\omega_{\rm p}^2}{4\omega^2}} \begin{pmatrix} \frac{ckz}{2\omega}\frac{\omega_{\rm p}}{\omega} + \frac{1}{4}\left(\frac{\omega_{\rm p}}{\omega}\right)^2 & 0 \\ 0 & \frac{\omega}{2ck_z}\frac{\omega_{\rm p}}{\omega} + \frac{1}{4}\left(\frac{\omega_{\rm p}}{\omega}\right)^2 \end{pmatrix} \tag{B.6}$$

At low frequencies, this has the expansion

$$R(\omega, q_z) \sim \mathbb{I} - 2\frac{\omega}{\omega_{\rm p}} \begin{pmatrix} \frac{\omega}{cq_z} & 0 \\ 0 & \frac{cq_z}{\omega} \end{pmatrix}. \tag{B.7}$$

The relevant expression for the Lifshitz formula is then

$$R^2\left(\tfrac{cux}{2a},\frac{u}{2a}\right)\sim\mathbb{I}-2\frac{cu}{a\omega_{\rm p}}\begin{pmatrix}x^2 & 0\\ 0 & 1\end{pmatrix}. \tag{B.8}$$

The rest is just expansion of the Lifshitz integrand

$$\operatorname{tr}\log\left[\mathbb{I}-R^2\left(\tfrac{cux}{2a},\tfrac{u}{2a}\right)e^{-u}\right]\sim 2\log\left[1-e^{-u}\right]-2\frac{cu}{a\omega_{\rm p}}\frac{x^2+1}{1-e^u}. \tag{B.9}$$

Integrating over x leaves us with

$$\int_0^1 dx\operatorname{tr}\log\left[\mathbb{I}-R^2\left(\tfrac{cux}{2a},\tfrac{u}{2a}\right)e^{-u}\right]\sim 2\log\left[1-e^{-u}\right]-2\frac{cu}{a\omega_{\rm p}}\frac{4/3}{1-e^u}. \tag{B.10}$$

As can be easily verified, we know that

$$\int_0^\infty du\,u^2\log[1-e^{-u}]=\frac{1}{3}\int_0^\infty du\,\frac{u^3}{1-e^u}=-\frac{\pi^4}{45}. \tag{B.11}$$

Thus, we can immediately write down the Casimir energy

$$E_c=-\frac{\hbar c\pi}{1440a^3}\left(1-\frac{4c}{a\omega_{\rm p}}+\cdots\right). \tag{B.12}$$

Recall that $E_0=-\frac{\hbar c\pi}{1440a^3}$ is the Casimir energy for ideal conductors. And for all relevant scales, this energy represents an attractive force.

Case 2 (*Hall response*):

$$\sigma_{xx}(\omega)=o(\omega^0),\qquad\qquad \sigma_{xy}(\omega)=\sigma_{xy}+o(\omega^0). \tag{B.13}$$

In this case, we have assumed $\sigma_{xx}(\omega=0)=0$, and as a result, at large distances the reflection matrix takes the simple form

$$R(\tfrac{cux}{2a},\tfrac{u}{2a})\to\frac{1}{1+\frac{\sigma_{xy}^2}{4c^2}}\begin{pmatrix}\frac{\sigma_{xy}^2}{4c^2} & -\frac{\sigma_{xy}}{2c}\\ \frac{\sigma_{xy}}{2c} & \frac{\sigma_{xy}^2}{4c^2}\end{pmatrix},\qquad\qquad \text{as } a\to\infty. \tag{B.14}$$

The integral involving this matrix is done in a straightforward manner using the integral identity

$$\mathrm{Li}_4(\lambda) = -\frac{1}{2}\int_0^\infty du\, u^2 \log[1-\lambda e^{-u}], \tag{B.15}$$

we then just need the eigenvalues of R, which are $\sigma_{xy}/(\sigma_{xy} \pm 2ic)$. Thus,

$$E_c(a) = E_0 \frac{45}{\pi^4} \,\mathrm{Re}\left\{ \mathrm{Li}_4 \left[\left(\frac{\sigma_{xy}}{\sigma_{xy}+2ic} \right)^2 \right] \right\}, \tag{B.16}$$

where $E_0(a) = -\frac{\hbar c \pi}{1440 a^3}$ as we have defined previously. This behavior is the long-distance behavior as we have described the conductivities. If we further assume $\sigma_{xy}/c \ll 1$, we get

$$E_c(a) \sim -E_0 \frac{45}{4\pi^4} \left(\frac{\sigma_{xy}}{c} \right)^2. \tag{B.17}$$

Notice that this is a repulsive force (not because it is positive, but because it has a negative slope). It remains repulsive until roughly $\sigma_{xy}/2c \approx 1$. The force plot can be seen in Fig. 4.3.

Bibliography

[1] D. K. Efimkin and Y. E. Lozovik, "Resonant manifestations of chiral excitons in Faraday and Kerr effects in a topological insulator film," Phys. Rev. B **87**, 245416 (2013).

[2] H. B. G. Casimir, "On the Attraction Between Two Perfectly Conducting Plates," Proc. K. Ned. Akad. Wet. **51**, 793 (1948).

[3] J. H. Wilson, D. K. Efimkin, and V. M. Galitski, "Resonant faraday and kerr effects due to in-gap states on the surface of a topological insulator," Phys. Rev. B **90**, 205432 (2014).

[4] A. A. Allocca, J. H. Wilson, and V. Galitski, "Nonanalytic behavior of the Casimir force across a Lifshitz transition in a spin-orbit-coupled material," Phys. Rev. B **90**, 075420 (2014).

[5] A. A. Allocca, J. H. Wilson, and V. M. Galitski, "Quantum interference phenomena in the Casimir effect," `arXiv:1501.06096`.

[6] J. H. Wilson, A. A. Allocca, and V. M. Galitski, "Repulsive casimir force between weyl semimetals," `arXiv:1501.07659`.

[7] J. H. Wilson and V. Galitski, "Breakdown of the coherent state path integral: Two simple examples," Phys. Rev. Lett. **106**, 110401 (2011).

[8] X.-L. Qi and S.-C. Zhang, "Topological insulators and superconductors," Rev. Mod. Phys. **83**, 1057–1110 (2011).

[9] P. Hosur and X. Qi, "Recent developments in transport phenomena in Weyl semimetals," C. R. Phys. **14**, 857–870 (2013).

[10] R. Kubo, "Statistical-mechanical theory of irreversible processes. I. general theory and simple applications to magnetic and conduction problems," J. Phys. Soc. Jpn. **12**, 570–586 (1957), arXiv:0211006 [cs] .

[11] M. Faraday and F. James, *The Correspondence of Michael Faraday, Volume 3: 1841-1848*, The Correspondence of Michael Faraday (Institution of Engineering and Technology, 1996).

[12] G. Fowles, *Introduction to Modern Optics*, Dover Books on Physics Series (Dover Publications, 1975).

[13] S. Longair, *High Energy Astrophysics: Stars, the galaxy and the interstellar medium*, High Energy Astrophysics No. v. 2 (Cambridge University Press, 1994).

[14] J. Titheridge, "Determination of ionospheric electron content from the faraday rotation of geostationary satellite signals," Planet. Space Sci. **20**, 353 – 369 (1972).

[15] J. S. Blakemore, "Semiconducting and other major properties of gallium arsenide," J. Appl. Phys. **53**, R123–R181 (1982).

[16] D. Macaluso and O. M. Corbino, "On a new effect on light traversing certain metallic vapors in a magnetic field," C. R. Acad. Sci. **127**, 548 (1898).

[17] J. Kerr, "On rotation of the plane of polarization by reflection from the pole of a magnet," Philosophical Magazine Series 5 **3**, 321 (1877).

[18] A. B. Sushkov, G. S. Jenkins, D. C. Schmadel, N. P. Butch, J. Paglione, and H. D. Drew, "Far-infrared cyclotron resonance and Faraday effect in Bi_2Se_3," Phys. Rev. B **82**, 125110 (2010).

[19] G. S. Jenkins, A. B. Sushkov, D. C. Schmadel, N. P. Butch, P. Syers, J. Paglione, and H. D. Drew, "Terahertz Kerr and reflectivity measurements on the topological insulator Bi_2Se_3," Phys. Rev. B **82**, 125120 (2010).

[20] Y. Wang, A. Chubukov, and R. Nandkishore, "Polar Kerr effect from chiral-nematic charge order," Phys. Rev. B **90**, 205130 (2014).

[21] H. Weyl, "Das asymptotische Verteilungsgesetz der Eigenwerte linearer partieller Differentialgleichungen (mit einer Anwendung auf die Theorie der Hohlraumstrahlung)," Mathematische Annalen **71**, 441–479 (1912).

[22] R. Balian and C. Bloch, "Distribution of eigenfrequencies for the wave equation in a finite domain. I. Three-dimensional problem with smooth boundary surface," (1970).

[23] M. Bordag, U. Mohideen, and V. M. Mostepanenko, "New developments in the Casimir effect," Phys. Rep. **353**, 1–205 (2001).

[24] T. Emig, N. Graham, R. L. Jaffe, and M. Kardar, "Casimir forces between arbitrary compact objects," Phys. Rev. Lett. **99**, 170403 (2007).

[25] E. M. Lifshitz, "The theory of molecular attractive forces between solids," Sov. Phys. JETP **2**, 73 (1956).

[26] I. E. Dzyaloshinskii, E. M. Lifshitz, and L. P. Pitaevskii, "General Theory of Van der Waals' Forces," Sov. Phys. Usp. **4**, 153–176 (1961).

[27] O. Kenneth and I. Klich, "Opposites attract: A theorem about the Casimir force," Phys. Rev. Lett. **97**, 160401 (2006).

[28] T. H. Boyer, "Van der Waals forces and zero-point energy for dielectric and permeable materials," Phys. Rev. A **9**, 2078–2084 (1974).

[29] O. Kenneth, I. Klich, A. Mann, and M. Revzen, "Repulsive Casimir forces." Phys. Rev. Lett. **89**, 033001 (2002).

[30] J. N. Munday, F. Capasso, and V. A. Parsegian, "Measured long-range repulsive Casimir-Lifshitz forces." Nature **457**, 170–173 (2009).

[31] U. Leonhardt and T. G. Philbin, "Quantum levitation by left-handed metamaterials," New J. Phys. **9**, 254 (2007).

[32] R. Zhao, J. Zhou, T. Koschny, E. N. Economou, and C. M. Soukoulis, "Repulsive casimir force in chiral metamaterials," Phys. Rev. Lett. **103**, 103602 (2009).

[33] F. S. S. Rosa, "On the possibility of Casimir repulsion using Metamaterials," J. Physics Conf. Series **161**, 012039 (2009).

[34] T. H. Boyer, "Quantum electromagnetic zero-point energy of a conducting spherical shell and the Casimir model for a charged particle," Phys. Rev. **174**, 1764–1776 (1968).

[35] S. A. Fulling, L. Kaplan, and J. H. Wilson, "Vacuum energy and repulsive Casimir forces in quantum star graphs," Phys. Rev. A **76**, 012118 (2007).

[36] M. Levin, A. P. McCauley, A. W. Rodriguez, M. T. H. Reid, and S. G. Johnson, "Casimir repulsion between metallic objects in vacuum," Phys. Rev. Lett. **105**, 090403 (2010).

[37] A. G. Grushin and A. Cortijo, "Tunable casimir repulsion with three-dimensional topological insulators," Phys. Rev. Lett. **106**, 020403 (2011).

[38] W. K. Tse and A. H. MacDonald, "Quantized Casimir force," Phys. Rev. Lett. **109**, 236806 (2012).

[39] P. Rodriguez-Lopez and A. G. Grushin, "Repulsive Casimir effect with Chern insulators," Phys. Rev. Lett. **112**, 056804 (2014).

[40] G. L. Klimchitskaya, U. Mohideen, and V. M. Mostepanenko, "The Casimir force between real materials: Experiment and theory," Rev. Mod. Phys. **81**, 1827–1885 (2009).

[41] K. A. Milton, *The Casimir Effect*, Physical Manifestations of Zero-point energy (World Scientific, 2001).

[42] S. K. Lamoreaux, "Demonstration of the Casimir Force in the 0. 6 to 6 μm Range," Phys. Rev. Lett. **78**, 5–8 (1997).

[43] K. A. Milton, "Recent Developments in the Casimir Effect," J. Phys. Conf. Series **161**, 012001 (2009), 0806.2880 .

[44] M. Sparnaay, "Attractive forces between flat plates," Nature **180**, 334–335 (1957).

[45] M. Sparnaay, "Measurements of attractive forces between flat plates," Physica **24**, 751–764 (1958).

[46] S. K. Lamoreaux, "The Casimir force: background, experiments, and applications," Rep. Prog. Phys. **68**, 201–236 (2005).

[47] U. Mohideen and A. Roy, "Precision measurement of the Casimir force from 0.1 to 0.9 μm," Phys. Rev. Lett. **81**, 4549–4552 (1998).

[48] A. A. Banishev, G. L. Klimchitskaya, V. M. Mostepanenko, and U. Mohideen, "Demonstration of the Casimir force between ferromagnetic surfaces of a Ni-coated sphere and a Ni-coated plate," Phys. Rev. Lett. **110**, 137401 (2013), 1211.1470v2 .

[49] P. Bruno, "Long-Range Magnetic Interaction due to the Casimir Effect," Phys. Rev. Lett. **88**, 240401 (2002).

[50] G. Metalidis and P. Bruno, "Magnetic Casimir effect," Phys. Rev. A **66**, 062102 (2002).

[51] G. Bimonte, E. Calloni, G. Esposito, L. Milano, and L. Rosa, "Towards Measuring Variations of Casimir Energy by a Superconducting Cavity," Phys. Rev. Lett. **94**, 180402 (2005).

[52] G. Bimonte, G. Bimonte, E. Calloni, E. Calloni, G. Esposito, G. Esposito, L. Rosa, and L. Rosa, "Variations of Casimir energy from a superconducting transition," Nucl. Phys. B **726**, 441–463 (2005).

[53] A. O. Sushkov, W. J. Kim, D. A. R. Dalvit, and S. K. Lamoreaux, "Observation of the thermal Casimir force," Nat. Phys. **7**, 230–233 (2011).

[54] G. Torricelli, P. J. van Zwol, O. Shpak, C. Binns, G. Palasantzas, B. J. Kooi, V. B. Svetovoy, and M. Wuttig, "Switching Casimir forces with phase-change materials," Phys. Rev. A **82**, 010101 (2010).

[55] P. Ziherl, R. Podgornik, and S. Žumer, "Casimir force in liquid crystals close to the nematic–isotropic phase transition," Chem. Phys. Lett. **295**, 99–104 (1998).

[56] F. Chen, G. L. Klimchitskaya, V. M. Mostepanenko, and U. Mohideen, "Control of the casimir force by the modification of dielectric properties with light," Phys. Rev. B **76**, 035338 (2007).

[57] S. de Man, K. Heeck, R. J. Wijngaarden, and D. Iannuzzi, "Halving the casimir force with conductive oxides," Phys. Rev. Lett. **103**, 040402 (2009).

[58] C.-C. Chang, A. A. Banishev, G. L. Klimchitskaya, V. M. Mostepanenko, and U. Mohideen, "Reduction of the Casimir Force from Indium Tin Oxide Film by UV Treatment," Phys. Rev. Lett. **107**, 090403 (2011).

[59] M. Bordag, B. Geyer, G. L. Klimchitskaya, and V. M. Mostepanenko, "Constraints for hypothetical interactions from a recent demonstration of the Casimir force and some possible improvements," Phys. Rev. D **58**, 075003 (1998).

[60] J. C. Long, H. W. Chan, A. B. Churnside, E. A. Gulbis, M. C. M. Varney, and J. C. Price, "Upper limits to submillimetre-range forces from extra space-time dimensions," Nature **421**, 922–925 (2003).

[61] R. S. Decca, D. López, H. B. Chan, E. Fischbach, D. E. Krause, and C. R. Jamell, "Constraining New Forces in the Casimir Regime Using the Isoelectronic Technique," Phys. Rev. Lett. **94**, 240401 (2005).

[62] D. J. Kapner, T. S. Cook, E. G. Adelberger, J. H. Gundlach, B. R. Heckel, C. D. Hoyle, and H. E. Swanson, "Tests of the Gravitational Inverse-Square Law below the Dark-Energy Length Scale," Phys. Rev. Lett. **98**, 021101 (2007).

[63] D. M. Weld, J. Xia, B. Cabrera, and A. Kapitulnik, "New apparatus for detecting micron-scale deviations from Newtonian gravity," Phys. Rev. D **77**, 062006 (2008).

[64] F. Capasso, J. N. Munday, D. Iannuzzi, and H. B. Chan, "Casimir Forces and Quantum Electrodynamical Torques: Physics and Nanomechanics," IEEE J. Sel. Topics Quantum Electron. **13**, 400–414 (2007).

[65] R. Decca, D. López, E. Fischbach, G. Klimchitskaya, D. Krause, and V. Mostepanenko, "Precise comparison of theory and new experiment for the Casimir force leads to stronger constraints on thermal quantum effects and long-range interactions," Ann. Phys. **318**, 37–80 (2005).

[66] R. Decca, D. López, E. Fischbach, G. Klimchitskaya, D. Krause, and V. Mostepanenko, "Tests of new physics from precise measurements of the Casimir pressure between two gold-coated plates," Phys. Rev. D **75**, 077101 (2007).

[67] R. Castillo-Garza, J. Xu, G. L. Klimchitskaya, V. M. Mostepanenko, and U. Mohideen, "Casimir interaction at liquid nitrogen temperature: Comparison between experiment and theory," Phys. Rev. B **88**, 075402 (2013).

[68] A. A. Banishev, G. L. Klimchitskaya, V. M. Mostepanenko, and U. Mohideen, "Casimir interaction between two magnetic metals in comparison with nonmagnetic test bodies," Phys. Rev. B **88**, 155410 (2013).

[69] D. Garcia-Sanchez, K. Y. Fong, H. Bhaskaran, S. Lamoreaux, and H. X. Tang, "Casimir Force and In Situ Surface Potential Measurements on Nanomembranes," Phys. Rev. Lett. **109**, 027202 (2012).

[70] R. O. Behunin, F. Intravaia, D. A. R. Dalvit, P. A. Maia Neto, and S. Reynaud, "Modeling electrostatic patch effects in Casimir force measurements," Phys. Rev. A **85**, 012504 (2012).

[71] R. O. Behunin, D. A. R. Dalvit, R. S. Decca, C. Genet, I. W. Jung, A. Lambrecht, A. Liscio, D. López, S. Reynaud, G. Schnoering, G. Voisin, and Y. Zeng, "Kelvin probe force microscopy of metallic surfaces used in Casimir force measurements," Phys. Rev. A **90**, 062115 (2014).

[72] A. Naji, D. S. Dean, J. Sarabadani, R. R. Horgan, and R. Podgornik, "Fluctuation-induced interaction between randomly charged dielectrics," Phys. Rev. Lett. **104**, 060601 (2010).

[73] G. Bimonte, "Hide It to See It Better: A Robust Setup to Probe the Thermal Casimir Effect," Phys. Rev. Lett. **112**, 240401 (2014).

[74] G. Bimonte, "Apparatus for measuring the thermal casimir force at large distances," Phys. Rev. Lett. **113**, 240405 (2014).

[75] R. S. Decca, "Is it plasma or Drude? Experimental answer using rotating engineered samples," Presented at APS March Meeting 2015.

[76] D. J. Thouless, M. Kohmoto, M. P. Nightingale, and M. Den Nijs, "Quantized Hall conductance in a two-dimensional periodic potential," Phys. Rev. Lett. **49**, 405–408 (1982).

[77] X. Chen, Z. C. Gu, and X. G. Wen, "Local unitary transformation, long-range quantum entanglement, wave function renormalization, and topological order," Phys. Rev. B **82**, 1–28 (2010).

[78] G. E. Volovik, "Quantum phase transitions from topology in momentum space," Lect. Notes Phys. , 31–73 (2007).

[79] A. A. Burkov, "Chiral anomaly and transport in Weyl metals," J. Phys. Condens. Matter **27**, 113201 (2015).

[80] C. L. Kane and E. J. Mele, "Quantum spin hall effect in graphene," Phys. Rev. Lett. **95**, 226801 (2005).

[81] C. L. Kane and E. J. Mele, "Z_2 Topological Order and the Quantum Spin Hall Effect," Phys. Rev. Lett. **95**, 146802 (2005).

[82] J. E. Moore and L. Balents, "Topological invariants of time-reversal-invariant band structures," Phys. Rev. B **75**, 121306 (2007).

[83] B. A. Bernevig, T. L. Hughes, and S.-C. Zhang, "Quantum Spin Hall Effect and Topological Phase Transition in HgTe Quantum Wells," Science **314**, 1757–1761 (2006).

[84] M. König, S. Wiedmann, C. Brüne, A. Roth, H. Buhmann, L. W. Molenkamp, X.-L. Qi, and S.-C. Zhang, "Quantum spin hall insulator state in HgTe quantum wells." Science **318**, 766–70 (2007).

[85] A. Roth, C. Brüne, H. Buhmann, L. W. Molenkamp, J. Maciejko, X.-L. Qi, and S.-C. Zhang, "Nonlocal transport in the quantum spin Hall state." Science **325**, 294–7 (2009).

[86] D. Hsieh, D. Qian, L. Wray, Y. Xia, Y. S. Hor, R. J. Cava, and M. Z. Hasan, "A topological Dirac insulator in a quantum spin Hall phase." Nature **452**, 970–4 (2008).

[87] H.-J. Zhang, C.-X. Liu, X.-L. Qi, X.-Y. Deng, X. Dai, S.-C. Zhang, and Z. Fang, "Electronic structures and surface states of the topological insulator $Bi_{1-x}Sb_x$," Phys. Rev. B **80**, 085307 (2009).

[88] Y. Xia, D. Qian, D. Hsieh, L. Wray, A. Pal, H. Lin, A. Bansil, D. Grauer, Y. S. Hor, R. J. Cava, and M. Z. Hasan, "Observation of a large-gap topological-insulator class with a single Dirac cone on the surface," Nat. Phys. **5**, 398–402 (2009).

[89] H. Zhang, C.-X. Liu, X.-L. Qi, X. Dai, Z. Fang, and S.-C. Zhang, "Topological insulators in Bi_2Se_3, Bi_2Te_3 and Sb_2Te_3 with a single Dirac cone on the surface," Nat. Phys. **5**, 438–442 (2009).

[90] H. Nielsen and M. Ninomiya, "A no-go theorem for regularizing chiral fermions," Phys. Lett. B **105**, 219–223 (1981).

[91] C. Wu, B. A. Bernevig, and S.-C. Zhang, "Helical Liquid and the Edge of Quantum Spin Hall Systems," Phys. Rev. Lett. **96**, 106401 (2006).

[92] L. Fu and C. L. Kane, "Superconducting Proximity Effect and Majorana Fermions at the Surface of a Topological Insulator," Phys. Rev. Lett. **100**, 096407 (2008).

[93] C. Nayak, A. Stern, M. Freedman, and S. Das Sarma, "Non-Abelian anyons and topological quantum computation," Rev. Mod. Phys. **80**, 1083–1159 (2008).

[94] Q. Liu, C.-X. Liu, C. Xu, X.-L. Qi, and S.-C. Zhang, "Magnetic Impurities on the Surface of a Topological Insulator," Phys. Rev. Lett. **102**, 156603 (2009).

[95] M. Z. Hasan and C. L. Kane, "Colloquium: Topological insulators," Rev. Mod. Phys. **82**, 3045–3067 (2010).

[96] X.-L. Qi, T. L. Hughes, and S.-C. Zhang, "Topological field theory of time-reversal invariant insulators," Phys. Rev. B **78**, 195424 (2008).

[97] I. Garate and M. Franz, "Magnetoelectric response of the time-reversal invariant helical metal," Phys. Rev. B **81**, 172408 (2010).

[98] R. R. Biswas and A. V. Balatsky, "Impurity-induced states on the surface of three-dimensional topological insulators," Phys. Rev. B **81**, 233405 (2010).

[99] P. Wei, F. Katmis, B. A. Assaf, H. Steinberg, P. Jarillo-Herrero, D. Heiman, and J. S. Moodera, "Exchange-Coupling-Induced Symmetry Breaking in Topological Insulators," Phys. Rev. Lett. **110**, 186807 (2013).

[100] Y. L. Chen, J.-H. Chu, J. G. Analytis, Z. K. Liu, K. Igarashi, H.-H. Kuo, X. L. Qi, S. K. Mo, R. G. Moore, D. H. Lu, M. Hashimoto, T. Sasagawa, S. C. Zhang, I. R. Fisher, Z. Hussain, and Z. X. Shen, "Massive Dirac fermion on the surface of a magnetically doped topological insulator." Science **329**, 659–62 (2010).

[101] Y. S. Hor, P. Roushan, H. Beidenkopf, J. Seo, D. Qu, J. G. Checkelsky, L. A. Wray, D. Hsieh, Y. Xia, S. Y. Xu, D. Qian, M. Z. Hasan, N. P. Ong, A. Yazdani, and R. J. Cava, "Development of ferromagnetism in the doped topological insulator $Bi_{2-x}Mn_xTe_3$," Phys. Rev. B **81**, 195203 (2010).

[102] P. P. J. Haazen, J.-B. Laloë, T. J. Nummy, H. J. M. Swagten, P. Jarillo-Herrero, D. Heiman, and J. S. Moodera, "Ferromagnetism in thin-film Cr-doped topological insulator Bi_2Se_3," Appl. Phys. Lett. **100**, 082404 (2012).

[103] C.-Z. Chang, J. Zhang, X. Feng, J. Shen, Z. Zhang, M. Guo, K. Li, Y. Ou, P. Wei, L.-L. Wang, Z.-Q. Ji, Y. Feng, S. Ji, X. Chen, J. Jia, X. Dai, Z. Fang, S.-C. Zhang, K. He, Y. Wang, L. Lu, X.-C. Ma, and Q.-K. Xue, "Experimental observation of the quantum anomalous Hall effect in a magnetic topological insulator." Science **340**, 167–70 (2013).

[104] X.-L. Qi, R. Li, J. Zang, and S.-C. Zhang, "Inducing a Magnetic Monopole with Topological Surface States," Science **323**, 1184–1187 (2009).

[105] C. Wickles and W. Belzig, "Reflectionless transport of surface Dirac fermions on topological insulators with induced ferromagnetic domain walls," Phys. Rev. B **86**, 035151 (2012).

[106] A. M. Essin, J. E. Moore, and D. Vanderbilt, "Magnetoelectric polarizability and axion electrodynamics in crystalline insulators," Phys. Rev. Lett. **102**, 146805 (2009).

[107] J. Maciejko, X.-L. Qi, H. D. Drew, and S.-C. Zhang, "Topological Quantization in Units of the Fine Structure Constant," Phys. Rev. Lett. **105**, 166803 (2010).

[108] W.-K. Tse and A. H. MacDonald, "Giant Magneto-Optical Kerr Effect and Universal Faraday Effect in Thin-Film Topological Insulators," Phys. Rev. Lett. **105**, 057401 (2010), arXiv:arXiv:1003.2260v2 .

[109] W. K. Tse and A. H. MacDonald, "Magneto-optical Faraday and Kerr effects in topological insulator films and in other layered quantized Hall systems," Phys. Rev. B **84**, 205327 (2011).

[110] I. Garate and M. Franz, "Excitons and optical absorption on the surface of a strong topological insulator with a magnetic energy gap," Phys. Rev. B **84**, 045403 (2011).

[111] E. Hankiewicz, T. Jungwirth, T. Dietl, C. Timm, and J. Sinova, "Optical properties of metallic (III, Mn)V ferromagnetic semiconductors in the infrared to visible range," Phys. Rev. B **70**, 245211 (2004).

[112] V. Aji, "Adler-Bell-Jackiw anomaly in Weyl semimetals: Application to pyrochlore iridates," Phys. Rev. B **85**, 241101 (2012).

[113] A. A. Burkov, M. D. Hook, and L. Balents, "Topological nodal semimetals," Phys. Rev. B **84**, 235126 (2011).

[114] P. Hosur, S. a. Parameswaran, and A. Vishwanath, "Charge transport in Weyl semimetals," Phys. Rev. Lett. **108**, 046602 (2012).

[115] A. A. Zyuzin and A. A. Burkov, "Topological response in Weyl semimetals and the chiral anomaly," Phys. Rev. B **86**, 115133 (2012).

[116] G. B. Halász and L. Balents, "Time-reversal invariant realization of the Weyl semimetal phase," Phys. Rev. B **85**, 035103 (2012).

[117] A. G. Grushin, "Consequences of a condensed matter realization of Lorentz-violating QED in Weyl semi-metals," Phys. Rev. D **86**, 045001 (2012).

[118] A. A. Burkov and L. Balents, "Weyl semimetal in a topological insulator multilayer," Phys. Rev. Lett. **107**, 127205 (2011).

[119] Y. Chen, S. Wu, and A. A. Burkov, "Axion response in Weyl semimetals," Phys. Rev. B **88**, 125105 (2013).

[120] X. Wan, A. M. Turner, A. Vishwanath, and S. Y. Savrasov, "Topological semimetal and Fermi-arc surface states in the electronic structure of pyrochlore iridates," Phys. Rev. B **83**, 205101 (2011).

[121] G. Chen and M. Hermele, "Magnetic orders and topological phases from f-d exchange in pyrochlore iridates," Phys. Rev. B **86**, 235129 (2012).

[122] W. Witczak-Krempa and Y. B. Kim, "Topological and magnetic phases of interacting electrons in the pyrochlore iridates," Phys. Rev. B **85**, 045124 (2012).

[123] I. M. Lifshitz, "Anomalies of electron characteristics of a metal in the high pressure region," Sov. Phys. JETP **38**, 1569 (1960).

[124] A. A. Abrikosov, *Fundamentals of the theory of metals* (North-Holland, Amsterdam, 1988).

[125] K. S. Chen, Z. Y. Meng, T. Pruschke, J. Moreno, and M. Jarrell, "Lifshitz transition in the two-dimensional Hubbard model," Phys. Rev. B **86**, 165136 (2012).

[126] Y. Okamoto, A. Nishio, and Z. Hiroi, "Discontinuous Lifshitz transition achieved by band-filling control in Na_xCoO_2," Phys. Rev. B **81**, 121102 (2010).

[127] A. Hackl and M. Vojta, "Zeeman-Driven Lifshitz Transition: A Model for the Experimentally Observed Fermi-Surface Reconstruction in $YbRh_2Si_2$," Phys. Rev. Lett. **106**, 137002 (2011).

[128] M. R. Norman, J. Lin, and A. J. Millis, "Lifshitz transition in underdoped cuprates," Phys. Rev. B **81**, 180513 (2010).

[129] C. Liu, T. Kondo, R. M. Fernandes, A. D. Palczewski, E. D. Mun, N. Ni, A. N. Thaler, A. Bostwick, E. Rotenberg, J. Schmalian, S. L. Bud'ko, P. C. Canfield, and A. Kaminski, "Evidence for a Lifshitz transition in electron-doped iron arsenic superconductors at the onset of superconductivity," Nat. Phys. **6**, 419–423 (2010).

[130] S. Hikami, A. I. Larkin, and Y. Nagaoka, "Spin-Orbit Interaction and Magnetoresistance in the Two Dimensional Random System," Prog. Theor. Phys, **63**, 707–710 (1980).

[131] B. L. Altshuler, D. Khmel'nitzkii, A. I. Larkin, and P. A. Lee, "Magnetoresistance and Hall effect in a disordered two-dimensional electron gas," Phys. Rev. B **22**, 5142–5153 (1980).

[132] P. A. Lee, "Disordered electronic systems," Rev. Mod. Phys. **57**, 287–337 (1985).

[133] G. Bergmann, "Weak localization in thin films: a time-of-flight experiment with conduction electrons," Phys. Rep. **107**, 1–58 (1984).

[134] J. J. Lin and J. P. Bird, "Recent experimental studies of electron dephasing in metal and semiconductor mesoscopic structures," J. Phys. Condens. Matter **14**, R501–R596 (2002).

[135] B. L. Altshuler, A. G. Aronov, and D. Khmel'nitzkii, "Effects of electron-electron collisions with small energy transfers on quantum localisation," J. Phys. C **15**, 7367–7386 (1982).

[136] A. Altland and B. D. Simons, *Condensed Matter Field Theory*, 2nd ed. (Cambridge University Press, Cambridge, 2010).

[137] X. Wen, *Quantum Field Theory of Many-body Systems*, reissue ed. (Oxford University Press, 2007).

[138] M. E. Peskin and D. V. Schroeder, *An Introduction To Quantum Field Theory* (Westview Press, 1995).

[139] J. R. Klauder, "Continuous representations and path integrals, revisited," in *Path Integrals and their Applications in Quantum, Statistical, and Solid State Physics*, edited by G. Papadopoulos and J. Devreese (Plenum Press, Antwerp, Belgium, 1977).

[140] F. A. Berezin, "Feynman path integrals in a phase space," Sov. Phys. Usp. **23**, 763–788 (1980).

[141] J. R. Klauder and B. Skagerstam, *Coherent states: applications in physics and mathematical physics* (World Scientific, 1985).

[142] J. R. Klauder, "The Feynman path integral: An historical slice," (2003), `arXiv:quant-ph/0303034v1`.

[143] R. J. Glauber, "Coherent and incoherent states of the radiation field," Phys. Rev. **131**, 2766 (1963).

[144] A. M. Perelomov, "Coherent states for arbitrary lie group," Commun. Math. Phys. **26**, 222–236 (1972).

[145] R. Gilmore, "Geometry of symmetrized states," Ann. Phys. **74**, 391–463 (1972).

[146] W. Zhang, D. H. Feng, and R. Gilmore, "Coherent states: Theory and some applications," Rev. Mod. Phys. **62**, 867 (1990).

[147] A. M. Perelomov, *Generalized coherent states and their applications* (Birkhäuser, 1986).

[148] M. Enz and R. Schilling, "Spin tunnelling in the semiclassical limit," J. Phys. C **19**, 1765–1770 (1986).

[149] K. Funahashi, T. Kashiwa, S. Sakoda, and K. Fujii, "Coherent states, path integral, and semiclassical approximation," J. Math. Phys. **36**, 3232 (1995).

[150] K. Funahashi, T. Kashiwa, S. Nima, and S. Sakoda, "More about path integrals for spin," Nucl. Phys. B **453**, 508–528 (1995).

[151] V. I. Belinicher, C. Providencia, and J. da Providencia, "Instanton picture of the spin tunnelling in the Lipkin-Meshkov-Glick model," J. Phys. A **30**, 5633–5643 (1997).

[152] J. Shibata and S. Takagi, "A note on (spin-) coherent-state path integral," Int. J. Mod. Phys. B **13**, 107–140 (1999).

[153] H. G. Solari, "Semiclassical treatment of spin system by means of coherent states," J. Math. Phys. **28**, 1097 (1987).

[154] M. Stone, K. Park, and A. Garg, "The semiclassical propagator for spin coherent states," J. Math. Phys. **41**, 8025 (2000).

[155] E. A. Kochetov, "Quasiclassical path integral in coherent-state manifolds," J. Phys. A **31**, 4473–4492 (1998).

[156] M. Pletyukhov, "On the extra phase correction to the semiclassical spin coherent-state propagator," J. Math. Phys. **45**, 1859 (2004).

[157] A. Polkovnikov, "Phase space representation of quantum dynamics," Ann. Phys. **325**, 1790–1852 (2010).

[158] W. Richter and C. R. Becker, "A Raman and farinfrared investigation of phonons in the rhombohedral V2–VI3 compounds Bi_2Te_3, Bi_2Se_3, Sb_2Te_3 and $Bi_2(Te_{1-x}Se_x)_3$ $(0 < x < 1)$, $(Bi_{1-y}Sb_y)_2Te_3$ $(0 < y < 1)$," Phys. Status Solidi **84**, 619–628 (1977).

[159] D. S. Novikov, "Elastic scattering theory and transport in graphene," Phys. Rev. B **76**, 245435 (2007).

[160] A. V. Shytov, M. I. Katsnelson, and L. S. Levitov, "Atomic Collapse and Quasi–Rydberg States in Graphene," Phys. Rev. Lett. **99**, 246802 (2007).

[161] A. V. Shytov, M. I. Katsnelson, and L. S. Levitov, "Vacuum polarization and screening of supercritical impurities in graphene," Phys. Rev. Lett. **99**, 236801 (2007).

[162] O. V. Gamayun, E. V. Gorbar, and V. P. Gusynin, "Supercritical coulomb center and excitonic instability in graphene," Phys. Rev. B **80**, 165429 (2009).

[163] Y. Lan, S. Wan, and S.-C. Zhang, "Generalized quantization condition for topological insulators," Phys. Rev. B **83**, 205109 (2011).

[164] G. Tkachov and E. M. Hankiewicz, "Anomalous galvanomagnetism, cyclotron resonance, and microwave spectroscopy of topological insulators," Phys. Rev. B **84**, 035405 (2011).

[165] Z. Li and J. P. Carbotte, "Hexagonal warping on optical conductivity of surface states in topological insulator Bi_2Te_3," Phys. Rev. B **87**, 155416 (2013).

[166] Z. Li and J. P. Carbotte, "Magneto-optical conductivity in a topological insulator," Phys. Rev. B **88**, 045414 (2013).

[167] H. Beidenkopf, P. Roushan, J. Seo, L. Gorman, I. Drozdov, Y. S. Hor, R. J. Cava, and A. Yazdani, "Spatial fluctuations of helical Dirac fermions on the surface of topological insulators," Nat. Phys. **7**, 939–943 (2011).

[168] D. Kim, S. Cho, N. P. Butch, P. Syers, K. Kirshenbaum, S. Adam, J. Paglione, and M. S. Fuhrer, "Surface conduction of topological Dirac electrons in bulk insulating Bi_2Se_3," Nat. Phys. **8**, 460–464 (2012).

[169] J. N. Hancock, J. L. M. van Mechelen, A. B. Kuzmenko, D. van der Marel, C. Brüne, E. G. Novik, G. V. Astakhov, H. Buhmann, and L. W. Molenkamp, "Surface State Charge Dynamics of a High-Mobility Three-Dimensional Topological Insulator," Phys. Rev. Lett. **107**, 136803 (2011).

[170] A. M. Shuvaev, G. V. Astakhov, G. Tkachov, C. Brüne, H. Buhmann, L. W. Molenkamp, and A. Pimenov, "Terahertz quantum Hall effect of Dirac fermions in a topological insulator," Phys. Rev. B **87**, 121104 (2013).

[171] R. Valdés Aguilar, A. V. Stier, W. Liu, L. S. Bilbro, D. K. George, N. Bansal, L. Wu, J. Cerne, A. G. Markelz, S. Oh, and N. P. Armitage, "Terahertz Response and Colossal Kerr Rotation from the Surface States of the Topological Insulator Bi_2Se_3," Phys. Rev. Lett. **108**, 087403 (2012).

[172] G. S. Jenkins, A. B. Sushkov, D. C. Schmadel, M.-H. Kim, M. Brahlek, N. Bansal, S. Oh, and H. D. Drew, "Giant plateau in the terahertz Faraday angle in gated Bi_2Se_3," Phys. Rev. B **86**, 235133 (2012).

[173] G. S. Jenkins, D. C. Schmadel, A. B. Sushkov, H. D. Drew, M. Bichler, G. Koblmueller, M. Brahlek, N. Bansal, and S. Oh, "Dirac cone shift of a passivated topological Bi_2Se_3 interface state," Phys. Rev. B **87**, 155126 (2013).

[174] C. S. Tang, B. Xia, X. Zou, S. Chen, H.-W. Ou, L. Wang, a. Rusydi, J.-X. Zhu, and E. E. M. Chia, "Terahertz conductivity of topological surface states in $Bi_{1.5}Sb_{0.5}Te_{1.8}Se_{1.2}$," Sci. Rep. **3**, 3513 (2013).

[175] L. Wu, M. Brahlek, R. Valdés Aguilar, a. V. Stier, C. M. Morris, Y. Lubashevsky, L. S. Bilbro, N. Bansal, S. Oh, and N. P. Armitage, "A sudden collapse in the transport lifetime across the topological phase transition in $(Bi_{1-x}In_x)_2Se_3$," Nat. Phys. **9**, 410–414 (2013).

[176] Z. Zhang, C.-Z. Chang, Z. Zuocheng, J. Wen, X. Feng, K. Li, M. Liu, K. He, L. Wang, X. Chen, Q.-K. Xue, X. Ma, and Y. Wang, "Band structure engineering in $(Bi_{1-x}Sb_x)_2Te_3$ ternary topological insulators," Nat. Commun **2**, 574 (2011).

[177] C.-Z. Chang, J. Zhang, M. Liu, Z. Zhang, X. Feng, K. Li, L.-L. Wang, X. Chen, X. Dai, Z. Fang, X.-L. Qi, S.-C. Zhang, Y. Wang, K. He, X.-C. Ma, and Q.-K. Xue, "Thin films of magnetically doped topological insulator with carrier-independent long-range ferromagnetic order." Advanced materials **25**, 1065–70 (2013).

[178] M. Lasia and L. Brey, "Optical properties of magnetically doped ultrathin topological insulator slabs," Phys. Rev. B **90**, 075417 (2014).

[179] P. Parashar, K. A. Milton, K. V. Shajesh, and M. Schaden, "Electromagnetic semitransparent δ-function plate: Casimir interaction energy between parallel infinitesimally thin plates," Phys. Rev. D **86**, 085021 (2012).

[180] G. Barton, "Casimir effects for a flat plasma sheet: I. Energies," J. Phys. A **38**, 2997 (2005).

[181] G. Barton, "Casimir effects for a flat plasma sheet: II. Fields and stresses," J. Phys. A **38**, 3021 (2005).

[182] M. Bordag, I. V. Fialkovsky, D. M. Gitman, and D. V. Vassilevich, "Casimir interaction between a perfect conductor and graphene described by the dirac model," Phys. Rev. B **80**, 245406 (2009).

[183] D. Drosdoff and L. M. Woods, "Casimir forces and graphene sheets," Phys. Rev. B **82**, 155459 (2010).

[184] B. E. Sernelius, "Casimir interactions in graphene systems," Europhys. Lett. **95**, 57003 (2011).

[185] J. D. Koralek, C. P. Weber, J. Orenstein, B. A. Bernevig, S.-C. Zhang, S. Mack, and D. D. Awschalom, "Emergence of the persistent spin helix in semiconductor quantum wells," Nature **458**, 610–613 (2009).

[186] R. Winkler, *Spin–Orbit Coupling Effects in Two-Dimensional Electron and Hole Systems*, Springer Tracts in Modern Physics, Vol. 191 (Springer Berlin Heidelberg, Berlin, Heidelberg, 2003).

[187] N. W. Ashcroft and N. D. Mermin, *Solid State Physics* (Saunders College, 1976) p. 826.

[188] R. S. Decca, D. López, and E. Osquiguil, "New results for the Casimir interaction: sample characterization and low temperature measurements," Int. J. Mod Phys A **25**, 2223–2230 (2010).

[189] B. L. Altshuler, "Fluctuations in the extrinsic conductivity of disordered conductors," JETP Lett. **41**, 648 (1985).

[190] P. A. Lee and A. D. Stone, "Universal conductance fluctuations in metals," Phys. Rev. Lett. **55**, 8–11 (1985).

[191] V. B. Bezerra, G. L. Klimchitskaya, and V. M. Mostepanenko, "Correlation of energy and free energy for the thermal Casimir force between real metals," Phys. Rev. A **66**, 062112 (2002).

[192] V. B. Bezerra, G. L. Klimchitskaya, V. M. Mostepanenko, and C. Romero, "Violation of the Nernst heat theorem in the theory of the thermal Casimir force between Drude metals," Phys. Rev. A **69**, 022119 (2004).

[193] I. Brevik, S. A. Ellingsen, J. S. Høye, and K. A. Milton, "Analytical and Numerical Demonstration of How the Drude Dispersive Model Satisfies Nernst's Theorem for the Casimir Entropy," J. Phys. A **41**, 164017 (2007).

[194] J. Rammer, "Quantum transport theory of electrons in solids: A single-particle approach," Rev. Mod. Phys. **63**, 781–817 (1991).

[195] B. Q. Lv, H. M. Weng, B. B. Fu, X. P. Wang, H. Miao, J. Ma, P. Richard, X. C. Huang, L. X. Zhao, G. F. Chen, Z. Fang, X. Dai, T. Qian, and H. Ding, "Discovery of Weyl semimetal TaAs," (2015), `arXiv:1502.04684`.

[196] P. Goswami and S. Tewari, "Axionic field theory of (3+1)-dimensional Weyl semimetals," Phys. Rev. B **88**, 245107 (2013).

[197] B. Rosenstein and M. Lewkowicz, "Dynamics of electric transport in interacting Weyl semimetals," Phys. Rev. B **88**, 045108 (2013).

[198] A. Alekseev, L. Faddeev, and S. Shatashvili, "Quantization of symplectic orbits of compact Lie groups by means of the functional integral," J. Geom. and Phys. **5**, 391 (1989).

[199] D. C. Cabra, A. Dobry, A. Greco, and G. L. Rossini, "On the path integral representation for spin systems," J. Phys. A **30**, 2699–2704 (1997).

[200] Y. Yanay and E. J. Mueller, "Saving the coherent state path integral," (2012), `arXiv:1212.4802`.

[201] R. Gilmore, *Lie groups, physics, and geometry* (Cambridge University Press, 2008).

[202] H. Kleinert, *Path Integrals in Quantum Mechanics, Statistics, Polymer Physics, and Financial Markets*, EBL-Schweitzer (World Scientific Publishing Company Pte Limited, 2009).